Mitofusin Disease Variant Provides Insight into Mitochondrial Tethering and Fusion

Stephanie Rene Sloat

A dissertation

Submitted in partial fulfillment of the

Requirements for the degree of

Doctor of Philosophy

University of Washington

2021

Reading Committee:

Suzanne Hoppins, Chair

James Hurley

Alexey Merz

Program Authorized to Offer Degree:

Biochemistry

University of Washington

Abstract

Mitofusin Disease Variant Provides Insight into Mitochondrial Tethering and Fusion

Stephanie Rene Sloat

Chair of the Supervisory Committee:
Suzanne Hoppins
Department of Biochemistry

Mitochondria are dynamic organelles that produce the energy we need to move, grow, and think. Every cell, from muscles in the heart to neurons in the brain, has a unique and ever-changing requirement for energy. In order to adapt to the needs of each cell, mitochondria adjust shape through fusion, division and movement. Mitochondrial fusion in particular requires two molecular machines, called mitofusins. These mitofusins, Mfn1 and Mfn2, cooperate to drive membranes together through a mechanism that couples GTP hydrolysis, oligomerization, and conformational changes. Despite the importance of mitochondrial fusion in cell health, much of this mechanism is still unknown. In this work, I utilize a disease associated variant, Mfn2^{S350P} and the equivalent Mfn1^{S329P} variant in order to perform a structure-function analysis. I found that expression of either variant led to a perinuclear clustering of mitochondria, which differs from the reticular morphology of healthy cells. Mitochondria within the cluster do not have a connected mitochondrial matrix, indicating that individual mitochondria are in close proximity as opposed to fusing into one large mitochondria in the perinuclear space. Interestingly, microtubule-based transport of the mitochondria to the perinuclear space is not responsible for perinuclear clustering. Instead, clusters appeared to be caused by interactions between mitofusins across mitochondrial membranes, forming the mitofusin *trans* complex. This indicates mitochondria are tethered together, but unable to proceed with full fusion. I also found that GTP hydrolysis is necessary for mitochondrial cluster formation, indicating that GTP hydrolysis is necessary for the formation of the *trans*

complex. Additionally, I made progress in developing a method to measure conformational changes in full length mitofusin on the surface of isolated mitochondria based on the recently published technique, ACCuRET. Taken together, the work presented in my dissertation reveals unique insight into mitochondrial tethering and fusion and makes progress toward techniques to further analyze the molecular mechanism of mitofusin.

Table of Contents

Table of Figures

Acknowledgements

I am incredibly thankful to everyone who has supported me during my graduate work. I would first like to thank my advisor, Dr. Suzanne Hoppins, for her guidance and support. I have learned so much from you over the last few years. I would also like to thank members of the Hoppins Lab, both past and present, for commiseration and stimulating conversation. I am grateful to my thesis committee, Drs. Jim Hurley, Alex Merz, Jihong Bai and Kelly Lee, for their guidance on my research.

I would also like to thank my family and friends who have been so supportive during my journey. My parents, Greg and Traci MacDonald, who have always believed in me. My dog, Ryder, who provided emotional support and enforced breaks. And last, but not least, my husband, Dan. I could not have done this without your love, support, and encouragement. You and our growing family make the hard work worthwhile.

Chapter 1. Introduction

1.1 Mitochondria and Mitochondrial Dynamics

Mitochondria fuel the processes that allow us to grow, move and think. This is accomplished in part through the production of adenosine triphosphate (ATP), a ubiquitous high energy molecule that can be broken down to fuel biological processes with high energy demands. Mitochondria also serve many other functions, including calcium buffering, lipid synthesis and managing the cellular response to stress (Zeniseck and Matthews, 2000; Mejia, Nguyen and Hatch, 2014; Scorrano et al., 2002). Disruptions to mitochondrial health or function have been associated with many diseases, including heart disease, cancer, diabetes and neurodegenerative diseases such as Alzheimer's and Parkinson's Disease (Chaanine et al., 2019; Zong, Rabinowitz and White, 2016; Rovira-Llopis, 2017; Blass, Sheu and Gibson, 2000; MacDonald et al., 2018).

Healthy mitochondrial function relies on the dynamic nature of mitochondria. Each cell has many mitochondria that form a vast and dynamic network throughout the cell. Mitochondria constantly move, fuse and divide to maintain the integrity of mitochondrial function and adapt to the ever-changing needs of the cell. At steady state, a balance of mitochondrial fusion and division is necessary to maintain mitochondrial DNA (mtDNA) and membrane potential (Yan et al, 2019). During periods of unique energy demand, mitochondria can shift the balance of dynamics to change the shape of the mitochondrial network to meet those demands. For example, it has been shown that mitochondria increase fusion to create a more connected network in order to combat mild cell stress as elongated mitochondria are more efficient at making ATP (Tondera et al, 2009; Gomes, Benedetto and Scorrano, 2011; Rambold et al., 2011). Conversely, mitochondria increase division to form a fragmented network which precedes programmed cell death (apoptosis) (Wu et al., 20011). Mitochondrial dynamics are also important for mitosis. Mitochondria increase fusion to form a hyperfused network in the G1-S transition, which has been proposed to address the increased energy demand of DNA replication. This is followed by mitochondrial fragmentation during the G2 and M phases of the cell cycle in order to evenly segregate mitochondria to daughter cells, further followed by increased fusion during G1 phase to restore the connected network (Mishra and Chan, 2014). Mitochondria are also mobile. In neurons, mitochondria are transported down axons and will stop at regions of high energy demand, such as synaptic terminals, in order to supply the region with ATP and buffer

calcium (Schwarz, 2013). Transport has been shown to aid in both mitochondrial fusion and division. Mitochondria move to meet for fusion and are pulled apart after division on microtubule tracks (Liu et al., 2009). The interconnection between mitochondrial fusion, division and transport is coordinated and necessary for cell function.

1.2 Molecular Mechanisms of Mitochondrial Dynamics

Remodeling of membranes has a large activation barrier, requiring an input of energy from molecular machines. One class of membrane remodeling proteins is the dynamin superfamily of proteins (DSPs). DSPs are large GTPases that coordinate GTP hydrolysis with oligomerization and conformational changes to drive membrane remodeling (Jimah and Hinshaw, 2019). Dynamin, the first and most well characterized member of the family, is responsible for dividing endocytic vesicles from the plasma membrane (Ferguson and de Camilli, 2012). Characteristic of DSPs, dynamin consists of a large GTPase domain, 2 helical bundles (BSE and Stalk domains) and a membrane interacting domain (Figure 1.1). Dynamin interacts with the base of the budding endocytic vesicle at the plasma membrane through the membrane binding domain and oligomerizes through interactions on the helical bundle backbone to form rings that wrap around the base of the vesicle bud. Adjacent dynamin rings on the base of the vesicle bud dimerize at the GTPase domain. Then, GTP hydrolysis powers a conformational change that constricts the dynamin ring and delivers the power stroke to divide the membrane.

1.2.1 Atlastin

DSPs are also involved in membrane fusion. Atlastin is responsible for the fusion of endoplasmic reticulum (ER) tubules (Orso et al., 2009). Atlastin shares some of the same basic domain architecture with dynamin, as well as the key features of the family including GTP hydrolysis, intermolecular contacts and conformational changes (Figure 1.1). Atlastin is embedded in the ER membrane through a transmembrane domain with the bulk of the protein facing the cytosol. Unlike the mechanism of membrane division DSPs, GTP binding and hydrolysis stimulates dimerization of atlastin through interfaces on the GTPase domain to form a *trans* interaction between atlastins on opposing ER membranes (Byrnes et al., 2013; Liu et al., 2015). It has been proposed that release of inorganic phosphate from the binding pocket stimulates the final conformational change that drives membranes together (Liu et al., 2015).

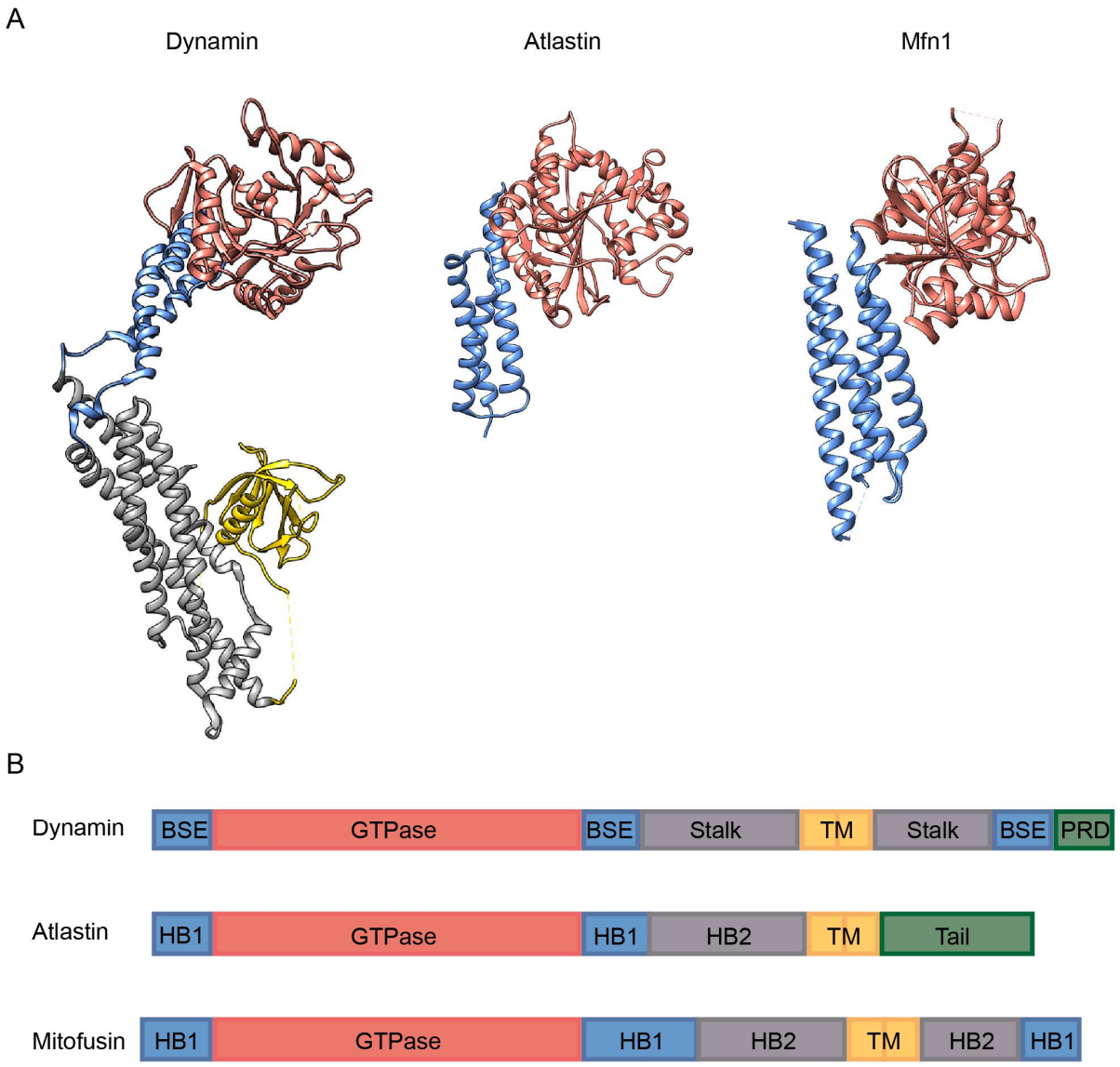

Figure 1.1 Structures from select DSPs

A) Structure of Dynamin 3 (5A3F), Atlastin 1 (3Q5E), and Mfn1 (5YEW) with GTPase domain in pink, helical bundle 1 (HB1)/BSE in blue, helical bundle 2 (HB2)/Stalk in grey and membrane binding domain (TM) in yellow. (B) Domain architecture in corresponding colors. Features not depicted in (A), proline rich domain (PRD) and tail domain, in green.

1.2.2 Mitochondrial Outer Membrane Fusion

Mitochondrial outer membrane (MOM) fusion is mediated by two mitofusin proteins, Mfn1 and Mfn2. Mfn1 and Mfn2 are paralogs with 60% sequence identity and 77% sequence similarity, however they have a unique function (Santel and Fuller, 2001; Chen et al., 2003; Eura et al., 2003; Ishihara et al., 2004; Sloat et al., 2019). Knock out of either Mfn1 or Mfn2 is embryonic lethal, highlighting that mitofusin is essential, suggesting a role for mitochondrial dynamics in development (Chen et al., 2003).

Similar to other DSPs, Mfn1 and Mfn2 have a large globular GTPase domain (G domain), 2 helical bundles (HB1 and HB2) and a transmembrane domain (TM) for insertion into the mitochondrial outer membrane (Figure 1.1) (Rojo et al., 2002). The two helical bundles are connected by a predicted hinge (Hinge 1) and the G-domain and HB1 are connected through hinge 2.

A precise model for mitochondrial fusion has yet to be determined, though much research has been conducted on this subject. Research has shown that GTPase activity of mitofusins is necessary for function (Ishihara at al., 2004). Mutations in the GTPase domain of Mfn1 fail to rescue reticular mitochondrial morphology in Mfn1-null cells and mutations in the GTPase domain of Mfn2 have been reported in disease (Qi et al., 2016; Züchner et al., 2004). Interestingly, GTPase activity in vitro is higher for Mfn1 than Mfn2, highlighting a distinction between Mfn1 and Mfn2 (Ishihara et al., 2004; Li et al., 2019). Similar to other known DSPs, GTPase activity alters the conformational state of the Mfn1 (Yan et al., 2018). When bound to GDP, mitofusin adopts an open conformation in which the α-helix at Hinge 2 is intact. When bound to the transition state mimic, GDP-BeF_3, mitofusin adopts a closed formation in which a 77-degree angle is introduced into the α-helix centered around serine residue 329 in Mfn1 (Yan et al., 2018). To date, research on conformational changes in mitofusin has been restricted to the mini mitofusin variant. How full-length protein responds to nucleotide state, such as any conformational changes around Hinge 1, have yet to be identified.

In addition to GTP hydrolysis and conformational changes, the mitofusins assemble into higher order oligomers in *cis*, on the same membrane, and in *trans*, on opposing membranes. BN-PAGE analysis shows that mitofusin likely exists as a *cis* dimer under steady state conditions. When bound to a non-hydrolysable GTP analogue or transition state mimic of GTP hydrolysis, mitofusin assembles into at least 2 larger species, roughly consistent with a trimer or tetramer, also in *cis* (Engelhart and Hoppins, 2019; Sloat et al., 2019). Studies on the yeast homolog of mitofusin, Fzo-1, suggest mitofusin assembles into a large ring in *cis* which initiates formation of a membrane fusion pore, however this assembly has yet to be confirmed for mitofusin in mammalian cells (Brandt et al., 2016). Mitofusin is also expected to form *trans* assemblies as mitofusin has been shown to be required on both mitochondrial membranes for efficient fusion (Hoppins et al., 2011; Detmer and Chan, 2007). The structural interfaces required for assembly in

cis or *trans* is unknown. Based on models of DSPs with similar homology to mitofusin, mitofusin is predicted to interact between the helical bundles for *cis*-assembly (Rocha et al., 2018). However, this interaction has yet to be tested. To date, two assembly interfaces have been proposed to constitute the *trans* interaction. X-ray crystallography studies of the mini-mitofusin have shown that Mfn1 interacts through the GTPase domain, creating the G-G interface (Cao et al., 2017; Yan et al., 2018). When this mini-mitofusin is inserted into liposomes, clustering of the proteoliposomes is supported only when the G-G interface is intact, supporting the model that the G-G interface composes the *trans* interaction (Cao et al., 2017). Mitofusin has also been proposed to oligomerize through interactions with the c-terminal α-helix, forming an anti-parallel coiled-coil (Koshiba et al., 2004). The field has yet to reach a consensus on whether either of these interfaces constitutes the *trans* assembly for mitofusin.

1.2.3 Mitochondrial Transport

Mitochondria are transported throughout the cell on the microtubule network through the mitochondrial transport complex. Dynein is the molecular motor that drives mitochondria in the retrograde direction, or towards the minus end of microtubules, and kinesin is responsible for transport in the anterograde direction, or towards the plus end of microtubules (Schwarz, 2013). These molecular motors connect to mitochondria through two adaptor proteins, Miro and Trak (Fransson et al., 2006; Glater et al., 2006; Schwarz, 2013). Miro is embedded in the MOM and contains two EF hand calcium binding domains and 2 GTPase domains. Binding of calcium to Miro EF hands signals mitochondria to pause at that location (Fransson et al., 2003). Binding of GTP to GTPase domain 1 of Miro increases activity, but the role of GTPase domain 2 is unknown (Fransson et al., 2006). Interestingly, both constitutively active and dominant negative variants of Miro lead to an accumulation of mitochondria in the perinuclear space (Fransson et al., 2003; Fransson et al., 2006). Trak is an intermediate adaptor between Miro and both dynein and kinesin, though data suggests it also interacts directly with mitochondria in the absence of Miro (Glater et al., 2006; van Spronsen et al., 2013).

Interestingly, there is a link between mitochondrial fusion machinery and transport. In mouse embryonic fibroblasts lacking Mfn1 or Mfn2, fragmented mitochondria have significantly decreased motility (Chen et al., 2003). Characterization of cells expressing disease variants of Mfn2 has revealed decreased

mitochondrial transport, although the molecular basis is not well understood (Baloh et al., 2007). Consistent with this, in a transgenic mouse model of CMT2A expressing $Mfn2^{T105M}$ in motor neurons, mitochondria were excluded from axons (Detmer et al., 2008). Coimmunoprecipitation experiments suggest mitofusin may interact directly with the transport machinery (Misko et al., 2010). It has been suggested that mitofusin can directly regulate mitochondrial transport, but the exact nature of this interaction is still unknown.

1.3 Mitochondrial Fusion and Disease

1.3.1 Mfn2 and Charcot-Marie-Tooth Type 2A

Mutations in Mfn2 lead to the peripheral neuropathy Charcot-Marie-Tooth Type 2A (CMT2A) (Cartoni and Martinou, 2009). CMT2A is characterized by degeneration of peripheral neurons affecting roughly 1 in every 2,500 births (Stuppia et al., 2015; Züchner et al., 2004). CMT2A can cause lower leg and arm weakness, imbalance, foot deformities, and loss of fine motor coordination. The mutations that cause CMT2A are found throughout the *MFN2* gene. Many disease-causing mutations are found in the GTPase domain, but there are other hot spots, including around Hinge 1 and Hinge 2, implicating these regions in the function of Mfn2.

Many disease-causing mutations in Mfn2 have a unique phenotype characterized by perinuclear clustering of mitochondria. Several mouse models have been created to model CMT2A, in which mitochondria are excluded from the axons of neurons and mice exhibited defects in muscle mass and strength among other defects (Detmer et al., 2008; Stavropoulos et al, 2021). Perinuclear aggregation of mitochondria in disease models has led to one possible hypothesis that CMT2A is caused by mis-localization of mitochondria in neurons due to changes in transport (Baloh et al., 2007; Cartoni and Marsinou, 2009). Indeed, mitochondria from DRG neurons expressing a CMT2A variant, $Mfn2^{R94Q}$, exhibit perinuclear clustering have decreased motility in both the anterograde and retrograde directions (Misko et al., 2010; Zhou et a., 2019). However, $Mfn2^{R94Q}$ was also found to be defective for fusion separately from the defect in transport (Baloh et al., 2007; Detmer et al., 2007). In a mouse model of CMT2A expressing $Mfn2^{R94Q}$, overexpression of Mfn1 restored mitochondrial distribution and rescued neurodegeneration, suggesting the fusion defect of $Mfn2^{R94Q}$, not transport defect, was the main factor in disease pathogenesis (Zhou et a., 2019).

1.3.2 Effect of Disease on Mitochondrial Dynamics

A wide range of diseases have altered mitochondrial dynamics with consequences for mitochondrial function, which has been demonstrated in many studies. For example, in healthy heart muscle, mitochondria line sarcomeres in order to supply ATP and Ca^{2+} buffering for muscle contraction. In mice induced with heart failure, mitochondria are smaller and more spherical in shape (Ferreira et al., 2019). This change in mitochondrial shape corresponds with low mitochondrial respiration and increased reactive oxygen species (ROS) and is correlated with shortened sarcomeres and decreased heart function. Another study demonstrated diabetes pathogenesis includes alterations to mitochondrial dynamics. Islet cells in the pancreas are responsible for synthesis and secretion of insulin in response to glucose. Mitochondria in these cells typically have elongated mitochondria in a connected reticular network. However, in diabetes models, the mitochondria in these cells are fragmented, have lower ATP production and increased ROS (Bindokas et al., 2003; Wada and Nakatsuka, 2016; Rovira-Llopis et al., 2017). Similarly, in neurons in the hippocampus of Alzheimer's disease patients and in mouse models of Parkinson's disease, mitochondria have fragmented morphology and mitochondrial disfunction (Zhu et al., 2013; Wang et al., 2017; Li et al., 2021).

Recently, strides have been made to alter mitochondrial dynamics in models of disease. In mice, heart disease has been modeled by manual induction of myocardial infarction. It was discovered that a protein kinase, βII protein kinas C (βIIPKC) phosphorylates Mfn1, leading to mitochondrial fragmentation and dysfunction. Inhibition of Mfn1 phosphorylation by a peptide designed to interrupt the interaction between βIIPKC and Mfn1 restored mitochondrial shape, size and function in heart muscle (Ferreira et al., 2019). Other treatments aimed at inhibiting mitochondrial division or stimulating mitochondrial fusion have been shown to increase mitochondrial connectivity and function in CMT2A, Alzheimer's Disease, and Parkinson's Disease models (Rocha et al., 2018; Zhou et al., 2019; Franco et al., 2020; Li et al., 2021; Dang et al., 2021). These promising results highlight the need for accurate models of mitofusin function in order to develop targeted regulation of mitochondrial fusion to treat disease.

Chapter 2. A dominant negative mitofusin variant reveals that mitochondrial tethering requires GTP hydrolysis

Chapter 2 is adapted with minimal modification from:

Sloat SR and Hoppins S. A dominant negative mitofusin variant reveals that mitochondrial tethering requires GTP hydrolysis. Submitted to Life Science Alliance.

2.1 Abstract

Mitochondrial fusion is essential for mitochondrial function and cellular health. In vertebrates, mitochondrial outer membrane fusion is mediated by two mitofusin paralogs, Mfn1 and Mfn2, which are conserved dynamin superfamily proteins. Here we characterize a variant of mitofusin reported in patients with CMT2A where a serine is replaced with a proline in a hinge domain (Hinge 2) connecting the globular GTPase domain to the adjacent extended helical bundle. We find that expression of this variant results in prolific and irreversible mitochondrial tethering that blocks mitochondrial fusion by wild-type mitofusin. Our data indicate that mitofusin-mediated mitochondrial tethering requires GTP hydrolysis and formation of a mitofusin complex across two membranes. We propose that mitofusin exists primarily in a low-energy state that is inactive and that GTP hydrolysis converts mitofusin to a high-energy state that can tether mitochondria. Our data further imply that within the mitofusin tethering complex, Hinge 2 supports a power stroke to progress the complex from tethering to membrane fusion.

2.2 Introduction

Mitochondria are dynamic organelles that move, fuse and divide. Mitochondrial fusion is necessary for maintaining mitochondrial function and cell health (Chan, 2020; Giacomello et al., 2020; Murata et al., 2020; Pernas and Scorrano, 2016). Mitochondria contribute to many cellular functions including energy production, calcium signaling, nutrient sensing and signaling in innate immunity and cell death (Eisner et al., 2018; Lim et al., 2021; Martínez-Reyes and Chandel, 2020; Mills et al., 2017; Rambold et al., 2011). Mitochondrial structure modulates mitochondrial function. Changes in mitochondrial structure consistent with decreased mitochondrial fusion has been reported in several human diseases, including cardiovascular disease, Alzheimer's Disease, diabetes and cancer (Chen et al., 2011; Dai and Jiang, 2019; Zhu et al., 2013). Recent studies have shown that restoring balanced mitochondrial dynamics in disease models restores mitochondrial morphology and function (Bido et al., 2017; Ferreira et al., 2019; Franco et al., 2020; Rocha et al., 2018; Wang et al., 2017; Zhou et al., 2019).

Mitochondrial fusion and division are mediated by evolutionarily conserved dynamin superfamily proteins (DSPs). The mitochondrial outer membrane fusion machine is composed of two mitofusin paralogs anchored to the outer membrane (Mfn1 and Mfn2)(Santel and Fuller, 2001). Opa1 is another DSP that mediates inner membrane fusion, which is temporally linked to outer membrane fusion (Song et al., 2009). The importance of these processes in organismal health is highlighted by the fact that mutations in *MFN2* or *OPA1* lead to Charcot-Marie-Tooth Syndrome Type 2A (CMT2A) and Dominant Optic Atrophy (DOA), respectively (Alexander et al., 2000; Delettre et al., 2000; Stuppia et al., 2015; Züchner et al., 2004). CMT2A is caused by amino acid substitutions throughout Mfn2 and results primarily in a peripheral neuropathy that causes progressive loss of function and sensation in the extremities.

Although Mfn1 and Mfn2 are highly similar and can both individually mediate mitochondrial fusion, they possess important functional distinctions. We have shown that mitochondrial fusion is most efficient if both paralogs are present, highlighting that each mitofusin contributes unique functions to the fusion complex (Engelhart and Hoppins, 2019; Hoppins et al., 2011). Atomic resolution structures of mitofusin minimal catalytic domains (mini-mitofusin) revealed that both Mfn1 and Mfn2 possess a globular GTPase domain connected by a hinge domain (Hinge 2) to an extended helical bundle (HB1) (Fig. 1A) (Cao et al

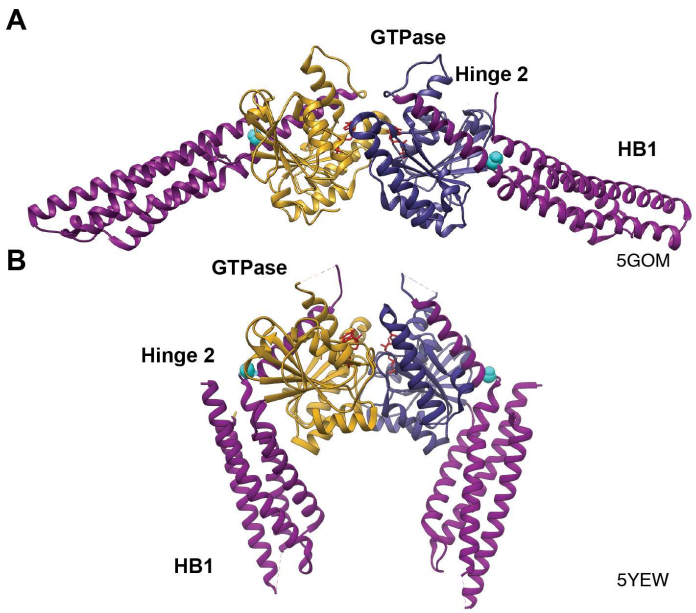

Figure 2.1 Structure of Mfn1

(A) Ribbon structure of $Mfn1_{IM}$ dimer in the open conformation bound to GDP (PDB: 5GOM) with the GTPase domain of one protomer in goldenrod, the second GTPase domain in dark blue, helical bundle 1 (HB1) in magenta, S329 highlighted in cyan, and GDP in red. **(B)** Structure of $Mfn1_{IM}$ dimer in the closed conformation bound to transition state mimic GDP-BeF_3 in red (PDB: 5YEW).

2017; Li et al., 2019; Qi et al., 2016; Yan et al., 2018). A second predicted helical bundle (HB2) and transmembrane region are absent from these structures but are required for membrane fusion as the mini-mitofusin does not mediate lipid mixing. These structural data indicate that Hinge 2 undergoes a large conformational change that moves HB1 relative to the GTPase domain from an open to a closed state (Fig. 1, A & B)(Yan et al., 2018). Typical of DSPs, mitofusins also form an intermolecular GTPase domain interface (G-G interface) that is required for GTP hydrolysis (Antonny et al., 2016; Cao et al., 2017; Daumke and Roux, 2017; Li et al., 2019; Qi et al., 2016; Yan et al., 2018). Analysis of GTP hydrolysis by these minimal catalytic domains revealed that Mfn1 has higher catalytic activity compared to Mfn2 (Li et al., 2019), which may contribute to their unique membrane fusion properties.

DSPs couple GTP binding and hydrolysis to oligomerization and conformational changes that drive membrane remodeling (Antonny et al., 2016; Ford and Chappie, 2019; Gao and Hu, 2021; Praefcke and McMahon, 2004; Ramachandran and Schmid, 2018). Mitofusin oligomerization occurs in the same membrane, *in cis*, and across two distinct membranes, *in trans*. Both types of assembly are required for efficient mitochondrial fusion, but the molecular details are not well defined. The mitofusin *trans* complex

likely functions as a membrane tether, establishing physical contact between adjacent mitochondrial membranes (Brandt et al., 2016; Engelhart and Hoppins, 2019; Koshiba et al., 2004). Mitofusin oligomerizes in the same membrane upon GTP binding (Engelhart and Hoppins, 2019; Ishihara et al., 2004; Samanas et al., 2020). We have reported that some CMT2A mitofusin variants have defective *cis* oligomerization and reduced fusion activity, indicating that *cis* assembly is required for efficient fusion (Engelhart and Hoppins, 2019; Samanas et al., 2020). These variants were not defective for *trans* complex formation, suggesting that GTP-dependent *cis* oligomerization is not strictly required for formation of the *trans* complex but is required for efficient progression from tethering to membrane fusion. Mini-mitofusin inserted into liposomes supported proteoliposome clustering through formation of the G-G interface, leading to the model that mitofusin *trans* complex formation, and thus mitochondrial tethering, requires the G-G interface (Cao et al., 2017). The role of the conformational change mediated by Hinge 2 in membrane fusion is not known, but several CMT2A-associated mutations are localized in this region, including one of the most frequently reported variants, Mfn2^{R94Q} (Stuppia et al., 2015). In the context of the mini-mitofusin, this substitution interfered with formation of the closed conformational state, indicating that this is likely important for mitofusin function (Li et al., 2019; Yan et al., 2018).

Here we investigate the role of Hinge 2 in mitofusin-dependent mitochondrial fusion by characterizing a disease associated variant, Mfn2^{S350P} and the equivalent Mfn1^{S329P} variant (Chung et al., 2010). These proline variants do not possess fusion activity and block wild type mitofusin-mediated mitochondrial fusion. We find that expression of either mitofusin proline variant resulted in rapid, dramatic redistribution of mitochondria to the perinuclear space in both wild-type or mitofusin-null cells. The redistribution of mitochondria occurred independently of dynein-based transport but did require that the mitofusin proline variant could bind and hydrolyze GTP. Our data indicate that the mitofusin proline variant forms prolific and irreversible *trans* complexes throughout the mitochondrial network. We propose that wild-type mitofusin *cis*-dimers exist in a low energy state and that GTP binding and hydrolysis permits formation of a fusion-competent high energy state *trans* complex. Our data suggest that Hinge 2 supports a power stroke that advances the *trans* complex from tethering to membrane fusion.

2.3 Results

2.3.1 Expression of disease-associated variants of mitofusin results in perinuclear clusters of mitochondria

To assess the function of the mitofusin proline variants, we expressed mitofusin with a C-terminal mNeonGreen tag in mouse embryonic fibroblasts (MEFs) lacking either Mfn1 or Mfn2 and visualized mitochondrial morphology by fluorescence microscopy. Mfn1-null and Mfn2-null cells had a fragmented mitochondrial network when transduced with empty vector (Fig. 2, A-D). When wild-type Mfn1 or Mfn2 ($Mfn1^{WT}$ or $Mfn2^{WT}$) were exogenously expressed in Mfn1-null or Mfn2-null MEFs respectively, reticular mitochondrial morphology was restored (Fig. 2, A-D). Interestingly, expression of $Mfn1^{S329P}$ led to an accumulation of mitochondria in the perinuclear space in 83.1±4.2% of cells (Fig. 2, A & B). Similarly, Mfn2-null cells expressing $Mfn2^{S350P}$ had perinuclear mitochondrial clustering in 78.4±6.4% of cells (Fig. 2, C & D). To determine if this effect was dominant, we expressed the mitofusin proline variants in wild-type MEFs.

As expected, transduction of empty vector, $Mfn1^{WT}$ or $Mfn2^{WT}$ did not alter the reticular mitochondrial structure, whereas expression of either $Mfn1^{S329P}$ or $Mfn2^{S350P}$ resulted in perinuclear clusters of mitochondria (Fig. 2, C & D). We observed that $Mfn1^{WT}$ and $Mfn2^{WT}$ were evenly distributed along mitochondria, with some mNeonGreen foci, while $Mfn1^{S329P}$ and $Mfn2^{S350P}$ expressing cells had many more mNeonGreen foci (Fig. 2, A & B lower panels).

We also examined the ultrastructure of mitochondria in cells expressing $Mfn1^{S329P}$ or $Mfn2^{S350P}$ using transmission electron microscopy (TEM). In wild-type MEFs, cristae have a regular electron dense pattern and individual mitochondria are spread throughout the cytoplasm (Fig. 2, E). As expected from our live-cell imaging, in Mfn1-null cells expressing $Mfn1^{S329P}$ or Mfn2-null cells expressing $Mfn2^{S350P}$, mitochondria were found proximal to the nucleus in TEM images. The mitochondria in cells expressing the mitofusin proline variant possessed cristae structures similar to wild-type, consistent with normal mitochondrial function. Together these observations of mitochondrial structure and ultra-structure indicate that substitution of $Mfn1^{S329}$ or $Mfn2^{S350}$ with proline results in redistribution of healthy mitochondria to the perinuclear region.

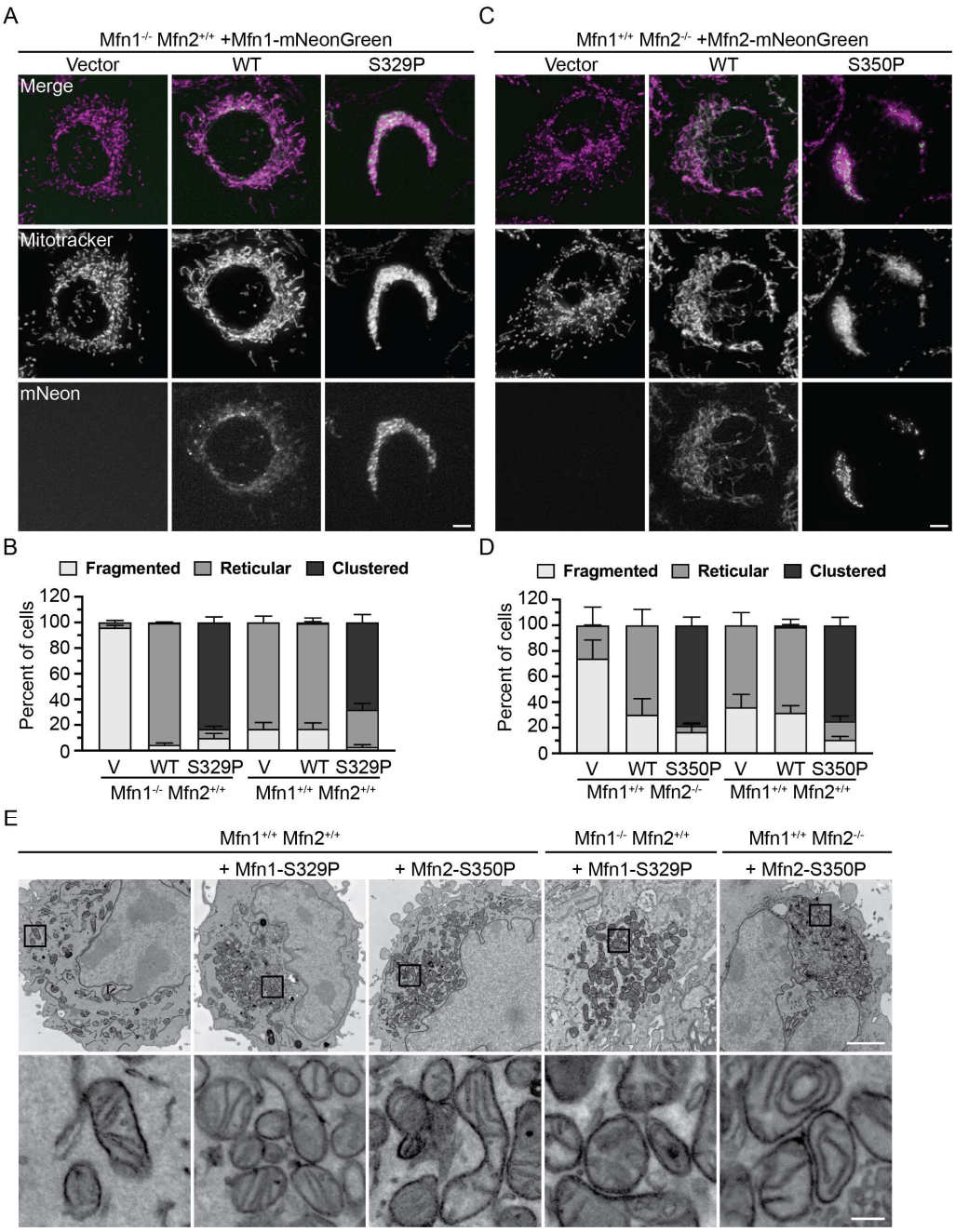

Figure 2.2 Expression of Mfn1S329P or Mfn2S350P cause perinuclear clustering of mitochondria.

(A) Representative images of Mfn1-null MEFs transduced with empty vector (V), Mfn1WT-mNeonGreen or Mfn1S329P-mNeonGreen. Mitochondria were labeled with Mitotracker Red CMXRos and visualized with live cell fluorescence microscopy. Images represent maximum intensity projections. Scale bar = 5 μm. (B) Quantification of the mitochondrial morphology in the cell lines described in A. Error bars represent mean ± SEM from n=3 separate blinded experiments (>100 cells per experiment). (C) Representative images of Mfn2-null MEFs transduced with empty vector (V), Mfn2WT-mNeonGreen or Mfn2S350P-mNeonGreen. Mitochondria were labeled with Mitotracker Red CMXRos and visualized with live cell fluorescence microscopy. Images represent maximum intensity projections. Scale bar = 5 μm. (D) Quantification of the mitochondrial morphology in the cell lines described in C. Error bars represent mean ± SEM from n=3 separate blinded experiments (>100 cells per experiment). (E) Representative electron micrographs of the indicated MEFs cell lines. Scale bar = 2 μm. Lower panels show higher magnification from boxed area in upper panel. Scale bar = 0.2 μm.

2.3.2 Mfn1^{S329P} and Mfn2^{S350P} are dominant negative variants that do not support fusion alone and block fusion by wild-type mitofusin

Whether the mitochondria in cells expressing Mfn1^{S329P} or Mfn2^{S350P} are fragmented or reticular within the cluster cannot be discerned by fluorescence microscopy. To distinguish these possibilities, we assessed mitochondrial connectivity by quantifying the diffusion of photoactivatable GFP targeted to the mitochondrial matrix (mt-paGFP). Following activation of mt-paGFP inside a small fraction of mitochondria within the network, we followed mt-paGFP diffusion and spread throughout the network for 50 minutes. We first assessed mitochondrial network connectivity in Mfn1-null or Mfn2-null cells to determine if the mitofusin proline variants supported mitochondrial fusion. We quantified the fraction of the mitochondrial network with GFP positive pixels immediately following photoactivation and 50 minutes later. In cells with low rates of fusion, we expected the fraction to be similar at both time points. In contrast, mitochondrial fusion would promote spread and diffusion of mt-paGFP, thus the fraction of mitochondria with GFP positive pixels was expected to increase. In Mfn1-null MEFs transduced with empty vector, the mitochondrial network was fragmented and the fraction of the network with mt-paGFP positive pixels increased by 1.30±0.20 fold over 50 minutes (Fig. 3, A & C). The results were similar in Mfn2-null cells transduced with empty vector, where the fraction the mitochondrial network with mt-paGFP positive pixels increased 1.51±0.15 fold over the time course (Fig. 3, B & D). In contrast, Mfn1-null cells expressing Mfn1^{WT} and Mfn2-null cells expressing Mfn2^{WT} both had reticular mitochondria and after 50 minutes, the fraction of the network with mt-paGFP increased 2.79±.23-fold and 3.04±0.20 fold, respectively (Fig. 3, A-D). These data are consistent with relatively low fusion rates in either Mfn1-null or Mfn2-null cells and increased fusion activity following expression of wild-type mitofusin. In Mfn1-null cells expressing Mfn1^{S329P}, the proportion of the mitochondrial network with mt-paGFP positive pixels increased by 1.43±0.15 fold over 50 minutes (Fig. 3, A & C). Similarly, in Mfn2-null cells expressing Mfn2^{S350P}, the fraction of mitochondria with mt-paGFP pixels increased by 1.48±0.08 fold over the time course (Fig. 3, B & D). Therefore, the diffusion of mt-paGFP in Mfn1-null or Mfn2-null cells expressing either proline variant was similar to the vector controls. These results indicate that Mfn1^{S329P} and Mfn2^{S350P} are unable to support fusion of mitochondria.

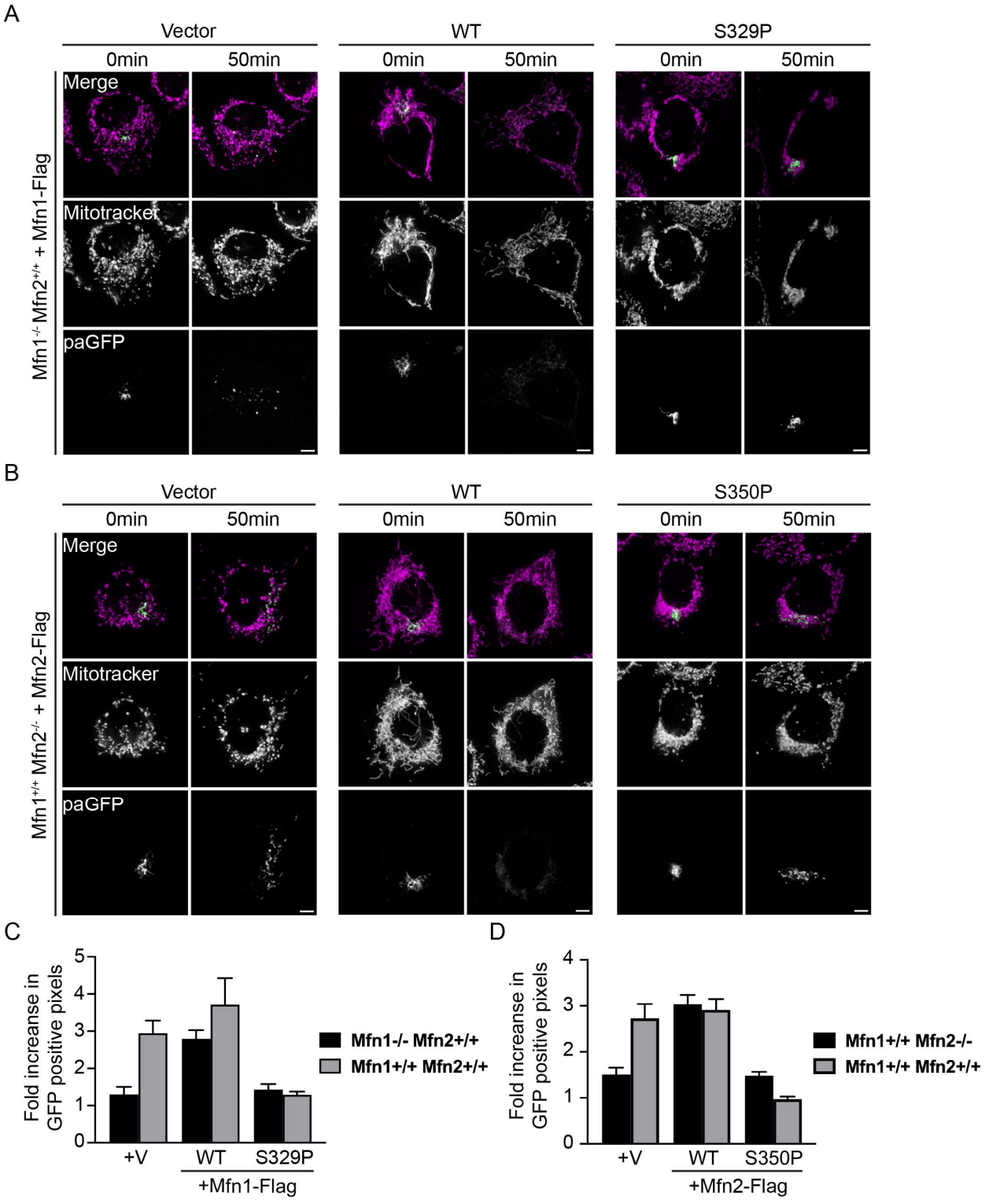

Figure 2.3 Mitochondrial clusters induced by proline variants do not have connected mitochondrial network.

(A) Representative images of Mfn1-null MEFs expressing mt-paGFP and transduced with empty vector (V), $Mfn1^{WT}$-Flag or $Mfn1^{S329P}$-Flag either 0 min or 50 min after activation of mt-paGFP with 405 nm laser, which is time = 0. Mitochondria were labeled with Mitotracker Red CMXRos and visualized with live cell fluorescence microscopy. Images represent maximum intensity projections. Scale bar = 5 μm. **(B)** Representative images of Mfn2-null MEFs expressing mt-paGFP and transduced with empty

vector (V), Mfn2^{WT}-Flag or Mfn2^{S350P}-Flag either 0 min or 50 min after activation of mt-paGFP with 405 nm laser, which is time = 0. Mitochondria were labeled with Mitotracker Red CMXRos and visualized with live cell fluorescence microscopy. Images represent maximum intensity projections. Scale bar = 5 µm. **(C)** Quantification of the diffusion of mt-paGFP in the cell lines described in A. Error bars represent mean ± SEM. n=6/7 cells over 2 independent experiments. **(D)** Quantification of the diffusion of mt-paGFP in the cell lines described in B. Error bars represent mean ± SEM. N=9-11 cells over 3 independent experiments.

Next, we determined whether mitochondrial fusion by endogenous mitofusin was affected by expression of the proline variants by analyzing diffusion of mt-paGFP in wild-type MEFs expressing either Mfn1^{S329P} and Mfn2^{S350P}. Wild-type MEFs transduced with empty vector have reticular mitochondrial morphology and the fraction of mt-paGFP pixels in the mitochondrial network increased approximately 3-fold over 50 minutes (Fig. 3, C & D, and SFig. 51 & 52). Expression of either Mfn1^{WT} or Mfn2^{WT} did not significantly change the diffusion of mt-paGFP in wild-type cells. In contrast, expression of either Mfn1^{S329P} or Mfn2^{S350P} significantly reduced diffusion of mt-paGFP (1.29±0.09 and 0.97-±0.06-fold increase, respectively) (Fig. 3, C & D and Ss1 & 52). The reduction in mt-paGFP diffusion compared to vector controls in wild-type cells indicates that Mfn1^{S329P} and Mfn2^{S350P} prevent fusion by wild-type mitofusins, and therefore possess dominant negative activity.

2.3.3 Formation of mitochondrial clusters is rapid and specific to mitochondria

Mitochondrial perinuclear clusters have been observed under other conditions, such as in cells drastically overexpressing mitofusin, cells expressing a truncated mitofusin lacking the GTPase domain, cells expressing some CMT2A variants of Mfn2 and cells overexpressing mitoPLD or mitoguardin (Choi et al., 2006; El Fissi et al., 2018; Huang et al., 2007; Koshiba et al., 2004; Santel and Fuller, 2001; Zhang et al., 2016). These mitofusin-dependent perinuclear clusters have been attributed to excessive mitochondrial tethering via mitofusin *trans* complex formation, although this has not been tested. Alternatively, under certain conditions, accumulation of mitochondria in the perinuclear space has been reported to depend on microtubule-based transport by dynein (Agarwal and Ganesh, 2020; Al-Mehdi et al., 2012). To study the molecular basis of the formation of the mitofusin proline variant-induced mitochondrial clusters, we expressed FLAG-tagged mitofusin from a tetracycline (TET)-inducible promoter in HEK293 Flp-In TREx cells to allow temporal control in our experiments.

In addition to the mitofusin proline variants, we also included the CMT2A variant Mfn2^{R94Q} in these analyses as it was previously reported to result in perinuclear clusters in neurons (El Fissi et al., 2018; Zhou et al., 2019). R94 is also located in Hinge 2, on a different helix than S350, and is therefore a useful

reference for Hinge 2 function (SFig. 5.3). R94Q is one of the most frequently reported amino acid substitution in CMT2A patients and has been extensively characterized (Cartoni et al., 2010; Detmer and Chan, 2007; El Fissi et al., 2018; Franco et al., 2020; Misko et al., 2010; Misko et al., 2012; Zhou et al., 2019). Interestingly, mitochondria in the axons of cultured DRG neurons expressing $Mfn2^{R94Q}$ have decreased retrograde and anterograde transport (Misko et al., 2010). Here we show that cells with vector only or cells expressing $Mfn1^{WT}$, $Mfn2^{WT}$ with 0.2 µg/mL TET for 4 hours possessed reticular mitochondria that were indistinguishable from cells incubated without TET (Fig. 4, A & B). Expression of $Mfn1^{S329P}$, $Mfn2^{S350P}$, or $Mfn2^{R94Q}$ resulted in rapid perinuclear clustering of mitochondria under the same conditions, although to different degrees (Fig. 4, A & B). $Mfn1^{S329P}$ expression resulted in perinuclear collapse of the mitochondrial network in almost all cells, while the change in distribution was observed closer to half the cells expressing $Mfn2^{S329P}$ or $Mfn2^{R94Q}$. To determine if these distinctions were due to different protein expression, we examined protein levels by Western blot analysis of whole cell protein extract. We found that $Mfn1^{WT}$ and $Mfn1^{S329P}$ were expressed at similar levels, 2.3X and 2X, respectively, compared to endogenous Mfn1 levels observed in vector controls (SFig. 5.4, A). $Mfn2^{WT}$, $Mfn2^{S350P}$, and $Mfn2^{R94Q}$ were also expressed at similar levels, at 7.1X, 6.2X and 6.7X endogenous Mfn2 levels, respectively (SFig. 5.4, B). Together, our results demonstrate that the redistribution of mitochondria to the perinuclear space occurs rapidly following expression of the mitofusin proline variant and that $Mfn1^{S329P}$ is more effective at evoking the redistribution of mitochondria.

We visualized lysosomes and ER in cells expressing the mitofusin proline variants following induction by TET to determine if the expression of $Mfn1^{S329P}$ or $Mfn2^{S350P}$ alter the distribution of other organelles in addition to mitochondria. In cells expressing $Mfn1^{WT}$ or $Mfn2^{WT}$, lysosomes appear as small puncta distributed throughout the cytoplasm. This distribution was not changed in cells expressing $Mfn1^{S329P}$ or $Mfn2^{S350P}$ (SFig. 5.5). TREx cells were transfected with Sec61-GFP to visualize the structure of the ER, which was similar in cells expressing wild-type mitofusin and either proline variant (SFig. 5.6). These data demonstrate that the mitofusin proline variants do not induce global perinuclear clustering of organelles but have a specific effect on mitochondrial distribution.

2.3.4 Perinuclear clustering of mitochondria is not dependent on mitochondrial transport by dynein

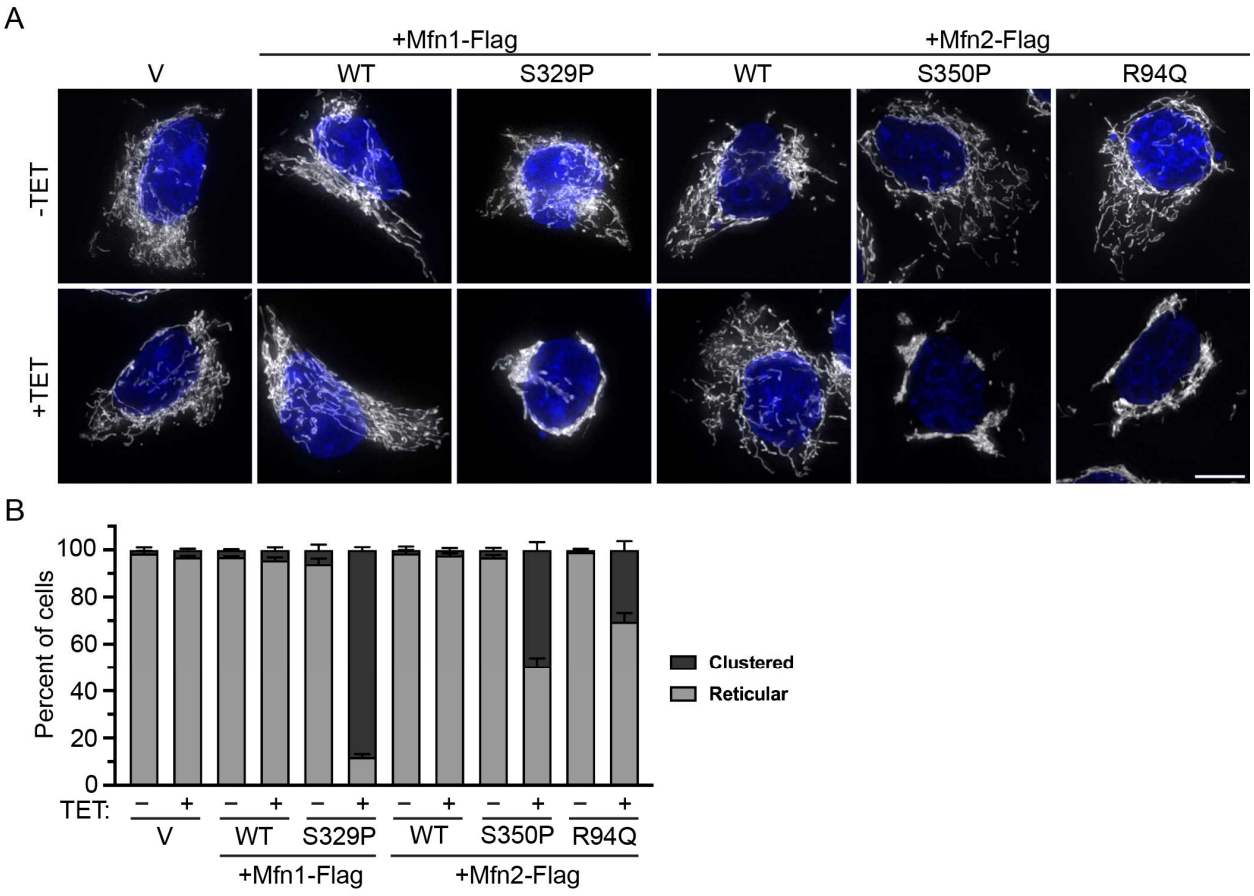

Figure 2.4 Mitofusin proline variants induce rapid perinuclear clustering of mitochondria.

(A) Representative images of Flp-In TREx HEK293 expressing the indicated mitofusin variant following induction of expression by incubation with 0.2 µg/mL TET for 4 hrs. Mitochondria were labeled with Mitotracker Red CMXRos, nuclei were labeled with NucBlue and visualized with live cell fluorescence microscopy. Images represent maximum intensity projections. Scale bar = 5 µm. **(B)** Quantification of the mitochondrial morphology in the cell lines described in A. Error bars represent mean ± SEM from n=3 separate blinded experiments (>100 cells per experiment).

Our data could be consistent with a model in which mitochondria that possess mitofusin proline variants have altered microtubule-based transport, driving mitochondria toward the perinuclear space. Adaptor proteins on the mitochondrial surface recruit dynein, which directs retrograde movement of mitochondria on microtubules toward the nucleus, and kinesin, which is responsible for anterograde movement toward the cell periphery (Kruppa and Buss, 2021). To determine if mitochondrial perinuclear clusters require dynein-dependent transport on microtubules, we induced expression of mitofusin in the TRex cells in the presence of nocodazole, which depolymerizes microtubules. Immunohistochemical staining confirmed that microtubules were fully depolymerized (SFig. 5.7). Cells expressing $Mfn1^{WT}$ or $Mfn2^{WT}$ had predominantly reticular mitochondria that were distributed throughout the cytosol in the presence or absence of

nocodazole (Fig. 5, A & B). In contrast, in cells expressing Mfn1^{S329P}, Mfn2^{S350P}, or Mfn2^{R94Q} we observed formation of perinuclear clusters similar to control cells without nocodazole (Fig. 5, A & B). Interestingly, the shape of the mitochondrial cluster is slightly different in nocodazole-treated cells where the mitochondria appear to be more compactly arranged and for Mfn2 variants, slightly more cells had mitochondria in perinuclear clusters.

These data suggest that mitochondrial perinuclear clusters that form upon expression of these mitofusin variants is independent of microtubule transport. To further support this conclusion, we knocked down expression of dynein heavy chain (DHC) using shRNA in the TET-inducible cells. To determine shRNA efficiency, we performed Western Blot analysis of whole cell lysates and observed that DHC protein levels were reduced 80-90% compared to cells treated with control shRNA against LacZ (Fig. 5, C). Mitochondrial morphology in cells expressing Mfn1^{WT} or Mfn2^{WT} looked similar in DHC knock down cells and the LacZ controls. Furthermore, expression of Mfn1^{S329P}, Mfn2^{S350P}, or Mfn2^{R94Q} led to perinuclear clustering of mitochondria in cells with reduced DHC expression and LacZ controls (Fig. 5, D & E). We note that there is a slight trend toward fewer clusters with reduced expression of DHC, suggesting that dynein activity may contribute to perinuclear localization of mitochondria to some extent, but it is not statistically significant. Together, our data indicate that mitochondrial perinuclear clustering due to CMT2A mitofusin variants is not dependent on dynein-directed microtubule-based transport.

2.3.5 Mfn1^{S329P}- and Mfn2^{S350P}-induced mitochondrial clusters requires GTP hydrolysis.

Our data demonstrate that the mitofusin proline variants do not support fusion and block fusion by wild-type mitofusin while also leading to the accumulation of mitochondria in the perinuclear space independent of microtubule-based transport. This is consistent with a model where the proline variant engages in abundant *trans* complexes that are irreversible and cannot progress to membrane fusion. To test this model, we evaluated the role of GTP binding and hydrolysis in the function of the mitofusin proline variants.

GTP hydrolysis requires formation of the mitofusin G-G interface (Cao et al., 2017; Li et al., 2019; Qi et al., 2016; Yan et al., 2018). The Mfn1^{R73D} variant of the mini-mitofusin failed to form the G-G interface, which suggests that changes in Hinge 2 can impair GTP hydrolysis by interfering with the formation of this

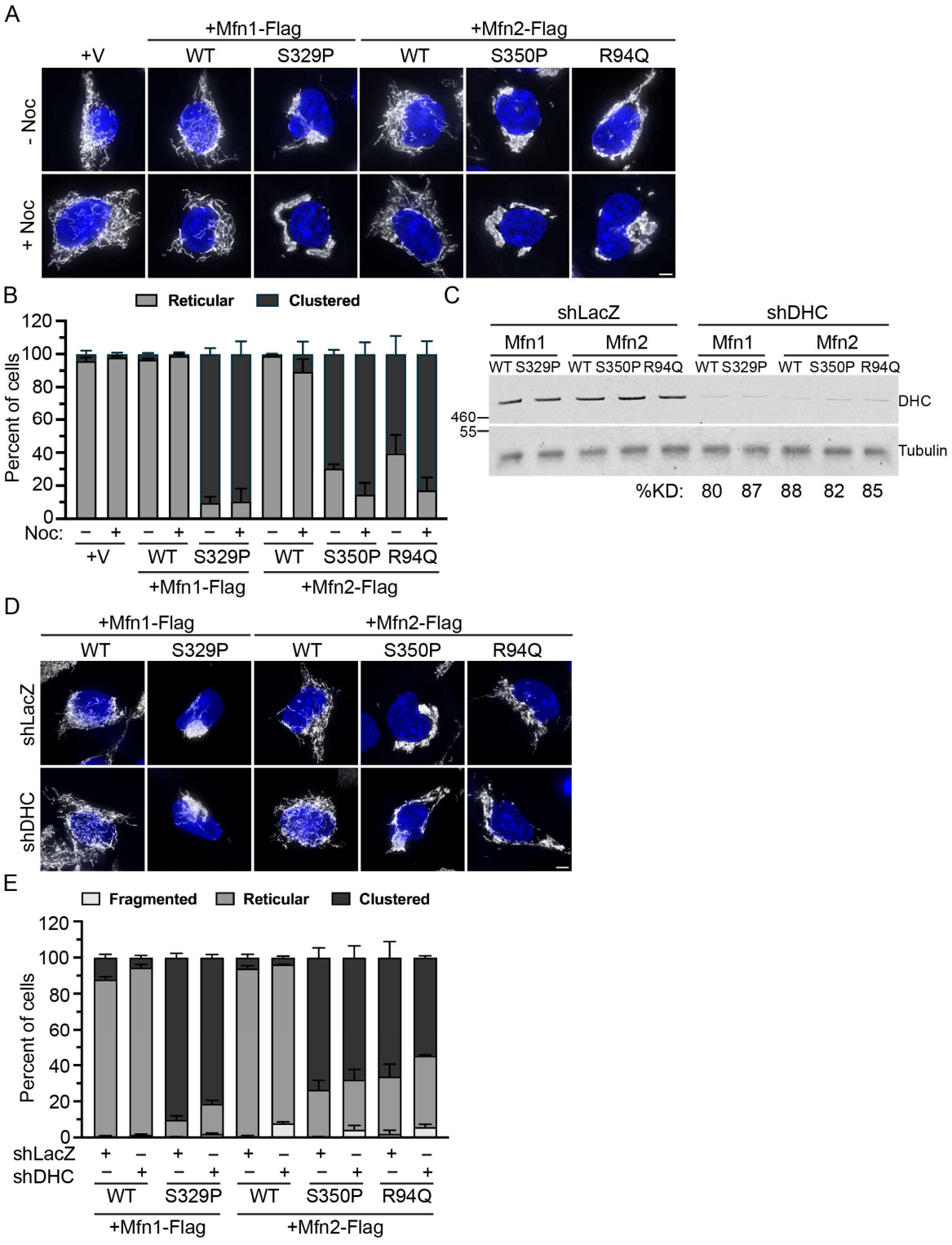

Figure 2.5 Perinuclear clustering of mitochondria by proline variant are not dependent on dynein-mediated microtubule-based transport.

A) Representative images of Flp-In TREx HEK293 expressing indicated mitofusin variant following induction of expression by incubation with 0.2 µg/mL TET for 4 hrs in the presence or absence of 5 nM nocodazole. Mitochondria were labeled with Mitotracker Red CMXRos, nuclei were labeled with NucBlue and visualized by live cell fluorescence microscopy. Images represent maximum intensity projections. Scale bar = 5um. **(B)** Quantification of the mitochondrial morphology in the cell lines described in A. Error bars represent mean ± SEM from n=3 separate blinded experiments (>100 cells per experiment). **(C)** Representative Western blot of α-

dynein heavy chain (DHC) and α-tubulin in whole protein extract from cells treated with either control shRNA (shLacZ) or shRNA against DHC (shDHC). Molecular weight markers are indicated in kDa on left. Percent knockdown (%KD) represents mean knockdown of DHC quantified by band intensities in Western blot normalized to whole protein stain. n=3. **(D)** Representative images of Flp-In TREx HEK293 with shLacZ or shDHC and expressing the indicated mitofusin variant following induction of expression by incubation with 0.2 µg/mL TET for 4 hrs. Mitochondria were labeled with Mitotracker Red CMXRos, nuclei were labeled with NucBlue and visualized by live cell fluorescence microscopy. Images represent maximum intensity projections. Scale bar = 5 µm. **(E)** Quantification of the mitochondrial morphology in the cell lines described in D. Error bars represent mean ± SEM from n=3 separate blinded experiments (>100 cells per experiment).

interface. Notably, a different amino acid substitution at the same position, Mfn1^{R73Q}, did not affect formation of the G-G interface, but this mini-mitofusin variant was unable to form the closed dimer, consistent with Hinge 2 function in this conformational change (Yan et al., 2018). To determine enzymatic activity of Mfn1^{S329P}, we used the internally modified Mfn1 (Mfn1$_{IM}$) that consists of residues 1-365 and 696-741 connected by a flexible linker (Cao et al., 2017). We found the kinetics of GTP hydrolysis was similar between Mfn1$_{IM}^{WT}$ and Mfn1$_{IM}^{S329P}$ (Fig. 6, A & B). This indicates that the proline substitution does not affect GTP binding or hydrolysis, which is triggered by formation of the G-G interface, and therefore these data indicate that the formation of the G-G interface is not altered by the proline substitution.

To determine if GTP hydrolysis is necessary for mitochondrial clustering in cells expressing the mitofusin proline variants, we altered GTPase activity in either Mfn1^{S329P} or Mfn2^{S350P} with amino acid substitutions known to disrupt the catalytic cycle at different steps. We expressed these variants in Mfn1-null or Mfn2-null cells so that we could assess mitochondrial fusion activity simultaneously. The P-loop of DSPs has a key lysine residue that has been well documented to allow GTP binding but disrupt GTP-hydrolysis when substituted with alanine (Chappie et al., 2010; Smirnova et al., 1998; Tornabene et al., 2020; van der Bliek et al., 1993). When this substitution is made in Mfn1 (Mfn1^{K88A}), the variant lacks GTPase activity and another substitution at this site (Mfn1^{K88T}) did not support fusion in Mfn1-null cells (Chen et al., 2003; Qi et al., 2016). As expected, we found that expression of Mfn1^{K88A} in Mfn1-null cells failed to rescue mitochondrial morphology as 97.9±1.3% of cells possessed fragmented mitochondria (Fig. 6, C & E). When Mfn1$^{K88A\text{-}S329P}$ was expressed in Mfn1-null cells, the mitochondrial network also remained fragmented in most cells (75.1±3.0%). Significantly, very few of the cells possessed clustered mitochondria (22.9±2.5%) compared to cells expressing Mfn1^{S329P} (75.9±3.4%) (Fig. 6, C & E). Similarly, most Mfn2-null cells expressing Mfn2^{K109A} had fragmented mitochondrial networks (Fig. 6, D & F). In contrast, more than half of the Mfn2-null cells expressing Mfn2$^{K109A\text{-}S350P}$ had reticular mitochondria (62.7±12.3%) and very few exhibited perinuclear clustering of mitochondria (Fig. 6, D & F). The fact that we observe Mfn2-null cells

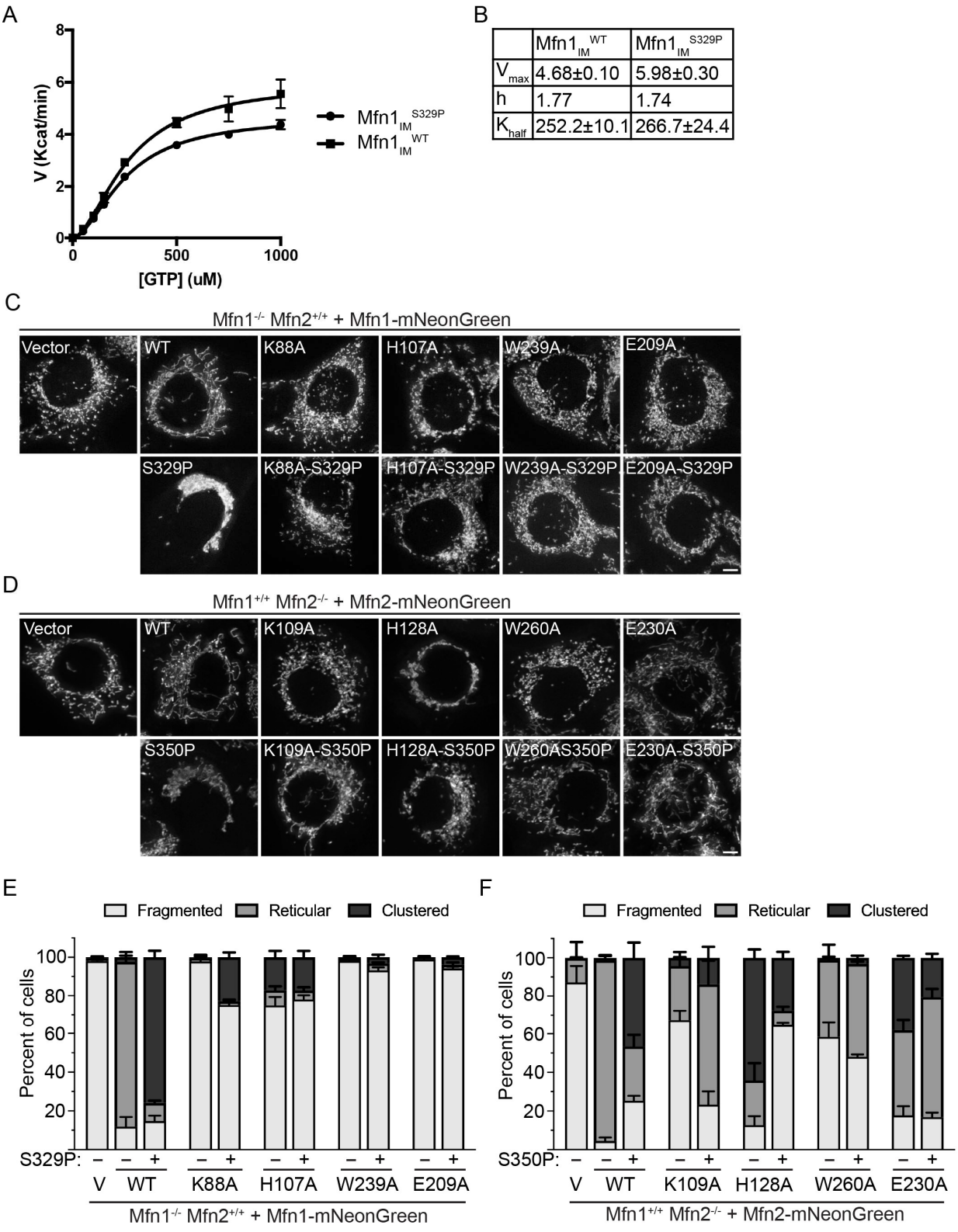

	$Mfn1_{IM}^{WT}$	$Mfn1_{IM}^{S329P}$
V_{max}	4.68±0.10	5.98±0.30
h	1.77	1.74
K_{half}	252.2±10.1	266.7±24.4

Figure 2.6 Mitofusin proline variants require GTPase activity to induce perinuclear clustering of mitochondria.

A) A kinetic plot of GTP hydrolysis of $Mfn1_{IM}^{WT}$ and $Mfn1_{IM}^{S329P}$ fit to an allosteric sigmoidal equation. **(B)** Table of kinetic parameters for $Mfn1_{IM}^{WT}$ and $Mfn1_{IM}^{S329P}$: Maximum velocity (V_{max}), Hill coefficient (h) and Michaelis-Menten constant (K_{half}). **(C)**

Representative images of Mfn1-null MEFs expressing indicated Mfn1-mNeonGreen variant. Mitochondria were labeled with Mitotracker Red CMXRos and visualized with live cell fluorescence microscopy. Images represent maximum intensity projections. Scale bar = 5 μm. **(D)** Representative images of Mfn2-null MEFs expressing indicated Mfn2-mNeonGreen variant. Mitochondria were labeled with Mitotracker Red CMXRos and visualized with live cell fluorescence microscopy. Images represent maximum intensity projections. Scale bar = 5 μm. **(E)** Quantification of the mitochondrial morphology in the cell lines described in C. Error bars represent mean ± SEM from n=3 separate blinded experiments (>100 cells per experiment). **(F)** Quantification of the mitochondrial morphology in the cell lines described in D. Error bars represent mean ± SEM from at least n=3 separate blinded experiments (>100 cells per experiment).

with reticular mitochondrial network upon expression of $Mfn2^{K109A-S350P}$ indicates that this variant can support fusion in the presence of $Mfn1^{WT}$ and reveals that the proline substitution at S350 does not block fusion activity of Mfn2 in this context. These data show that GTP hydrolysis is necessary for perinuclear clustering of mitochondria in cells expressing $Mfn1^{S329P}$ or $Mfn2^{S350P}$.

To determine if GTP hydrolysis, but not GTP binding, is necessary for mitochondrial clustering, we targeted H107, which has been suggested to have a role in charge compensation within the GTP binding pocket. Substitution of alanine at H107 permitted GTP to bind but prevented hydrolysis (Cao et al., 2017). Of note, other structural studies suggest that H107 points away from the binding pocket, which could imply a different or additional role for H107 in catalysis (Yan et al., 2018). It has been reported that expression of either $Mfn1^{H107A}$ or $Mfn2^{H128A}$ in cells lacking both mitofusins (Mfn1/2-null cells) resulted in an abnormal mitochondrial network, which included some perinuclear clusters (Cao et al., 2017). When we expressed $Mfn1^{H107A}$ in Mfn1-null cells, we observed primarily fragmented mitochondria (74.9±4.4%) with a small degree of mitochondrial clustering in the perinuclear region (17.1±3.3%). The difference between our data and previous results could be due to expression in Mfn1-null cells rather than Mfn1/2-null cells, or a difference in the degree of overexpression. With expression of $Mfn1^{H107A-S329P}$ in Mfn1-null cells, we observed that 78.1±2.2% of cells had fragmented mitochondria and 17.3±3.3% had mitochondrial clustering, similar to $Mfn1^{H107A}$ alone (Fig. 6, C & E). With expression of $Mfn2^{H128A}$ in Mfn2-null cells, we observed more than half of the cells with perinuclear clustering (64.1±4.4%), similar to reports following expression in Mfn1/2-null cells (Cao et al., 2017). Interestingly, few Mfn2-null cells expressing $Mfn2^{H128A-S350P}$ possessed clustered mitochondria (27.6±3.0%)(Fig. 6, D & F). These data further highlight functional differences between the mitofusin paralogs and indicate that the mitofusin proline variants must possess GTP hydrolysis activity to induce perinuclear clustering of mitochondria.

To determine if GTP binding is necessary for clustering of mitochondria by the proline variants, we made $Mfn1^{W239A}$, which has been shown to abolish GTP binding in the mini-Mfn1 (Cao et al., 2017). A

subsequent atomic structure of mini-Mfn1 suggested that W239 may also have a role in stabilizing the G-G interface (Yan et al., 2018). In the mini-Mfn2 structure, W260 was facing away from the nucleotide binding pocket, which the authors proposed facilitates GTP binding (Li et al., 2019). In Mfn1-null cells expressing Mfn1^{W239A}, the mitochondria were fragmented in the vast majority of cells, similar to previous reports (Cao et al., 2017). Mfn1-null cells expressing of Mfn1$^{W239A-S329P}$ also possessed primarily fragmented mitochondrial networks (Fig. 6, C & E). Expression of Mfn2^{W260A} or Mfn2$^{W260A-S350P}$ in Mfn2-null cells resulted in a partial rescue of mitochondrial morphology, consistent with previous reports that the W260A variant can support some mitochondrial fusion (Engelhart and Hoppins, 2019; Sloat et al., 2019). Neither Mfn2^{W260A} or Mfn2$^{W260A-S350P}$ induced perinuclear clustering in Mfn2-null cells (Fig. 6, D & F). These data indicate that GTP binding is also necessary for perinuclear clustering of mitochondria induced by expression of the proline variants.

The G-G interface is stabilized by an intermolecular salt bridge between E209 and R238 in Mfn1 (E230 and R259 in Mfn2). Disruption of this salt bridge by alanine substitutions allows GTP binding but inhibits GTP hydrolysis, resulting in loss of mitochondrial fusion activity as evidenced by fragmented mitochondria when expressed in Mfn1/2-null cells (Cao et al., 2017). To determine if the G-G interface is necessary for mitochondrial clustering induced by the mitofusin proline variants, we tested the effect of expression of Mfn1$^{E209A-S329P}$ on mitochondrial morphology in Mfn1-null cells. We observed that most cells expressing either Mfn1^{E209A} or Mfn1$^{E209A\ S329P}$ possessed fragmented mitochondria, consistent with no mitochondrial fusion activity (Fig. 6, C & E). In cells expressing either Mfn2^{E230A} or Mfn2$^{E230A-S350P}$, slightly more than half of the cells had reticular mitochondria, revealing mitochondrial fusion activity for both variants when Mfn1 is also present. Mfn2^{E230A} expression also resulted in some cells with perinuclear clusters of mitochondria, although less than Mfn2^{S350P} alone. Interestingly, Mfn2-null cells expressing Mfn2$^{E230A-S350P}$ possessed fewer mitochondrial perinuclear clusters compared to cells expressing Mfn2^{E230A} or Mfn2^{S350P} only (Fig. 6, D & F). Therefore, formation of the G-G interface is also necessary for perinuclear clustering of mitochondria caused by Mfn1^{S329P} or Mfn2^{S350P}. This may be due to the fact that this interface is required for GTP hydrolysis, or it could mean that the G-G interface is required to form the mitofusin *trans* complex. In sum, these data indicate that the proline variant mitofusins must possess a fully functional GTPase domain to alter the distribution of mitochondria in cells.

2.3.6 Nucleotide-dependent cis-assembly of Mfn1^{S329P} is reduced.

Mitofusins assemble into at least two distinct oligomers upon GTP binding. We have previously shown that other CMT2A-associated mitofusin variants with defects in mitochondrial fusion have impaired GTP-dependent assembly (Engelhart and Hoppins, 2019; Samanas et al., 2020). To assess the GTP-dependent assembly of Mfn1^{S329P}, we performed Blue-Native PAGE (BN-PAGE) of solubilized mitochondria that possess either Mfn1^{WT}-FLAG or Mfn1^{S329P}-FLAG. In the absence of additional nucleotide, Mfn1^{WT} exists predominantly as a single species that migrates with an estimated molecular weight of 200 kDa, which is consistent with a *cis* dimer (arrowhead, Fig. 7, A & B). We incubated mitochondria in the presence of the non-hydrolyzable GTP analog, GMP-PNP, which shifts mitofusin from the dimer into two larger species that migrate at ~320 kDa and ~450 kDa (Fig. 7, A & B, open and closed arrows). In the absence of nucleotide, Mfn1^{S329P} is indistinguishable from wild type, indicating that the *cis* dimer is not altered. In contrast, in the presence of GMP-PNP, very little Mfn1^{S329P} formed either the ~320 kDa or ~450 kDa species (Fig. 7, A & B, open and closed arrows). Given that the proline variant can bind and hydrolyze GTP in the context of Mfn1$_{IM}$, this indicates that Mfn1^{S329P} is deficient for GTP-dependent *cis*-oligomerization.

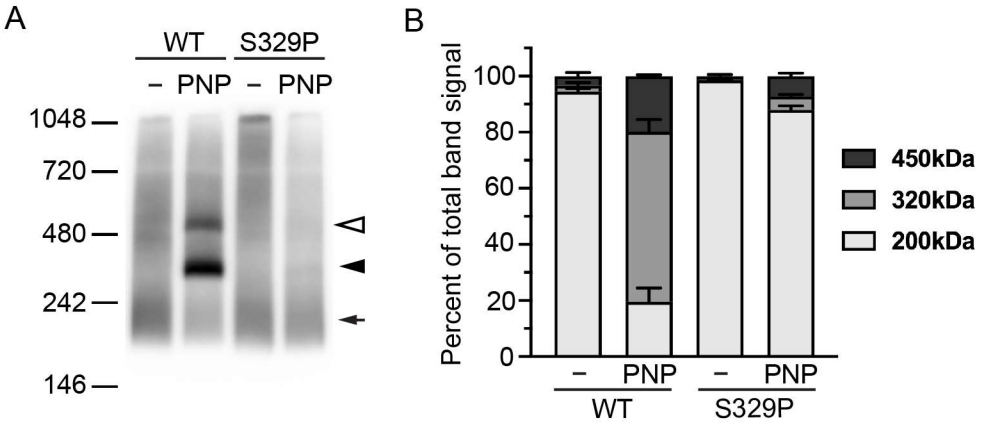

Figure 2.7 Mfn1^{S329P} is defective for GTP-dependent assembly.

(A) Representative BN-PAGE of mitochondrial isolated from Flp-In TREx cells expressing Mfn1^{WT}-Flag or Mfn1^{S329P}-Flag following induction of expression by incubation with 0.2 µg/mL TET for 4 hrs. Mitochondria were untreated or incubated in the presence or of GMP-PNP (PNP), followed by separation by BN-PAGE and immunoblotted with α-Flag antibody. Arrow indicates ~200 kDa species, closed arrowhead indicates ~320 kDa species, and open arrowhead indicates ~450 kDa species. Molecular weight markers are indicated in kDa on left. **(B)** Quantification of native mitofusin species indicated in A. Error bars represent mean ± SEM from n=3 separate experiments.

2.3.7 Mfn1^{S329P}- and Mfn2^{S350P}- induced perinuclear clusters require mitofusin *trans* assembly.

Our data are consistent with a model where these mitofusin variants cause unrestricted mitochondrial tethering in the cell such that virtually all mitochondria are connected via mitofusin complexes in *trans*. We predict that if stable *trans* interactions lead to mitochondrial clusters, we should block their formation by expressing a cytosolic variant of mitofusin. Under these conditions, mitochondrially anchored mitofusin would interact with cytosolic mitofusin rather than engaging in *trans* complexes, which would prevent the excessive mitochondrial tethering and perinuclear collapse (Fig. 8, A). To do this, we expressed a mitofusin variant shown to have primarily cytosolic localization, Mfn1^{F646D} (Huang et al., 2017). Of note, when Mfn1^{F646D} was observed in the mitochondrial outer membrane in cells, mitochondrial perinuclear clusters were reported by Huang. Following transfection of TREx cells with either eGFP-Mfn1^{F646D}, eGFP-Mfn1$^{F646D-S329P}$ or eGFP alone, expression of either Mfn1^{WT}-FLAG or Mfn1^{S329P}-FLAG was induced and mitochondrial structure was assessed in cells expressing cytosolic eGFP-Mfn1^{F646D} (Fig. 8, B & C). Cells expressing Mfn1^{WT}-FLAG and either eGFP-Mfn1^{F646D} or eGFP-Mfn1$^{F646D-S329P}$ had a negligible proportion of cells with mitochondrial perinuclear clusters compared to the eGFP-only control. As expected, most cells expressing Mfn1^{S329P} and eGFP had perinuclear mitochondrial clusters. In contrast, cells expressing Mfn1^{S329P} with cytosolic eGFP-Mfn1^{F646D} or eGFP-Mfn1$^{F646D-S329P}$ had significantly less mitochondrial clustering than cells without cytosolic mitofusin. The difference in the percent of cells with mitochondrial perinuclear clusters between eGFP-Mfn1$^{F646D-S329P}$ and eGFP-Mfn1^{F646D} could be due to trace amounts of mitofusin localizing to mitochondria in cells expressing eGFP-Mfn1$^{F646D-S329P}$. Our data indicate that perinuclear clustering of mitochondria that possess Mfn1^{S329P} is primarily the result of mitofusin interactions in *trans*, resulting in mitochondrial tethering and perinuclear collapse of the network.

2.4 Discussion

Taken together, our data demonstrate that amino acid substitutions in Hinge 2 of either mitofusin paralog can result in extensive mitochondrial tethering due to prolific and irreversible interaction of mitofusins on adjacent mitochondria. As a result, the mitochondrial network collapses to the perinuclear space. This change in mitochondrial distribution does not require dynein-dependent transport. In fact, we observed more cells with a perinuclear mitochondrial network when microtubules were depolymerized, suggesting

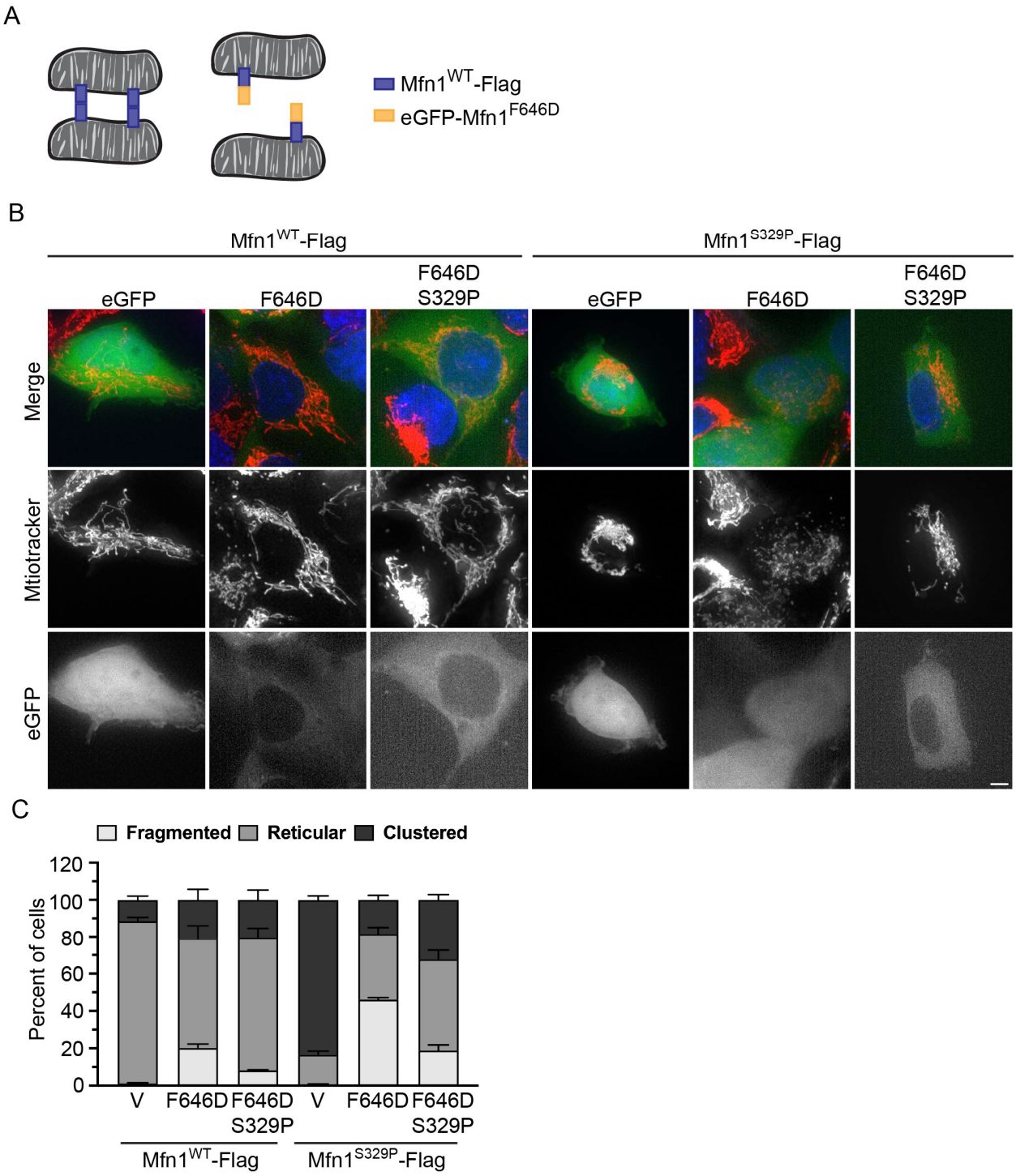

Figure 2.8 Cytosolic mitofusin blocks mitochondrial tethering by mitofusin proline variants.

(A) Schematic of mitochondria tethered by mitofusin *trans* complexes (left) and mitochondria with mitofusin *trans* complexes blocked by interaction with the cytosolic variant of mitofusin (F646D)(right). **(B)** Representative images of Flp-In TREx HEK293 transfected with eGFP, eGFP- Mfn1^{F646D} or eGFP-Mfn1$^{F646D-S329P}$ expressing either Mfn1^{WT}-Flag or Mfn1^{S329P}-Flag induced by incubation with 0.2 µg/mL TET for 4 hrs. Mitochondria were labeled with Mitotracker Red CMXRos, nuclei were labeled with NucBlue and visualized by live cell fluorescence microscopy. Images represent maximum intensity projections. Scale bar = 5 µm. **(C)** Quantification of the mitochondrial morphology in the cell lines described in B. Error bars represent mean ± SEM from n=3 separate blinded experiments (≥100 cells per experiment).

that attachment to microtubules may slow the collapse of the mitochondrial network to the perinuclear space. Previous studies have indicated that some CMT2A variants, including $Mfn2^{R94Q}$, reduce mitochondrial transport in axons by dynein and kinesin (Misko et al., 2010; Misko et al., 2012). Our data indicates that aberrant mitochondrial tethering could be another factor contributing to dysfunction of these variants.

The change in mitochondrial distribution evoked by expression of the mitofusin Hinge 2 variants requires GTP binding and hydrolysis, which indicates that mitochondrial tethering by the mitofusin *trans* complex requires GTP hydrolysis. For membrane division DSPs such as dynamin and DRP1, GTP hydrolysis is required to remodel the helical protein assembly, and contributes to the power stroke that constricts the target membrane, and to disassembly of the DSP oligomer (Antonny et al., 2016; Ford and Chappie, 2019). Our data indicate that mitofusin GTP hydrolysis is required to establish the *trans* complex, prior to the power stroke that would drive membranes together to induce lipid mixing. Our data are consistent with analysis of liposomes decorated with $Mfn1_{IM}$, which require the transition state mimic GDP-BeF_3 to form proteoliposome clusters via the G-G interface in *trans* (Cao et al., 2017). This is also consistent with one model for atlastin, a DSP responsible for ER membrane fusion, in which GTP hydrolysis leads to *trans* interactions across ER membranes (Byrnes et al., 2013; Liu et al., 2015).

Membrane fusion occurs through regulated assembly of dynamic protein complexes that change in tertiary and quaternary conformation. We have shown that mitofusin exists primarily as a dimer in the mitochondrial outer membrane, which likely corresponds to the diffuse pattern we observe with mitofusin-mNeonGreen expression. We propose that this *cis* dimer is in a low energy state and does not engage in *trans* complex formation. Our data suggest that GTP hydrolysis switches mitofusin to a high energy state that is competent to engage in *trans* complexes to tether mitochondria, which may be the mitofusin foci observed by fluorescence microscopy. The fact that amino acid substitutions in Hinge 2 prevent progression from membrane tethering to membrane fusion indicates that Hinge 2 functions in this step. Indeed, two distinct structures of mini-mitofusin indicate that Hinge 2 participates in a large conformational change from an open to a closed state. The proline substitution in Hinge 2 may interfere with these conformational dynamics.

We have previously characterized other CMT2A-associated mitofusin variants with amino acid substitutions in either the GTPase domain or within the predicted Hinge 1 domain that connects HB1 to a second helical bundle (HB2). All of these had reduced GTP-dependent oligomerization (Engelhart and Hoppins, 2019; Samanas et al., 2020). Here we report that the proline substitution at S329 in Hinge 2 also prohibits *cis* oligomerization but does not alter the steady state dimer. Given that these substitutions are found in three different structural domains of mitofusin, it is unlikely that all substitutions alter a single assembly interface. Therefore, our data suggest that GTP binding evokes allosteric changes in multiple mitofusin domains to expose *cis* oligomerization interfaces. Defects in mitofusin *cis* assembly correlate with decreased mitochondrial fusion activity (Engelhart and Hoppins, 2019; Samanas et al., 2020). Consistent with this, Mfn1^{S329P} and Mfn2^{S350P} lack fusion activity (Fig. 3). Unlike our previously characterized CMT2A variants, which were partial loss-of-function, Mfn1^{S329P} and Mfn2^{S350P} are complete loss-of-function and dominant negative (Fig. 3, C & D). This dominant negative effect is likely due to engaging wild-type mitofusin in a non-functional complex either in *cis* or in *trans*. When assembled as the steady state dimer with a wild type mitofusin, the proline variant could block GTP-dependent *cis*-oligomerization. If the proline variant assembled with wild-type mitofusin in *trans*, the proline variant would block progression from tethering to membrane fusion.

Consistent with the rapid mitochondrial tethering we observed, it has been previously reported that inter-mitochondrial contact events occur with relatively high frequency compared to mitochondrial fusion or division events (Wong et al., 2019). From live cell imaging analysis, Wong *et al* predicted that up to 30% of mitochondria in the cell were engaged in inter-mitochondrial contacts and the vast majority of these separated and moved away from each other. It is possible that when either Mfn1^{S329P} or Mfn2^{S350P} are present on the mitochondrial outer membrane, these contacts permit initiation of irreversible *trans* complexes that tether mitochondria together.

2.5 Materials and Methods

Plasmids and Cloning

The following plasmids were used in this study: pBABE-puro (Addgene #1764), mito-PAGFP (Addgene #23348), peGFP-N1 (Clontech), Sec61β-GFP (gift from Jodi Nunnari), pLKO.1-TRC (Addgene #10878), psPax2 (Addgene #12260), VSV-G (Addgene #8454). To create constructs containing mitofusin variants, mitofusin was cloned using Gibson assembly as previously described (Sloat et al., 2019). Variants were created using site-directed mutagenesis using Gibson assembly. Following digestion with DpnI to remove template DNA, the amplified DNA was transformed into Endura or DH5-alpha *Escherichia coli* cells and plasmids were purified from selected colonies. All plasmids were confirmed by sequence analysis.

Cell culture and transfection

All cells were grown at 37°C and 5% CO2 and cultured in DMEM (Thermo Fisher Scientific) containing 1X GlutaMAX (Thermo Fisher Scientific) with 10% fetal bovine serum (FBS; Seradigm). MEFs cells (Mfn wild type, Mfn1-null and Mfn2-null) were purchased from the American Type Culture Collection. Flp-In TREx Host cells (Invitrogen) were a gift from Nancy Maizels. Flp-In TREx cells were maintained in media containing 15 μg/mL blasticidin (Life Technologies) and 100 μg/mL zeocin (Invitrogen). Cells were tested for mycoplasma contamination by 4′,6-diamidino-2-phenylindole staining before each experiment.

Flp-In TREx HEK293 clonal populations were transfected with 1.5 μg peGFP-N1, 200 μL JetPRIME Buffer and 4 μL JetPRIME Transfection Reagent (Polyplus Transfection) for 4-6hrs. Experiments were performed 24hrs after transfection.

Retroviral transduction

Plat-E cells (Cell Biolabs) were maintained in complete media supplemented with 1 μg/ml puromycin and 10 μg/ml blasticidin and plated at ~80% confluency the day before transfection. 350,000 Plat-E cells were plated in a 6-well dish and the following day were transfected with pBABE plasmids (3 μg pBABE Mfn1 or empty vector; 1.5-3 μg pBABE Mfn2; 3 μg mito-paGFP) using FuGENE HD (Promega) and Opti-MEM reduced serum media (Gibco). Transfection reagent was incubated overnight before a media change. Viral supernatants were collected at approximately 48 and 72 hours post transfection and incubated with MEFs

in the presence of 8 µg/ml polybrene. Approximately 24 h after the last viral transduction, MEF cells were split and selection was added (1 µg/ml puromycin or 200 µg/ml hygromycin B).

Flp-In TREx Clonal Populations

300,000 Flp-In TREx HEK293 Host cells (Thermo Fisher Scientific) were seeded in a 6-well dish. Two days later, cells were co-transfected with 0.2 µg pFTSH (gift from Nancy Maizels) containing gene of interest and 1.8 µg pOG44 (Life Technologies) using 4 µL JetPRIME Transfection Reagent (Polyplus Transfection) for 4-6hrs. Cells were moved to two 10-cm dishes and allowed to recover for 2 days before adding selection to the media (200 µg/ml hygromycin B). Under selection, cells survived at low density and clones were collected onto sterile filter paper dots soaked in trypsin. Following expansion, whole cell extracts from clonal populations incubated with TET were screened by Western blot analysis for mitofusin against wild-type controls.

shRNA lentivirus

shRNA target sequences were obtained using the RNAi Consortium (TRC; Broad Institute). Oligonucleotides for shRNA against DHC (target sequence: 5'-CCCGTGATTGATGCAGATAAA-3') were purchased from Integrated DNA Technologies, annealed and ligated into pLKO.1 - TRC viral plasmid. shRNA against LacZ in pLKO.1 - TRC (target sequence: 5'-CGCGCCTTTCGGCGGTGAAAT-3') was a gift from Yasemin Sancak. One million HEK293T cells were seeded in 6 cm plates with 5 ml media. The next day, cells were transfected with 900 ng psPax2, 100 ng VSV-G, and 1000 ng viral plasmid in JetPRIME transfection reagent with JetPRIME buffer for 48 hrs. Viral supernatant was collected, passed through a 0.45 micron PES membrane filter and stored at -80°C. Flp-In TREx stable cell lines were seeded at 250,000 cells in a 6-well dish. The next day, viral supernatant was thawed at room temperature was added to cells with 8 µg/ml polybrene and incubated for 48 hrs. Cells were moved to a 10 cm dish and selection was added (1 µg/ml puromycin). Approximately three days later, cells were seeded onto no. 1.5 glass-bottomed dishes (MatTek) coated with 10 µg/mL fibronectin (Sigma-Aldrich) and were imaged two days later following incubation with 0.2 µg/mL tetracycline hydrochloride (Fisher Scientific) as described below.

Microscopy

All cells were plated ingrown on no. 1.5 glass-bottomed dishes (MatTek) for ~48 hours prior to imaging. Cells were incubated with 0.1 µg/ml Mitotracker Red CMX Ros with or without 3 drops NucBlue (Molecular Probes) for 15 min at 37°C with 5% CO_2. Following this, MEF cells were rinsed into complete media for at least 45 min before imaging and the Flp-In TREx cells were incubated with 0.2 µg/mL tetracycline hydrochloride (Fisher Scientific) for 4 hrs. A Z-series with a step size of 0.3 µm was collected with a Nikon Ti-E wide-field microscope with a 60 × NA (numerical aperture) 1.4 oil objective (Nikon), a solid-state light source (Spectra X; Lumencor), and an sCMOS camera (Zyla 5.5 megapixel). Each cell line was imaged on at least three separate occasions by a blinded experimentor (n > 100 cells per experiment).

Image analysis

Images were deconvolved using 15 iterations of 3D Landweber deconvolution. Deconvolved images were then analyzed using Nikon Elements software. Maximum intensity projections were created using ImageJ software (NIH). Mitochondrial morphology in mammalian cells was scored as follows: reticular indicates that fewer than 50% of the mitochondria in the cell were fragments (fragments defined as mitochondria less than 2.5 µm in length); fragmented indicates that most of the mitochondria in the cell were less than 2.5 µm in length; clustered indicates that the mitochondrial distribution was altered such that most mitochondria were coalesced in the perinuclear space. In MEF cells expressing mitofusin-mNeonGreen, only cells with GFP signal were scored. In MEF cells expressing Mfn2-mNeonGreen as described in Figure 6, only cells with GFP signal less than 1000 units were scored. All quantification was performed by a blinded experimenter.

Photoactivatable mitochondrial (mt)-GFP

Cells transduced with mito-paGFP (Addgene #23348) and either Mfn1-Flag pBabe-hygro or Mfn2-Flag-P2A-blasticidin pBabe were plated in No. 1.5 glass-bottomed dishes (MatTek). MEFs were incubated with 0.1 µg/ml MitoTracker Red CMXRos for 15 min at 37°C with 5% CO2, washed, and incubated with complete media for at least 45 min prior to imaging. MEFs were imaged at 37°C with 5% CO_2. A region that was ~1 μm^2 was activated using a 405 nm laser, and the same cell was imaged every 10 min for 50 min. Images were collected with a Nikon Ti-E widefield microscope with a 63x NA 1.4 oil objective (Nikon), a solid-state

light source (SPECTRA X; Lumencor), and an sCMOS camera (Zyla 5.5 Megapixel). Images were cropped and deconvolved using 15 iterations of 3D Landweber deconvolution on Offline Deconvolution software (Nikon). Data was then analyzed using Nikon NIS-Elements Analysis software. Background was removed and maximum intensity projections were created. Each channel was thresholded separately for each cell and the number of pixels that were both mCherry positive and GFP positive were recorded. Spread of paGFP was calculated as number of pixels that were both GFP and mCherry positive divided by total number of mCherry pixels after 50min divided by the same variable at 0min (immediately following activation). Graphs were created in Prism (Graphpad).

SDS-PAGE, Western blot analysis, and quantification

Whole cell protein lysates were obtained by resuspending PBS-washed cells in radioimmunoprecipitation assay (RIPA) lysis buffer (150 mM NaCl, 1% Nonidet NP-40, 1% sodium deoxycholate, 0.1% SDS, 25 mM Tris [pH 7.4], and 1× Halt Protease Inhibitor Cocktail, EDTA-free [Thermo Fisher Scientific]). The samples were incubated on ice for 5 min and then spun at 21,000x*g* for 15 min at 4°C. The supernatant was transferred to a clean tube, and protein concentration was measured by bicinchoninic acid assay (Thermo Fisher Scientific). Following separation by SDS-PAGE, proteins transferred to nitrocellulose were detected using primary rabbit or mouse antibodies and visualized with appropriate secondary antibodies conjugated to IRDye (Thermo Fisher Scientific). The following antibodies were used in this study: mouse monoclonal anti-FLAG (Sigma; 1:1000); mouse monoclonal anti-Mfn2 (Sigma clone 4H8; 1:1000); mouse monoclonal anti-alpha tubulin (Thermo Fisher Scientific clone DM1A; 1:5000); rabbit polyclonal anti-Mfn1 (gift from Jodi Nunnari, University of California, Davis; 1:500); and rabbit polyclonal anti-DYNC1H1 (Proteintech; 1:1000). Western blot images for expression of mitofusin in FLP-In TREx HEK293 cells were imaged on a LI-COR Imaging System (LI-COR Biosciences). Mitofusin band intensity was normalized to tubulin band intensity and compared to vector control in the presence of TET using LI-COR Analysis Software (LI-COR Biosciences). Western blot images for shRNA were acquired on Sapphire and quantification was performed with Azurespot. Knockdown quantification was normalized using whole protein stain (Azure Biosystems) and the mean was calculated from 3 separate western blots of three independent shRNA experiments.

Electron Microscopy

Cells were pelleted and fixed in 4% glutaraldehyde and 0.1 M sodium cacodylate buffer, pH 7.3 at room temperature overnight. Samples were imaged using JEOL 1230 transmission electron microscope (JEOL USA) operated at 80KV.

Preparation of mitochondria

For each experiment, three 15-cm plates of HEK293 Flp-In TREx cells were grown to ~90% confluency. Expression of mitofusin was induced by incubation with 0.2 µg/mL tetracycline hydrochloride (Fisher Scientific) for 4 hrs. Cells were harvested by cell scraping, pelleted, and washed in mitochondrial isolation buffer (MIB) (0.2 M sucrose, 10 mM Tris-MOPS, pH 7.4, 1 mM ethylene glycol-bis(β-aminoethyl ether)-N,N,N′,N′-tetraacetic acid). The cell pellet was resuspended in one cell pellet volume of cold MIB with 1x HALT protease inhibitor cocktail (Thermo Scientific) and 0.5 mM phenylmethylsulfonyl fluoride (Sigma-Aldrich), and cells were homogenized by ~12 strokes on ice with a Kontes-Potter-Elvehjem tissue grinder set at 350 rpm. The homogenate was centrifuged (400 × g, 5 min, 4°C) to remove nuclei and unbroken cells, and homogenization of the pellet fraction was repeated followed by centrifugation at 400 × g, 5 min, 4°C. The supernatant fractions were combined and centrifuged (7400 × g, 8 min, 4°C) to pellet a crude mitochondrial fraction. The crude mitochondrial pellet was resuspended in a small volume of MIB. Protein concentration of fractions was determined by Bradford assay (Bio-Rad Laboratories) and adjusted to 5 µg/uL.

Blue Native (BN)-PAGE

Isolated mitochondria (12.5 µg) were incubated with or without 2 mM GMP-PNP (Guanosine 5′-β,γ-imidotriphosphate trisodium salt hydrate; Sigma-Aldrich) as indicated at 37°C for 30 min. Mitochondria were then lysed in 1% wt/vol digitonin, 50 mM Bis-Tris, 50 mM NaCl, 10% wt/vol glycerol, 0.001% Ponceau S, pH 7.2, for 15 min on ice. Lysates were centrifuged at 16,000 × g at 4° C for 30 min. The cleared lysate was mixed with Invitrogen NativePAGE 5% G-250 sample additive to a final concentration of 0.25%. Samples were separated on a Novex NativePAGE 4–16% Bis-Tris Protein Gels (Invitrogen) at 4°C. Gels were run at 40 V for 30 min and then 100 V for 45-60 min with dark cathode buffer (1× NativePAGE Running Buffer [Invitrogen], 0.02% [wt/vol] Coomassie G-250). Dark cathode buffer was replaced with light cathode buffer (1× NativePAGE Running Buffer [Invitrogen], 0.002% [wt/vol] Coomassie G-250) and the gel was run

at 250 V for 60–75 min until the dye front ran off the gel. After electrophoresis was complete, gels were transferred to polyvinylidene fluoride membrane (Bio-Rad Laboratories) at 30 V for 16 h in transfer buffer (25 mM Tris, 192 mM glycine, 20% methanol). Membranes were incubated with 8% acetic acid for 15 min to fix the proteins to the membrane and then washed with dH_2O for 5 min. Membranes were dried at room temperature for 60 min and then rehydrated in 100% methanol and washed in dH_2O. Membranes were blocked in 4% milk for 20 min and were probed with anti-FLAG (Sigma) overnight at 4°C. Membranes were incubated with horseradish peroxidase-linked (HRP) secondary antibody (Cell Signaling Technology) at room temperature for 1 h. Membranes were developed in Radiance Plus Chemiluminescent HRP Substrate (Azure Biosystems) for 5 min and imaged on a Sapphire Biomolecular Imager (Azure Biosystems). Band intensities were quantified using AzureSpot analysis software (Azure Biosystems). NativeMark Unstained Protein Standard (Life Technologies) was used to estimate molecular weights of mitofusin protein complexes.

Protein expression and purification $Mfn1_{IM}$

$Mfn1_{IM}$ pET28 plasmid was obtained from Song Gao. Mutations were made by Gibson assembly and confirmed by sequencing. $Mfn1_{IM}$ constructs were expressed in *Escherichia coli* Rosetta (DE3) cells. Cells were cultured in Luria-Bertani medium with 150 µg/ml ampicillin and 25 µg/ml chloramphenicol at 37°C to an OD_{600} of ~0.6, and protein expression was induced by the addition of 100 µM isopropyl 1-thio-β-D-galactopyranoside. Induced cultures were grown overnight at ~17°C. The cells were harvested by centrifugation at 6,000 x g for 10 min. Cell pellets expressing $MFN1_{IM}$ were resuspended in 5 ml of PBS, pelleted by centrifugation at 6,000 x g for 5 min, frozen in liquid nitrogen, and stored at -80 °C. Cells were thawed in a room-temperature water bath and resuspended in 50 ml of 50 mM HEPES-KOH (pH 7.4), 400 mM NaCl, 5 mM $MgCl_2$, 30 mM imidazole, 1 mM phenylmethanesulfonylfluoride, 1x protease inhibitor mixture (Thermo Scientific), 2.5 mM β-mercaptoethanol (β-ME) and lysed using a microfluidizer (Avestin). The lysate was subjected to centrifugation at 14,000 rpm for 45 min. The supernatant was applied to 2.5 ml of HisPurTM Ni-NTA beads (Thermo Scientific) equilibrated with binding buffer 1 (20 mM HEPES-KOH (pH 7.4), 400 mM NaCl, 5 mM $MgCl_2$, 30mM imidazole (pH 8.0), 2.5 mM β-ME) and nutated at 4°C for 30 min. Ni-NTA beads bound to protein were washed with 20 column volumes of binding buffer 1, and proteins were eluted with elution buffer (20 mM HEPES- KOH (pH 7.4), 400 mM NaCl, 5 mM $MgCl_2$, 300 mM

imidazole, 2.5 mM β-ME). Mfn1$_{IM}$-containing elutions were incubated with 800 µg of GSHS-transferase (GST)-fused PreScission pro- tease to remove the N-terminal His6 tag. This was dialyzed overnight against binding buffer 2 (20 mM HEPES-KOH (pH 7.4), 400 mM NaCl, 5 mM MgCl2, 2.5 mM β -ME). After dialysis, PreScission protease was removed using a GST column. The protein was reapplied to a second Ni-NTA column equilibrated with binding buffer 2. Binding buffer 1 was used to elute the protein, which was subsequently loaded onto a Superdex200 16/60 column (GE Healthcare) equilibrated with gel filtration buffer (20 mM HEPES-KOH (pH 7.4), 150 mM NaCl, 5 mM $MgCl_2$, 1mM DTT). The protein eluted in a discrete peak corresponding to a molecular mass of ~50 kDa. Protein was concentrated on an Amicon Ultra Centrifugal Filter (molecular weight cutoff, 30,000) (Millipore) to 30 mg/ml, and glycerol was added to 20% before the protein was aliquoted and stored at -80°C. Protein purification was performed at 4°C. Protein concentration was determined by Bradford assay (Bio-Rad).

GTPase assay

Frozen protein was thawed on ice and diluted to 2.5 µM in 20mM HEPES-KOH (pH 7.4), 50 mM KCl, 5 mM $MgCl_2$, 1 mM DTT. Protein concentrations were confirmed by Bradford assay (Bio-Rad). Reactions were set up in triplicate in a 96-well plate on ice. Variable concentrations of GTP were added, and reactions were incubated at 37°C for 15 min. Reactions were stopped by adding 200 mM EDTA on ice. Concentrations of free inorganic phosphate (Pi) were measured by malachite green reagent, incubated at room temperature for 15 min. The optical density at 650 nm was measured, and a potassium phosphate standard curve was used to determine release of Pi by GTP hydrolysis. Data was analyzed in Prism (Graphpad).

Immunofluorescence

Cells were plated onto fibronectin-coated coverslips. Cells were incubated with 0.1 µg/ml Mitotracker Red CMX Ros for 15 min at 37°C with 5% CO2, then washed into compete media containing 1 µg/mL tetracycline hydrochloride (Fisher Scientific) +/- 5 nM nocodazole (Fisher Scientific) and incubated for 4 hours. Cells were fixed in 4% paraformaldehyde (Sigma-Aldrich) and 0.5% glutaraldehyde (Polysciences Inc.) for 15 min at room temperature, then solubilized in 0.1% Surfact-Amps TX-100/PBS (Thermo Scientific). Microtubules were stained using mouse monoclonal anti-alpha tubulin (Thermo Fisher Scientific clone DM1A; 1:300) and goat anti-mouse Alexa 488 secondary antibody (Invitrogen; 1:300).

Chapter 3. Method Development for Measuring Conformational Changes in Mitofusin

3.1 Introduction

Mitochondrial outer membrane fusion is expected to require large conformational changes of the mitofusin protein. Recent studies using the mini-mitofusin described in chapter 2 have identified two conformational states adopted by mitofusin based on the nucleotide binding state (Yan et al, 2018). When crystalized with GDP in the nucleotide binding pocket, Mfn1 adopts the open conformation in which the α helices extending from HB1 into the GTPase domain remains intact. In the presence of GDP-BeF_3, Mfn1 adopts the closed conformation which introduces a ~77-degree bend in the α-helices (Figure 3.1 A). The site of this bend is identified as Hinge 2. In our previous studies described in chapter 2, we identified alterations to this hinge in Mfn1 by $Mfn1^{S329P}$ leads to perinuclear collapse of mitochondria due to increased tethering by mitofusin interacting in trans. Our studies revealed that GTP hydrolysis is necessary for the formation of the mitofusin tether. This suggests changes in conformation around Hinge 2 are required for transitioning from tether to fusion, but this hypothesis has yet to be tested. The current research on conformations adopted by mitofusin around Hinge 2 have been conducted using purified mini-mitofusin (Cao et al, 2017; Yan et al, 2018). Mitofusin is predicted to have at least one additional hinge, Hinge 1, between helical bundle 1 and helical bundle 2 (Samanas et al., 2020). Due to the lack of purified full length protein containing Hinge 1, the same techniques cannot be used to elucidate conformational changes around Hinge 1. Additionally, it is unknown how Hinge 2 behaves in the context of full-length protein. In order to assess native conformational changes of mitofusin during mitochondrial fusion, methods for analyzing conformational changes in full-length protein must be developed.

Anap Cyclen-Cu^{2+} resonance energy transfer (ACCuRET) is a recently developed technique to assess conformational changes in purified protein based on the principles of transmission metal ion fluorescence resonance energy transfer (tmFRET) (Gordon et al, 2018). With ACCuRET, the noncanonical amino acid, L-Anap, is incorporated into the protein using amber stop codon suppression. L-Anap is naturally fluorescent when excited at 360 nm and acts as the FRET donor (Figure 3.1 B). The use of L-Anap as the FRET donor is advantageous over traditional FRET methods as L-Anap is small (roughly the size of tryptophan) and does not require the use of a flexible linker that can limit the accuracy and sensitivity. Fluorescent signal from L-Anap is quenched by the FRET acceptor, Cu^{2+}, in a distance dependent manner.

Cu^{2+} is localized to the chosen location through 1-(2-pyridin-2-yldisulfanyl)ethyl)-1,4,7,10-tetraazacyclododecane (TETAC) which binds metal ions with high affinity and forms a disulfide bond with cysteine resides. The degree of L-Anap quenching by Cu^{2+} can be used to quantify the distance between the FRET pair within a range of about 20Å. By incorporating the FRET pair into mitofusin near Hinge 1, we can use this technique to evaluate conformational changes in response to nucleotide binding and hydrolysis to investigate how conformational changes are involved in the mechanism of mitochondrial fusion. Here, I develop method using ACCuRET with purified mitochondria in order to assess conformational changes in full-length mitofusin protein using isolated mitochondria.

3.2 Results

3.2.1 Choosing the FRET donor and acceptor

In order to measure conformational changes in full length protein, we chose to express mitofusin in mammalian cells. This allows mitofusin to insert into the mitochondrial outer membrane which allows mitofusin to exist in its native context. Mitochondria will be isolated for analysis in order to concentrate mitofusin to enhance signal from the naturally fluorescing Anap. I chose to express mitofusin in Flp-In TREx HEK293 cells, so I could temporally control expression of mitofusin with induction by tetracycline (TET). This system is also advantageous because there is less cell-to-cell variability in expression level compared to retroviral transduction techniques. To adopt ACCuRET for mitofusin, I focused on conformational changes around Hinge 2 in which mitofusin can adopt at least two known conformations in response to the nucleotide state. First, I chose candidate locations for the ACCuRET donor and acceptor, one of which will be placed on the GTPase domain and the other on HB1. Insertion of L-Anap at the amber stop codon (TAG site) is not viable for all locations, requiring us to test several possible TAG sites for optimal expression. Features we considered when choosing a FRET pair include 1) whether each FRET pair was within the 20Å Cu^{2+} quenching window in both the open and closed conformation, 2) whether the residues were surface exposed and 3) we prioritized residues that were not conserved. We used UCSF Chimera to determine the distance between residues in the open and closed conformations as well as accessibility. Based on these characteristics, we chose four of the most viable candidate FRET pairs to proceed with optimization (Figure 3.1 C).

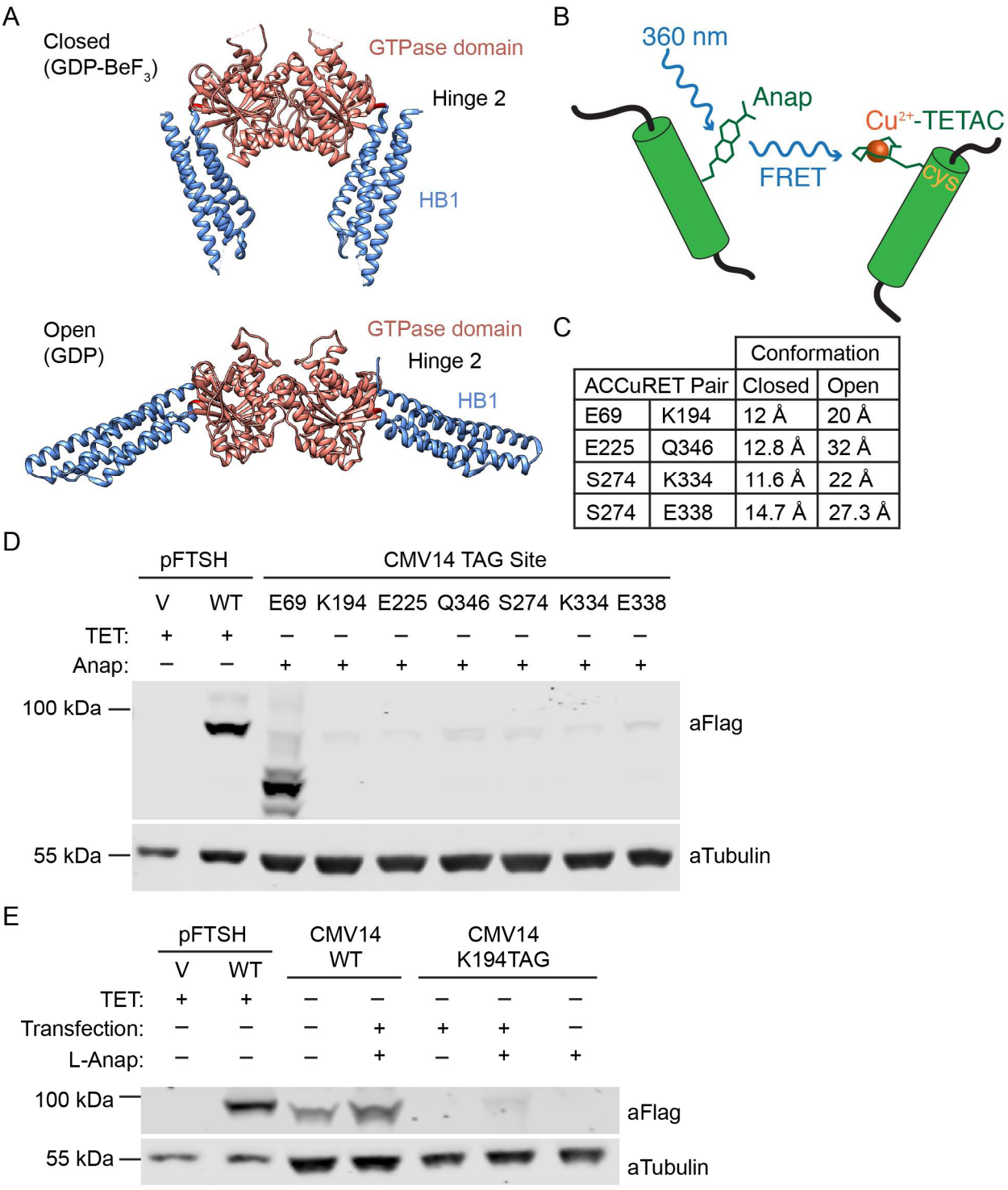

		Conformation	
ACCuRET Pair		Closed	Open
E69	K194	12 Å	20 Å
E225	Q346	12.8 Å	32 Å
S274	K334	11.6 Å	22 Å
S274	E338	14.7 Å	27.3 Å

Figure 3.1 Amber Stop Codon Site Optimization with Transient Transfection.

(A) Structure of Mfn1 in the open conformation bound to GDP-BeF_3 (PDB 5GOM) and in the closed conformation (PDB 5YEW). (B) Schematic of ACCuRET fluorescence energy transfer. L-Anap is excited at 360 nm and emits around 470 nm and quenched by copper ion (Cu^{2+})-TETAC. (C) Table of potential FRET pairs. Distance between each residue in the open conformation of Mfn1 (5GOM) or the closed conformation (5YEW) in angstroms (Å). (D) Western blot of whole-cell lysates transfected with Mfn1-Flag with amber stop codon inserted at indicated location and probed with α-Flag and α-tubulin. Cells were treated with (+) or without (-) "Anap", indicating the components necessary for insertion of L-Anap at the amber stop codon (transfection with pANAP and peRF1, then incubation with L-Anap-ME). Expression controls were collected from whole cell lysates of Flp-In TREx Hek293 cells with Mfn1-^{WT}-Flag stably inserted behind the TET-inducible promoter and treated with 0.2 µg/mL TET for 4 hrs. Molecular weight markers are

indicated on the left (kDa). (E) Western blot of whole cell lysates from Flp-In TREx HEK293 cells stably transfected with Mfn1-Flag behind the TET-inducible promoter (pFTSH) or transiently transfect with Mfn1-Flag (CMV14) and probed with α-Flag and α-tubulin. Cells were treated with (+) or without (-) 0.2 μg/mL TET for 4 hrs, co-transfected with (+) or without (-) CMV14-Mfn1, pAnap and peRF1 (Transfection), and with (+) or without (-) L-Anap-ME. Molecular weight markers are indicated on the left (kDa).

In order to determine the TAG site with highest incorporation of L-Anap, I created mitofusin constructs in the CMV14 plasmid with TAG sites inserted at each candidate location (Figure 3.1 C). To insert L-Anap into the TAG site, mitofusin is co-transfected with pANAP, a plasmid encoding the tRNA and tRNA synthetase for L-Anap, which delivers L-Anap to the ribosome during protein synthesis, and peRF1, a dominant negative form of eukaryotic release factor 1 (DN-eRF1), which aids in the incorporation of noncanonical amino acids into proteins. After transfection for 4-8 hrs, the media is replaced with 20 μM L-Anap methyl ester (L-Anap-ME) to allow expression of mitofusin to proceed in the presence of the components required to incorporate L-Anap into the TAG site. In order to determine which sites allow mitofusin to express with the greatest efficiency, I transiently expressed these mitofusin variants in TREx HEK293 Host cells then collected whole cell extracts for Western blot analysis. For this first experiment, I used TREx cells stably expressing $Mfn1^{WT}$-Flag behind a TET-inducible promotor as a control for Mfn1 expression at the correct molecular weight. $Mfn1^{E69ANAP}$ had intense bands on Western blot, but there were additional bands present at lower molecular weights, indicating ribosome readthrough of the TAG site during transcription (Figure 3.1 D). Mitofusin with other TAG sites had relatively little protein present, indicating L-Anap was incorporated with low efficiency, but only bands at the expected size were detected. Based on these results, all but E69 were determined to be viable options for the TAG site.

To reinforce this conclusion, I repeated the experiment with additional positive and negative controls. First, I included transient expression of $Mfn1^{WT}$-Flag from the CMV14 plasmid in order to compare expression levels. As $Mfn1^{WT}$-Flag CMV14 does not have a TAG site, this represents the maximum anticipated expression. As expected, transient expression of $Mfn1^{WT}$ was lower than mitofusin stably integrated into the genome and induced by TET (Figure 3.1 F). As expected, expression of $Mfn1^{K195ANAP}$ was lower than $Mfn1^{WT}$ because of the low efficiency of L-Anap incorporation. As a negative control, I compared expression in cells treated with L-Anap, but without transfection of pAnap, peRF1 or CMV14-Mfn1. No band was detected at ~100 kDa when cells were treated with L-Anap only, indicating that the band we see with all components present is not due to off target L-Anap incorporation (Figure 3.1 F). I also

compared cells transfected with all plasmids in the absence of L-Anap. No band was detected under this condition, indicating the detected band was not a result of ribosome readthrough of the TAG stop codon (Figure 3.1 F).

3.2.2 Expression of Mfn1 in Flp-In TREx HEK 293 cells

Due to the increased expression of $Mfn1^{WT}$ in the TET inducible cells compared to transient transfection, we moved to stable insertion of mitofusin behind the TET inducible promotor. I expected that this would increase efficiency of the incorporation of L-Anap because it is a two-part transfection (pANAP and peRF1) instead of a three-part transfection (Mfn1-Flag CMV14, pANAP and peRF1). Because it takes 5-6 weeks to create cell lines with mitofusin stably inserted behind the TET inducible promotor and because our initial experiment showed that TAG site allowed mitofusin to be expressed at similar levels, I chose one FRET pair as a starting point to test the system in the TREx cells. I chose K334 for the donor and S274 for acceptor because they were both determined to be viable TAG sites (Figure 3.1 D) and the distance between the pair is closest to the 20Å range of reliable metal ion quenching in both the closed and open conformations, which may allow us to quantify the distance between the FRET pair (Figure 3.1 C). In order to express mitofusin in this system, cells are transfected with pANAP and peRF1 for 4-8 hrs, then the media is replaced with media containing 20 μM L-Anap-ME and 0.1 μg/mL TET for ~20 hrs. I verified expression of mitofusin in this system using Western blot to compare expression levels of cells treated with or without the conditions required for expression (Figure 3.2 A).

3.2.3 Detection of L-Anap fluorescent signal

Next, I determined if I could detect fluorescent signal from L-Anap from isolated mitochondria in the plate reader assay. After transfection with pANAP and peRF1 and expression induced with TET in the presence of L-ANAP-ME, mitochondria were isolated and placed at varying concentrations in a black bottomed 384 well plate. Untreated mitochondria were also collected to detect background fluorescence. Mfn1-ANAP was excited at 360 nm and emission spectra were recorded from 400-600 nm in samples with 20 μL of mitochondria at increasing concentration (0 μg/μL, 0.25 μg/μL, 0.5 μg/μL, 1 μg/μL, 1.5 μg/μL, and 2 μg/μL). I saw an increase in fluorescence correlated with increased mitochondrial concentration (Figure 3.2 B). However, background fluorescence also increased with increased mitochondrial protein

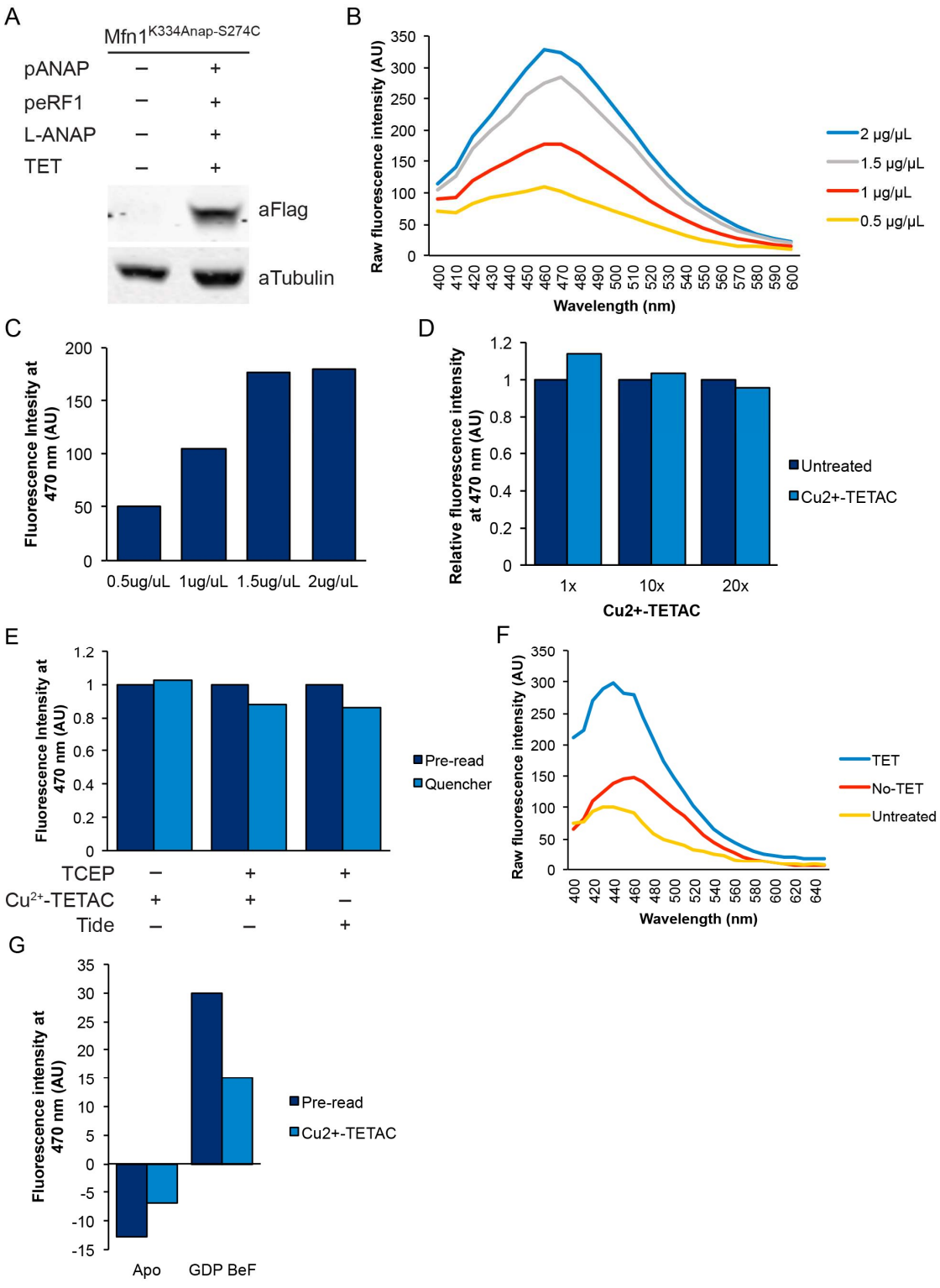

Figure 3.2 Anap fluorescence detection and optimization.

A) Western blot of whole-cell lysates from Flp-In TREx HEK293 cells with Mfn1$^{K334ANAP-S274C}$-Flag stably inserted into the genome behind a TET inducible promoter. Cells were transfected with (+) or without (-) the components necessary for insertion of L-Anap into the amber stop codon site. Whole-cell lysates were run on SDS-PAGE and immunoblotted with α-Flag and α-tubulin. (B) Emission spectra from mitochondria expressing Mfn1$^{K334ANAP-S274C}$ -Flag plated at indicated protein concentration and excited at 360 nm. (C) Fluorescence intensity at 470 nm with background fluorescence from untreated mitochondria removed from data presented

in B. (D) Fluorescence intensity at 470 nm from mitochondria expressing Mfn1$^{K334ANAP-S274C}$ -Flag excited at 360 nm. Indicated values represent fluorescence intensity with background fluorescence from untreated mitochondria removed. (E) Fluorescence intensity at 470 nm from mitochondria expressing Mfn1$^{K334ANAP-S274C}$ -Flag excited at 360 nm. Indicated values represent fluorescence intensity with background fluorescence from untreated mitochondria removed. (F) Emission spectra from mitochondria treated with indicated conditions and excited at 360 nm. (G) Fluorescence intensity at 470 nm from mitochondria expressing Mfn1$^{K334ANAP-S274C}$ -Flag excited at 360 nm. Indicated values represent fluorescence intensity with background fluorescence removed. Background was defined as intensity at 470 nm from mitochondria transfected with pAnap and peRF1 and treated with L-Anap in the absence of TET. All graphs represent n=1. AU=arbitrary units.

concentration. When the fluorescence is corrected by removing background by untreated mitochondria, we detect peak fluorescence intensity around 470 nm (Figure 3.2 C). Because fluorescent signal correlated with mitochondrial concentration, I continued experiments using the highest concentration of mitochondria that I felt I could reliably extract in a single mitochondrial isolation prep.

3.2.4 Cu^{2+}-TETAC quenching

Once I established a working concentration of mitochondria, I set out to determine if Cu^{2+}-TETAC would quench Mfn1-Anap fluorescence in our system. Mitochondria were isolated in the presence or absence of the Anap expression conditions, incubated with or without Cu^{2+}-TETAC, and the emission spectra after excitation at 350 nm was measured. Initial readings showed that Cu^{2+}-TETAC did not quench the signal from L-Anap (Figure 3.2 D). To test if a higher concentration of Cu^{2+}-TETAC was required, I re-measured fluorescence after adding 10x and 20x Cu^{2+}-TETAC. Even with 20x Cu^{2+}-TETAC, I did not detect significant quenching (Figure 3.2 D). Because fluorescence detected from L-Anap with or without 1x Cu^{2+}-TETAC is inconsistent with interpretable results, I decided to alter the protocol to measure the same well before and after adding Cu^{2+}-TETAC in order to compensate for well-to-well variability.

A possible explanation for the lack of quenching with Cu^{2+}-TETAC is that it cannot bind to cysteine because it has been oxidized in the process of isolation of mitochondria from cells. To test this, I included the reducing agent tris(2-carboxyethyl)phosphine (TCEP) in the mitochondrial isolation buffer. Specifically, TCEP was added to mitochondria 10 min prior to measuring fluorescence intensity at 470 nm after excitation at 360 nm. Then, Cu^{2+}-TETAC was added and fluorescence intensity was recorded after 3 min. As previously observed, without TCEP, Cu^{2+}-TETAC did not quench fluorescent signal at 470nm (Figure 3.3 E). However, in the presence of TCEP, Cu^{2+}-TETAC quenched signal by 12%, suggesting that the cysteine residue had been oxidized. Detectable quenching was encouraging, but the degree of quenching was still relatively small, so we pursued an explanation for the mild quenching phenotype. In the open

conformation, K334 and S274 are 22Å apart, which is at the edge of the maximum quenching range for Cu^{2+}. A potential explanation for the low quenching we detected is that rotomers of L-Anap or TETAC positioned the Cu^{2+} too far away from ANAP to quench. To test this, I used a more potent quencher, Tide quencher. I observed that Tide quenched ANAP fluorescence to a similar degree as Cu^{2+}-TETAC, suggesting that Cu^{2+} is positioned within range of L-Anap (Figure 3.2 E).

After discussion with the authors of the original ACCuRET methods paper, I made adjustments to the negative control used to determine background fluorescence. Previously, I used untreated isolated mitochondria to determine background fluorescence. Here, I transfected cells with pANAP and peRF1 to express the tRNA components, then media was replaced with L-Anap-ME in the absence of TET (no-TET control). Without TET, mRNA for $Mfn1^{K334ANAP-S274C}$ is not translated, so L-Anap will not be incorporated into $Mfn1^{K334ANAP-S274C}$. Thus, any fluorescence introduced by L-Anap in the no-TET control therefore represents either incorporation of L-Anap into other proteins containing naturally occurring TAG sites or free L-Anap that has entered the mitochondrial matrix. I tested the new negative control for background in the assay. Background fluorescence for the no-TET control is slightly higher than that of untreated mitochondria alone (Figure 3.2 F). Addition of TET drastically increased the fluorescence detected after excitation at 360 nm, indicating successful incorporation of L-Anap into $Mfn1^{K334ANAP-S274C}$ (Figure 3.2 F).

3.2.5 Changes to experimental conditions

At this stage of assay development, I further re-evaluated the conditions under which the experiment will be conducted to guide the development of the assay. The following adjustments were made to the protocol. First, after isolating mitochondria and adjusting for protein concentration, I transferred mitochondria from the isolation buffer into cytosol buffer, which more closely mimics the intracellular environment. Cytosol buffer includes an energy regenerating system, which helps maintain membrane potential of the mitochondria. Stable membrane potential is required for mitofusin activity and therefore may influence mitofusins ability to undergo conformational changes (Legros et al., 2002). With the switch into cytosol buffer, I will be able to compare mitochondria treated with different nucleotide states, either in the apo state or treated with GDP-BeF_3. We determined this was important to include in our assay development as we expect to see differential quenching in the presence or absence of GDP-BeF_3. If we do not detect

different degrees of quenching with GDP-BeF_3, then we would conclude that our assay needs further optimization. Second, I eliminated a nearby cysteine residue in the mitofusin constructs (C327S) in order to prevent potential background quenching from Cu^{2+}-TETAC binding to an off-target cysteine residue. Third, I attempted to reduce background from non-specific L-Anap binding by increasing the number of washes in mitochondrial isolation buffer (MIB) during mitochondrial isolation. With these changes to the protocol, I felt more confident that we were proceeding with assay development under the desired experimental conditions. However, in the first pilot under the modified assay conditions, background fluorescence was high relative to fluorescence emitted at 470 nm by L-Anap excited at 360 nm (Figure 3.2 F). Thus, when background fluorescence from the no-TET control was subtracted, the results were not interpretable (Figure 3.2 G). We determined that the signal to noise ratio needs to be optimized. In order to fix this ratio, we either need to increase the fluorescence detected from L-Anap incorporated into $Mfn1^{K334ANAP-S274C}$ or decrease the background fluorescence.

3.2.6 Optimization of expression conditions

First, I attempted to increase detectable signal over background by increasing the concentration of fluorescent $Mfn1^{K334ANAP-S274C}$ on the mitochondria through optimization of the transfection conditions. The original ACCuRET protocol was optimized for a three-part transfection and recommends transfecting pANAP and peRF1 at a ratio of 3:4. First, I adjusted the amount of peRF1 while keeping the total amount of pANAP the same. Our results indicate that adjusting the pANAP:peRF1 ratio from 3:4 to either 3:3 or 3:2 did not enhance expression of mitofusin (Figure 3.3 A & B). I also evaluated total DNA transfected. I found that transfection of 2x pAnap and peRF1 resulted in increased protein expression, however 3x DNA in the transfection did not further increase expression (Figure 3.3 A & B). As these were the conditions I had been using to express $Mfn1^{K334ANAP-S274C}$ in the TREx cells, I did not change the protocol based on these results.

Next, I tested whether increasing expression time in the presence of TET and Anap-ME could increase the total protein expressed. I expect that increasing the time cells have to express protein will increase the total amount of protein transcribed, which would allow more $Mfn1^{K334ANAP-S274C}$ on the mitochondria to be detected in our assay. First, I optimized for expression by increasing the time cells are incubated in the

presence of L-Anap and TET after transfection. However, in order to collect mitochondria

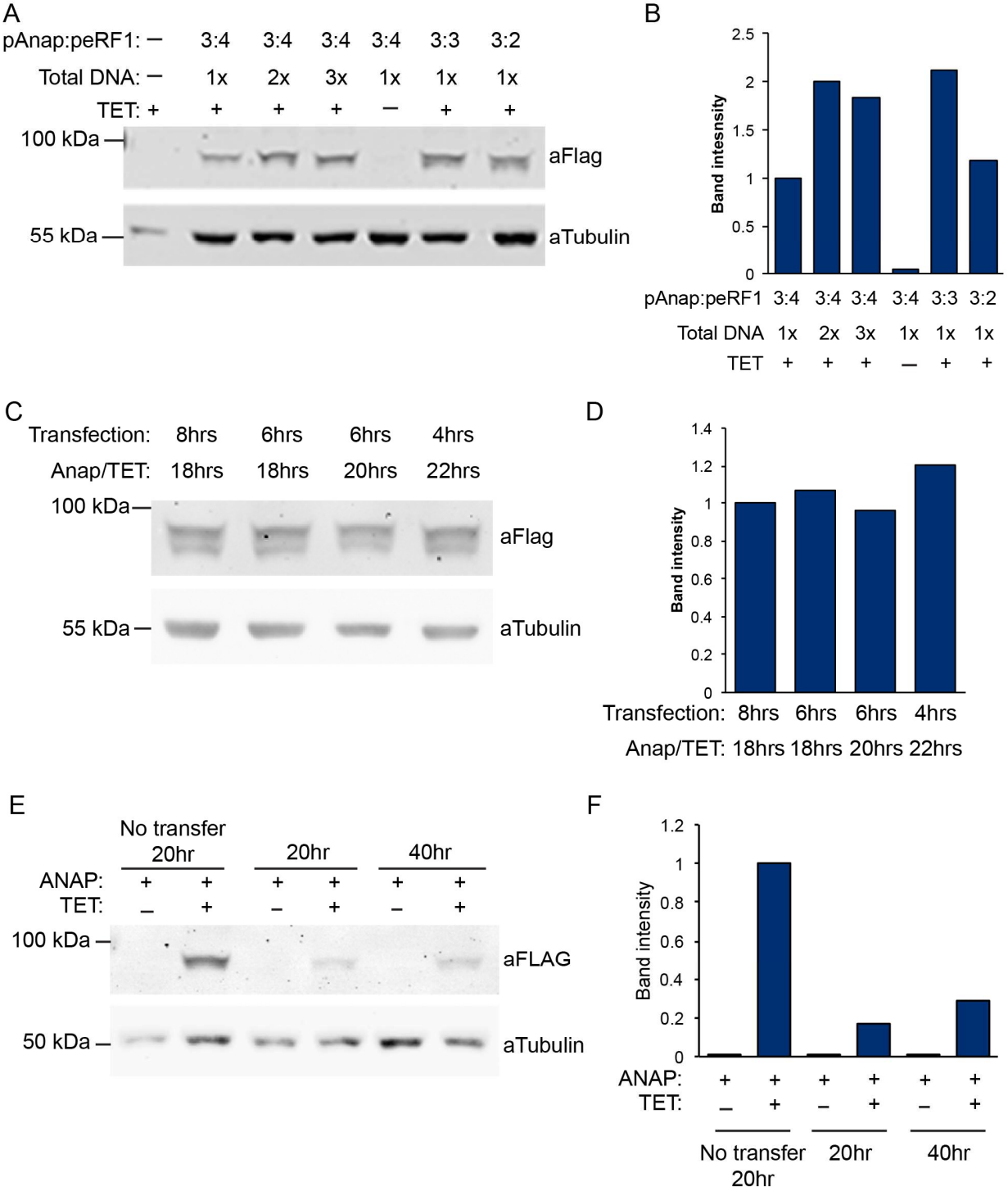

Figure 3.3 Expression Optimization.

(A) Western blot of whole-cell lysates from Flp-In TREx HEK293 cells with Mfn1$^{K334ANAP-S274C}$ -Flag stably inserted behind the TET-inducible promoter and expressed under the indicated expression conditions. Whole-cell lysates were run on SDS-PAGE and immunoblotted with α-Flag and α-tubulin. Molecular weight markers are indicated on the left (kDa). (B) Quantification of band intensities from western blot described in A. Band intensities represent α-Flag normalized to α-tubulin loading control. (C) Western blot of whole-cell lysates from Flp-In TREx HEK293 cells with Mfn1$^{K334ANAP-S274C}$ -Flag stably inserted behind the TET-inducible promoter and expressed under the indicated expression conditions. Whole-cell lysates were run on SDS-PAGE and immunoblotted

with α-Flag and α-tubulin. Molecular weight markers are indicated on the left (kDa). (D) Quantification of band intensities from western blot described in C. Band intensities represent α-Flag normalized to α-tubulin loading control. (E) Western blot of whole-cell lysates from Flp-In TREx HEK293 cells with Mfn1$^{K334ANAP-S274C}$ -Flag stably inserted behind the TET-inducible promoter and expressed under the indicated expression conditions. Whole-cell lysates were run on SDS-PAGE and immunoblotted with α-Flag and α-tubulin. Molecular weight markers are indicated on the left (kDa). (F) Quantification of band intensities from western blot described in E. Band intensities represent α-Flag normalized to α-tubulin loading control.

for experimentation one day after transfection, the total transfection and incubation time cannot exceed ~26 hrs. Thus, to increase the time cells are incubated in L-Anap and TET, we must decrease the amount of time the transfection reagents are on the cells. Here, we see that when I dropped the transfection time from 8 hrs to 4 hrs in order to increases expression in the presence of L-Anap and TET from 18hrs to 22 hrs there was a slight increase in expression (Figure 3.3 C & D). We considered that there might also be more Mfn1 $^{K334ANAP-S274C}$ protein if we incubated cells in the presence of L-Anap and TET for 2 days prior to collecting mitochondria. This also required an adjustment to the transfection conditions to avoid transfecting cells at low confluency, which is stressful and can cause cell death. Thus, I transfected cells in a 12 or 24-well dish at ~80% confluency and transferred the cells to a larger 6-well dish 4 hours after transfection. These cells were allowed to incubate in media containing L-Anap-ME and TET for 20 or 40 hours, respectively. To control for whether transferring the cells between dishes after transfection affects expression, I transfected cells in a 6-well dish at ~80% confluency for 4 hrs and incubated in L-Anap-ME and TET for 20hrs, without transferring cells to a new dish. We found that the act of transferring cells after transfection significantly reduced expression efficiency (Figure 3.3 C). Additionally, expression for 40hrs was not significantly improved from cells expressing for 20hrs in the transferred cells (Figure 3.3 C). Taken together, our data shows that the most efficient transfection conditions is 0.6ug:0.8ug DNA pANAP:peRF1 for 4hrs and expression with L-ANAP-ME and TET for 22 hours, without moving cells to a new dish.

3.2.7 Reduce background fluorescence with L-Anap-TFA

Next, I sought to decrease background signal, which required that we determined the source of the background fluorescence. Signal from mitochondria not expressing Mfn1$^{K334ANAP-S274C}$ could be coming from free L-Anap that is stuck in or on the mitochondria or L-Anap could be incorporated into naturally occurring amber stop codons in other mitochondrial proteins. To determine if free L-Anap-ME is trapped in the mitochondria, I isolated un-transfected mitochondria that were incubated with or without L-Anap-ME. In this scenario, any fluorescence signal detected is due to nonspecific binding of L-Anap to

mitochondria as no

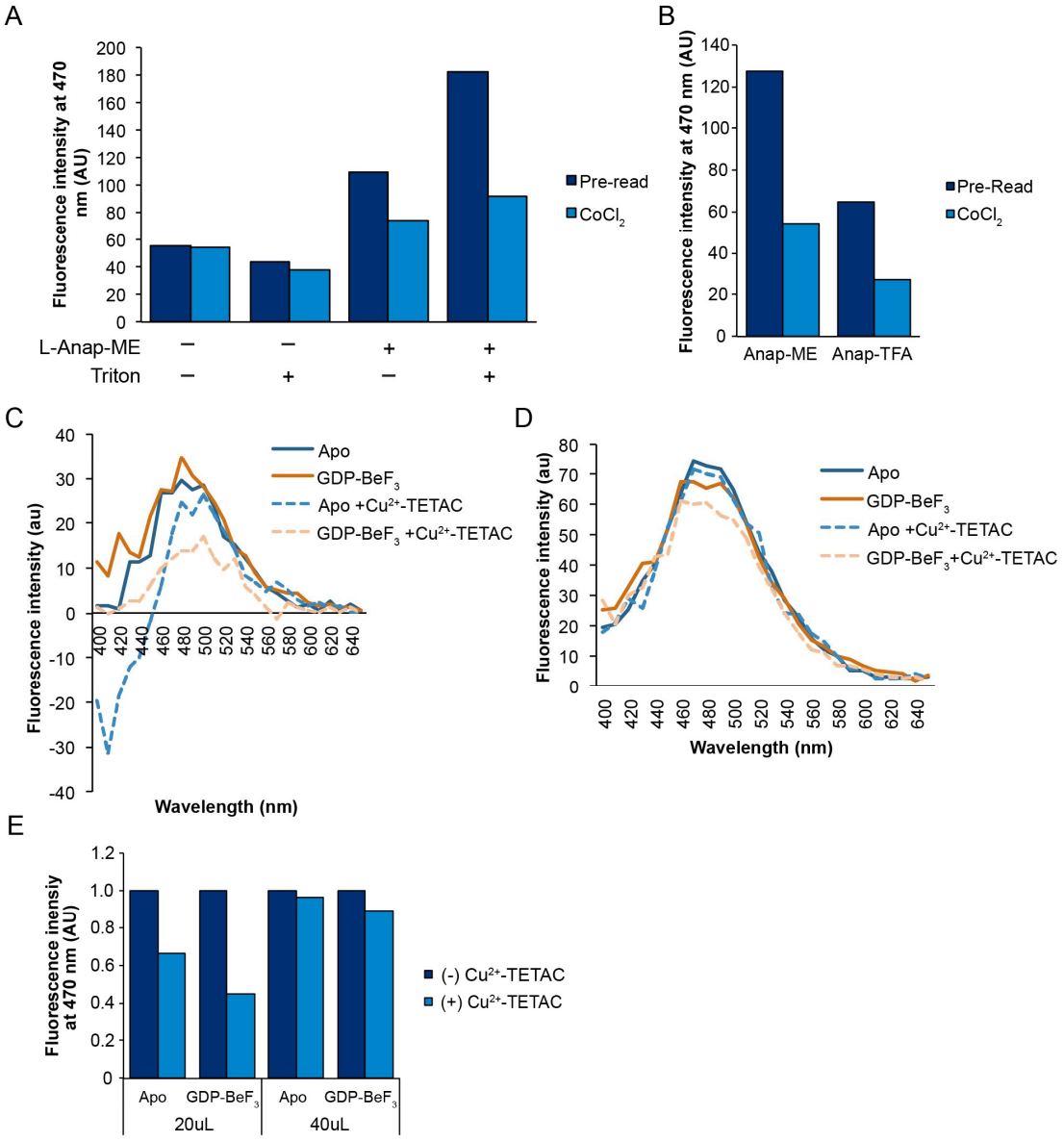

Figure 3.4 Background Optimization.

A) Fluorescence intensity at 470 nm from mitochondria expressing Mfn1$^{K334ANAP-S274C}$ -Flag excited at 360 nm. Indicated values represent fluorescence intensity with no-TET control background fluorescence removed. (B) Fluorescence intensity at 470 nm from mitochondria expressing Mfn1$^{K334ANAP-S274C}$ -Flag excited at 360 nm. Indicated values represent fluorescence intensity with no-TET control background fluorescence removed. (C) Emission spectra from mitochondria expressing Mfn1$^{K334ANAP-S274C}$ -Flag excited at 360 nm with background fluorescence from no-TET control removed. (D) Emission spectra from mitochondria expressing Mfn1$^{K334ANAP-S274C}$ -Flag excited at 360 nm with background fluorescence from no-TET control removed. (E) Relative fluorescence intensity at 470nm from experiment described in C and D. All graphs represent n=1. AU=arbitrary units.

tRNAs are present to incorporate L-Anap into proteins with amber stop codons. I lysed mitochondria in the presence of Triton X-100 in order to release potentially trapped L-Anap-ME into solution and quenched using the potent cytosolic quencher, $CoCl_2$. We detected a 2-fold higher signal from mitochondria

incubated with L-Anap than without, suggesting that free Anap is trapped in or sticking to the mitochondria (Figure 3.4

A). $CoCl_2$ quenched the fluorescent signal at 470 nm, but only in mitochondria incubated with L-Anap, further showing that free Anap-ME is contributing to the background signal. This is separate from background signal from mitochondria alone, which is not quenched by $CoCl_2$. Quenching L-ANAP-ME from $CoCl_2$ was more efficient in mitochondria lysed with triton, suggesting that the bulk of background is coming from L-Anap trapped in the mitochondrial matrix as opposed to L-Anap sticking to the outer mitochondrial membrane.

Next, we considered the possibility that L-Anap-TFA may have a lower propensity to get stuck inside of the mitochondria compared to L-Anap-ME. To test this, I isolated mitochondria from cells incubated with no Anap, Anap-ME, or Anap-TFA and lysed with Triton X-100. The total fluorescence from mitochondria expressing Anap-TFA was lower than Anap-ME, suggesting less Anap was present in isolated mitochondria when cells were grown with ANAP-TFA (Figure 3.4 B). In both cases, CoCl2 was able to quench the signal from L-Anap.

3.2.8 Cu^{2+}-TETAC quenching in the presence of nucleotide

Next, I investigated whether our optimization results in more reliable expression and quenching of L-Anap emission at 470 nm. Previously, I had tested the concentration of mitochondria in a 20uL reaction and found that more concentrated mitochondria did not increase the detectable fluorescent signal. With more practice with isolating mitochondria, I was able to increase the reliable yield from a single prep, allowing me to explore using more mitochondria per experiment. Here, I wanted to know if increasing the volume of mitochondria at the same concentration, thereby doubling the total protein in the well, could increase the detectable fluorescent signal. The emission spectra for mitochondria excited at 360 nm had a much higher signal with 40uL than 20uL and had a more normal distribution when the background fluorescence from the no-TET control was subtracted (Figure 3.4 C & D). In both cases, we detected quenching after Cu^{2+}-TETAC, indicating that the optimized conditions that I developed provide the desired results. Additionally, I compared mitochondria treated with or without GDP-BeF_3. Mfn1 bound to GDP-BeF_3 is expected to adopt the closed conformation and Mfn1 in the apo state is expected to adopt the open

conformation. Therefore, Cu^{2+}-TETAC is expected to be in closer proximity to Anap in Mfn1 bound to GDP-BeF_3, resulting in increased quenching of the fluorescent signal. Indeed, we detected greater quenching with mitochondria incubated with GDP-BeF_3 than without (Figure 3.4 E). During this experiment, I accidentally doubled the Cu^{2+}-TETAC concentration in the 20uL wells, but not the 40uL wells. We saw a significant increase in quenching with the higher Cu^{2+}-TETAC concentration, suggesting that we could enhance quenching by adjusting the concentration of Cu^{2+}-TETAC (Figure 3.4 C E). This makes sense because we introduced TCEP in order to reduce the cysteine residue by cleaving disulfide bonds, which is how Cu^{2+}-TETAC binds to cysteine. Based on this result, I recommend moving forward with 40uL of 2ug/mL mitochondria per well and increasing the concentration of Cu^{2+}-TETAC.

3.3 Discussion

In conclusion, I made progress in the development of a new method to measure conformational changes in mitofusin using the newly described technique, ACCuRET. Using L-Anap-TFA, I detected fluorescent signal from L-Anap incorporated into Mfn1-Flag on isolated mitochondria and this signal was quenched by Cu^{2+}-TETAC. This indicates that we successfully expressed $Mfn1^{K334ANAP-S274C}$ with Anap incorporated at the TAG site, reduced background from free Anap trapped in the mitochondria, and Cu^{2+}-TETAC binds to cysteine in an orientation that allows quenching. I also detected stronger quenching in the presence of GDP-BeF_3, indicating that Mfn1 is adopting a different conformational state in response to nucleotide in our system. However, at this time, the data presented represent a single experiment. Therefore, the next step is to determine if the results are repeatable under the new conditions.

One question that I have not addressed is whether incorporation of ANAP at a different amino acid position in Mfn1 would be more efficient. Of note, this was highly variable in other systems. I believe that I have established the most efficient transfection conditions for expressing ACCuRET in the Flp-In TREx TET-inducible system using Anap incorporated at K334. If we are unable to repeat quenching under the proposed conditions, we may need to continue optimization of Mfn1 expression with incorporation of L-Anap. In order to do this, a methodical optimization of amber stop codon location may reveal an amber stop codon site that incorporates L-Anap more efficiently, thereby increasing overall expression of Mfn1. The most rigorous method to determine optimal amber stop codon sites would be to test expression of all six

TAG variants from the TET-inducible promotor. I have TREx cell lines with amber stop codons in two additional independent positions (S274TAG and E338TAG). Of note, the cell lines are mixed populations and it is possible to creating single cell isolates could allow us to optimize for isolates with higher expression.

Following selection of the TAG site with the highest protein expression level, optimization of quenching with Cu^{2+}-TETAC may be necessary. In Figure 3.4 F, I showed that increasing the concentration of Cu^{2+}-TETAC increased quenching. I propose that the presence of reducing agent, TCEP, may interfere with the binding of Cu^{2+}-TETAC to the cystine residue by cleaving disulfide bonds. A Cu^{2+}-TETAC dose curve may reveal a higher concentration of Cu^{2+}-TETAC that promotes maximum quenching. Although L-Anap-TFA reduced the background fluorescence compared to L-Anap-ME, I still detect high levels of background signal, indicating free Anap is still present in these mitochondrial preparations. To reduce this, I would attempt to dialyze Anap from the isolated mitochondria.

There are additional controls that could be done to verify that the system is working as expected. First, mitofusin assembles into higher order oligomers. It is possible that Cu^{2+}-TETAC bound to cysteine could quench Anap from nearby mitofusin protomers. To verify that we do not detect intramolecular quenching, two Mfn1 cDNAs would be expressed behind the same TET promoter. One Mfn1 would have the amber stop codon site for incorporation of L-Anap and the other Mfn1 would have the cysteine for Cu^{2+}-TETAC binding. With this system, we expect to detect fluorescent signal from L-Anap excited at 360 nm, but addition of Cu^{2+}-TETAC would fail to quench as it will be incorporated on separate Mfn1 molecules that are outside of the narrow quenching range. If no quenching is detected, we would conclude that quenching detected when Anap and Cu^{2+}-TETAC are incorporated into the same molecule is due to intermolecular quenching. Second, to establish that incorporation of the amber stop codon and cysteine do not affect mitofusin activity, we would perform a mitofusin rescue assay in mitofusin-null cells. Mouse embryonic fibroblasts lacking Mfn1 have a predominantly fragmented mitochondrial network. Expression of $Mfn1^{WT}$ in Mfn1-null cells rescues the reticular mitochondrial morphology (Engelhart and Hoppins, 2019). We expect that expression of Mfn1 with the ACCuRET pair in these cells would also rescue mitochondrial morphology, indicating that the protein is functional for mitochondrial fusion.

Once we have established a protocol, there are many applications for this system. First, we had identified that variants at Hinge 2 of Mfn1 led to formation of the *trans* complex between mitofusins on adjacent mitochondria that were unable to proceed with fusion, effectively trapping mitochondria in a tether (chapter 2). This led to the prediction that conformational changes around Hinge 2 are required for transitioning from the tether to full mitochondrial fusion. We can use ACCuRET to test this hypothesis by comparing $Mfn1^{WT}$ with the Hinge 2 variant, $Mfn1^{S329P}$. Second, we can use this system to assess how other disease-causing variants affect conformational changes in full-length mitofusin. Additionally, we can express Mfn2 with the corresponding ACCuRET pair to assess conformational changes in Mfn2 using this system. Establishing ACCuRET as a method to measure conformational changes in full-length mitofusin will be an invaluable tool to investigate the molecular mechanism of mitofusin-dependent mitochondrial fusion.

3.4 Materials and Methods

Cloning

To create constructs containing mitofusin variants, mitofusin was cloned into p3xFlag CMV14 (Sigma Aldrich; gift from Jodi Nunnari) or pFTSH (gift from Nancy Maizels) expression plasmids using Gibson assembly and variants were created using site-directed mutagenesis using Gibson assembly. Following digestion with DpnI to remove template DNA, the amplified DNA was transformed into DH5-alpha *Escherichia coli* cells and plasmids were purified from selected colonies. All plasmids were confirmed by sequence analysis.

Cell culture and transfection

All cells were grown at 37°C and 5% CO2 and cultured in DMEM (Thermo Fisher Scientific) containing 1X GlutaMAX (Thermo Fisher Scientific) with 10% fetal bovine serum (FBS; Seradigm). Flp-In TREx Host cells (Invitrogen) were a gift from Nancy Maizels. Flp-In TREx Host cells were maintained in media containing 15 µg/mL blasticidin (Life Technologies) and 100 µg/mL zeocin (Invitrogen). Cells were tested for mycoplasma contamination by 4′,6-diamidino-2-phenylindole staining.

Flp-In TREx HEK293 Host cells were co-transfected with 0.6 µg CMV14-Mfn1, 0.3 µg pANAP (Addgene #48696; gift from Sharona Gordon) and 0.4 µg peRF1-E55D.pcDNA5-FRT (gift from Sharona Gordon), 200 µL JetPRIME Buffer, and 4 µL JetPRIME Transfection Reagent (Polyplus Transfection) for 4-8hrs. Media was exchanged for media containing 20 µM L-Anap methylester (L-Anap-ME; AsisChem, Inc.) for 24 hrs.

Flp-In TREx Stable Lines

300,000 Flp-In TREx HEK293 Host cells (Thermo Fisher Scientific) were seeded in two wells of a 6-well dish per cell line. Two days later, cells were co-transfected with 0.2 µg pFTSH (gift from Nancy Maizels) containing gene of interest and 1.8 µg pOG44 (Life Technologies) using 4 µL JetPRIME Transfection Reagent (Polyplus Transfection) for 4-6hrs. Cells were pooled into 10-cm dishes and allowed to recover for 2 days before adding selection to the media (200 µg/ml hygromycin B).

SDS-PAGE, Western blot analysis, and quantification

Whole cell protein lysates were obtained by resuspending PBS-washed cells in radioimmunoprecipitation assay (RIPA) lysis buffer (150 mM NaCl, 1% Nonidet NP-40, 1% sodium deoxycholate, 0.1% SDS, 25 mM Tris [pH 7.4], and 1× Halt Protease Inhibitor Cocktail, EDTA-free [Thermo Fisher Scientific]). The samples were incubated on ice for 5 min and then spun at 21,000x*g* for 15 min at 4°C. The supernatant was transferred to a clean tube, and protein concentration was measured by bicinchoninic acid assay (Thermo Fisher Scientific). Following separation by SDS-PAGE, proteins transferred to nitrocellulose were detected using primary rabbit or mouse antibodies and visualized with appropriate secondary antibodies conjugated to IRDye (Thermo Fisher Scientific). The following antibodies were used in this study: mouse monoclonal anti-FLAG (Sigma; 1:1000) and mouse monoclonal anti-alpha tubulin (Thermo Fisher Scientific clone DM1A; 1:5000). Western blot images for expression of mitofusin from CMV14 plasmid were imaged on a LI-COR Imaging System (LI-COR Biosciences). Mitofusin band intensity was normalized to tubulin band intensity using LI-COR Analysis Software (LI-COR Biosciences). Western blot images from cells stably expressing mitofusin in Flp-In TREx HEK293 with pFTSH plasmid were acquired on Sapphire (Azure Biosystems) and quantification was performed with Azurespot (Azure Biosystems).

Preparation of mitochondria

For each experiment, one 15-cm plate of HEK293 Flp-In TREx cells were grown to ~90% confluency in 24mL DMEM with 10% FBS. One day before collection of mitochondria, cells were transfected with 4.8 µg pANAP, 6.4 µg DN-eRF1, 1.6 mL JetPRIME Buffer and 32 µL JetPRIME Transfection Reagent (Polyplus Transfection), for 4-8 hrs, unless otherwise indicated. Expression of mitofusin was induced by incubation with 20 µM L-Anap methylester (L-Anap-ME; AsisChem, Inc.) or 20 µM L-3-(6-acetylnaphthalen-2-ylamino)-2-aminopropionic acid trifluoroacetic salt (L-Anap-TFA; AsisChem, Inc.), and 0.1 µg/mL tetracycline hydrochloride (Fisher Scientific) for 16-22 hrs, as indicated. Cells were harvested by cell scraping, pelleted, and washed in mitochondrial isolation buffer (MIB) (0.2 M sucrose, 10 mM Tris-MOPS, pH 7.4, 1 mM ethylene glycol-bis(β-aminoethyl ether)-N,N,N′,N′-tetraacetic acid). The cell pellet was resuspended in one cell pellet volume of cold MIB with 1x HALT protease inhibitor cocktail (Thermo Scientific) and 0.5 mM phenylmethylsulfonyl fluoride (Sigma-Aldrich), and cells were homogenized by ~12 strokes on ice with a Kontes-Potter-Elvehjem tissue grinder set at 350 rpm. The homogenate was centrifuged (400 × g, 5 min, 4°C) to remove nuclei and unbroken cells, and homogenization of the pellet fraction was repeated followed by centrifugation at 400 × g, 5 min, 4°C. The supernatant fractions were combined and centrifuged (7400 × g, 8 min, 4°C) to pellet a crude mitochondrial fraction. The crude mitochondrial pellet was resuspended in a small volume of MIB. Protein concentration of mitochondria was determined by Bradford assay (Bio-Rad Laboratories).

Cells were left in MIB or pelleted and resuspended in Cytosol Buffer (20 mM PIPES-KOH [pH 6.8], 150 mM KOAc, 5 mM $Mg(OAc)_2$, 42 mM sorbitol, 2.25 mg/mL creatine phosphokinase, 40 mM creatine phosphate, 2.5 mM ATP, with or without 5 mM GDP, 50 mM NaF and 5 mM $BeSO_4$, and with or without 5 µM tris(2-carboxyethyl)phosphine (TCEP) as indicated). Mitochondria were incubated at 30°C for 10 min. Cu^{2+}-TETAC was made by mixing 1uL 110mM $CuSO_4$ in H2O and 1uL 100 mM 1-(2-pyridin-2-yldisulfanyl)ethyl)-1,4,7,10-tetraazacyclododecane (TETAC) in DMSO for 1 min, then 198uL Cytosol Buffer (20 mM PIPES-KOH [pH 6.8], 150 mM KOAc, 5 mM $Mg(OAc)_2$, 42 mM sorbitol) was added.

ACCuRET

Mitochondria were plated in a 384-well black plate at indicated volume and concentration. Mitochondria were excited at 360 nm and emission spectra recorded using SpectraMax Gemini XPS (Molecular Devices). Cu^{2+}-TETAC was subsequently added and mitochondria were excited at 360 nm and emission spectra recorded again. Background from the untreated or no-TET control was subtracted to determine fluorescence emitted from L-Anap.

Chapter 4. Conclusions and Future Directions

In this dissertation, I have used biochemical and molecular biology techniques to advance knowledge in the field of mitochondrial outer membrane fusion. I identified that GTP hydrolysis is required for mitofusin dependent tethering prior to mitochondrial fusion. I also made progress in the development of a technique to measure conformational changes in mitofusin.

4.1 Summary of findings regarding the model for mitofusin dependent mitochondrial fusion

I identified a variant in Mfn1 and Mfn2 that causes perinuclear clustering of mitochondria in mammalian cells. Analysis of this variant revealed that perturbations to Hinge 2 prevents fusion by trapping mitofusin in a tethered state. paGFP analysis revealed that mitochondria trapped in the perinuclear cluster are discrete entities and do not mix contents even in the presence of wild type mitofusin, indicating that this variant is dominant negative. I also showed that GTP hydrolysis is necessary for clustering, implicating GTP hydrolysis in formation of the tether. Additionally, the variant was unable to form higher order oligomers, suggesting conformational changes around Hinge 2 are required for assembly in *cis*. Taken together, our data suggests that mitofusin exists in a low energy *cis* dimer on mitochondria. When fusion is initiated, GTP hydrolysis activates mitofusin to form a trans assembly in a high energy state. Once the tether is formed, mitofusin undergoes conformational changes around Hinge 2 that allow the mitochondria to proceed to full fusion.

My research gives significant insight into the mechanism of mitofusin-dependent mitochondrial fusion. Previously, it was unknown how GTP hydrolysis of mitofusin contributed to the fusion mechanism. I identified that GTP hydrolysis is necessary for mitofusin interactions in *trans*. This is similar to the mechanism of atlastin in ER membrane fusion and differs from other known dynamin superfamily proteins (DSPs) involved in membrane division. This could indicate an important distinction between DSPs mediating membrane fusion and division. My research also sheds light on the models for CMT2A pathogenesis. Previous research on CMT2A disease-causing variants of Mfn2 revealed perinuclear clustering of mitochondria is a common theme. Research on select variants showed that mitochondria have reduced anterograde and retrograde movement in the axons on neurons, which was hypothesized to result in the clustering mitochondria phenotype. However, I showed that inhibiting the transport machinery

required for movement does not prevent perinuclear clustering induced by two of these disease variants, suggesting that perinuclear clustering of mitochondria and the defect in the transport are independent. How either of these phenotypes contributes to disease pathogenesis is a subject for future study.

4.2 Summary of method development using ACCuRET

As a member of the dynamin superfamily of proteins (DSPs), mitofusin is expected to coordinate GTP hydrolysis with assembly and conformational changes in order to drive membrane fusion. However, little is known about the conformational states adopted by mitofusin. Isolation of full-length mitofusin protein has yet to be achieved, limiting the techniques available to study the protein in vitro. Therefore, I worked on a technique to study full-length mitofusin on isolated mitochondria using the recently described FRET based method, ACCuRET (Gordon et al., 2018). I designed mitofusin with the FRET donor on HB1 and the FRET acceptor on the GTPase domain in order to measure conformational changes around Hinge 2.

To adapt the original ACCuRET protocol for isolated mitochondria I made several adjustments, including stable integration of the gene of interest behind a TET inducible promotor. Additionally, I discovered that the FRET donor, Anap-ME, was trapped in the mitochondria during isolation, which led to high background signal. I was able to reduce this background by changing from Anap-ME to Anap-TFA. Under the initial experimental conditions, I found that cysteine was oxidized during isolation, preventing Cu^{2+}-TETAC binding, and thereby preventing quenching of the signal from L-Anap. To address this, I added TCEP to reduce the disulfide bond, which allowed Cu^{2+}-TETAC to bind and quench the signal from Anap. With the optimized conditions for the ACCuRET experiment, I still detect a small degree of quenching by Cu^{2+}-TETAC. My results suggest increasing the Cu^{2+}-TETAC concentration could enhance quenching. Further, I proposed additional experiments in order to optimize fluorescence to ensure we obtain consistent results between experiments. Development of this technique will provide a valuable tool for analyzing the conformational states of full length mitofusin during mitochondrial fusion.

4.3 Future Directions

4.3.1 Effect of proline variant on conformational changes around Hinge 2

Mitofusin has been shown to adopt at least two conformational states based on the nucleotide binding state, but how these conformations fit into the bigger picture of mitofusin-dependent mitochondrial

fusion is still unknown. In chapter 2, I investigated a conserved serine residue at Mfn1^{S329} and Mfn2^{S350}, which is located at Hinge 2, between the GTPase domain the helical bundle 1. In the open conformation, S329/S350 is part of an intact α-helix and in the closed conformation, this residue forms the center of a 77-degree bend. When this residue is altered to proline, the function of mitofusin is greatly altered. To investigate how changes at this hinge affect conformational state, I propose using the ACCuRET technique described in chapter 3 to measure conformational changes in the presence of nucleotide in Mfn1^{S329P} and Mfn2^{S350P}. I predict the proline variant either locks mitofusin into a single conformation or destabilizes the alpha helix, leading to a floppy hinge. These results will help us understand how conformational changes around Hinge 2 contribute to mitochondrial fusion. If the proline variant locks mitofusin in one conformation, we will see that nucleotide state does not change quenching. If the degree of quenching matches Mfn1^{WT} in the GDP bound state, this would indicate that Mfn1^{S329P} is stuck in the open conformation. Whereas, if the degree of quenching matches Mfn1^{WT} bound to GDP-BeF_3, then we can make the prediction that Mfn1^{S329P} is stuck in the closed conformation. With this information, we can make the prediction that this conformation consists of the tether-competent state. Alternatively, we may see that fluorescence is quenched to an intermediate degree, indicating either that Hinge 2 is floppy or trapped in a state not previously observed by X-ray crystallography.

4.3.2 Conformational states of Mfn1 and Mfn2

Development of the ACCuRET technique will be instrumental in determining how conformational changes in mitofusin drive mitochondrial fusion. In addition to analyzing the proline variants described above, we can use ACCuRET to determine how perturbations in other regions of mitofusin affect conformation of the protein and how that affects mitochondrial fusion. It has been well studied that GTP hydrolysis is necessary for mitochondrial fusion. We can test if GTP hydrolysis changes the conformation around Hinge 2 by making mutations known to disrupt enzymatic activity in mitofusin, such as Mfn1^{K188A}/Mfn2^{K109A}, with the ACCuRET FRET pair.

ACCuRET should be adaptable to placement of FRET pairs in varying locations to measure both inter- and intra-molecular distances. Hinge 1 is predicted to undergo conformational changes during mitochondrial fusion and data from our lab showed that mutations near this hinge affect mitofusin function,

indicating movement about this hinge is functionally relevant (Samanas et al., 2020). If one half of the FRET pair is placed on HB1 and the other half of the FRET pair is placed on HB2, then we can measure how nucleotide state affects conformation around Hinge 1. Structure predictions based on the DSP most similar to mitofusin, BDLP, could be used to calculate expected distances between residues to design FRET pairs. ACCuRET could also be adapted to intra-molecular interactions. For example, placement of the amber stop codon site in the GTPase domain of one mitofusin and the cysteine residue on the GTPase domain of a separate mitofusin, we could measure changes in intramolecular contacts in response to changes in nucleotide state. Crystal structures of Mfn1 in the open or closed dimer could be used to design FRET pairs on the GTPase domain.

4.3.3 Mitofusin-dependent tether interface

Mitofusin has been shown to form higher order oligomers in the same membrane, in *cis*, as well as across mitochondrial membranes, in *trans*. However, it is still unknown which protein interfaces are necessary for forming each of these interactions. We can study the *trans* assembly interface by taking advantage of the tools developed in Chapter 2, using Mfn1^{S329P} and Mfn2^{S350P} to induce perinuclear clustering of mitochondria as a readout for tethering and the cytosolic variant of mitofusin, Mfn1^{F646D}, to interfere with this tether. In order to determine which interfaces are required for the *trans* interaction, mutations known to block interactions at specific interfaces could be introduced concurrently with the cytosolic variant. For example, E209A in Mfn1 is known to block interactions at the G-G interface. If the G-G interface is required for forming the trans interaction, then cytosolic expression of Mfn1$^{E209A-F646D}$ in cells expressing Mfn1^{S329P} on mitochondria will not prevent clustering of mitochondria, as Mfn1$^{E209A-F646D}$ won't be able to interact with Mfn1^{S329P}. However, if the G-G interface is not an important interface of the tether complex, expression of Mfn1$^{E209A-F646D}$ will interfere with clustering induced by Mfn1^{S329P}.

Further, we should be able to extend this technique to measuring tethering of Mfn2 using the corresponding variant, Mfn2^{F665D}. We will first test how Mfn2^{F665D} affects cytosolic expression of Mfn2 using fluorescence microscopy. Then, we can adapt the experiments performed with Mfn1^{F646D} to Mfn2^{F665D}. Our ability to induce and subsequently block tethering of mitofusin across mitochondrial membranes is a valuable tool for studying the *trans* interaction of mitofusin.

Chapter 5. Supplemental Figures

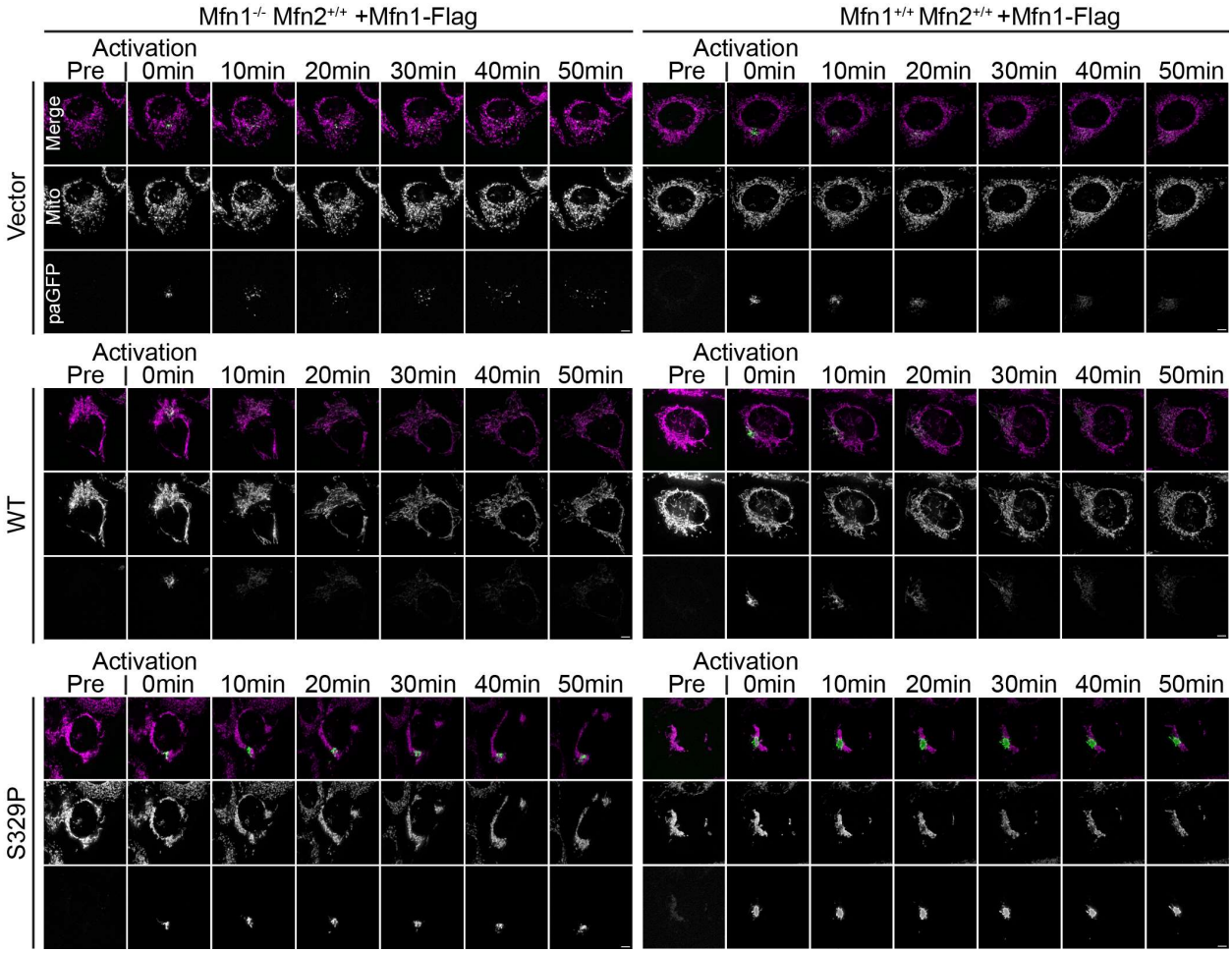

Figure 5.1 Representative images of mt-paGFP diffusion over 50 minutes

Mfn1-null or WT MEFs expressing mt-paGFP and transduced with empty vector (V), Mfn1^{WT}-Flag or Mfn1^{S329P}-Flag before activation of mt-paGFP (Pre) and 0min, 10 min, 20 min, 30 min, 40 min and 50 min following. Mitochondria were labeled with Mitotracker Red CMXRos and visualized with live cell fluorescence microscopy. Images represent maximum intensity projections. Scale bar = 5 μm.

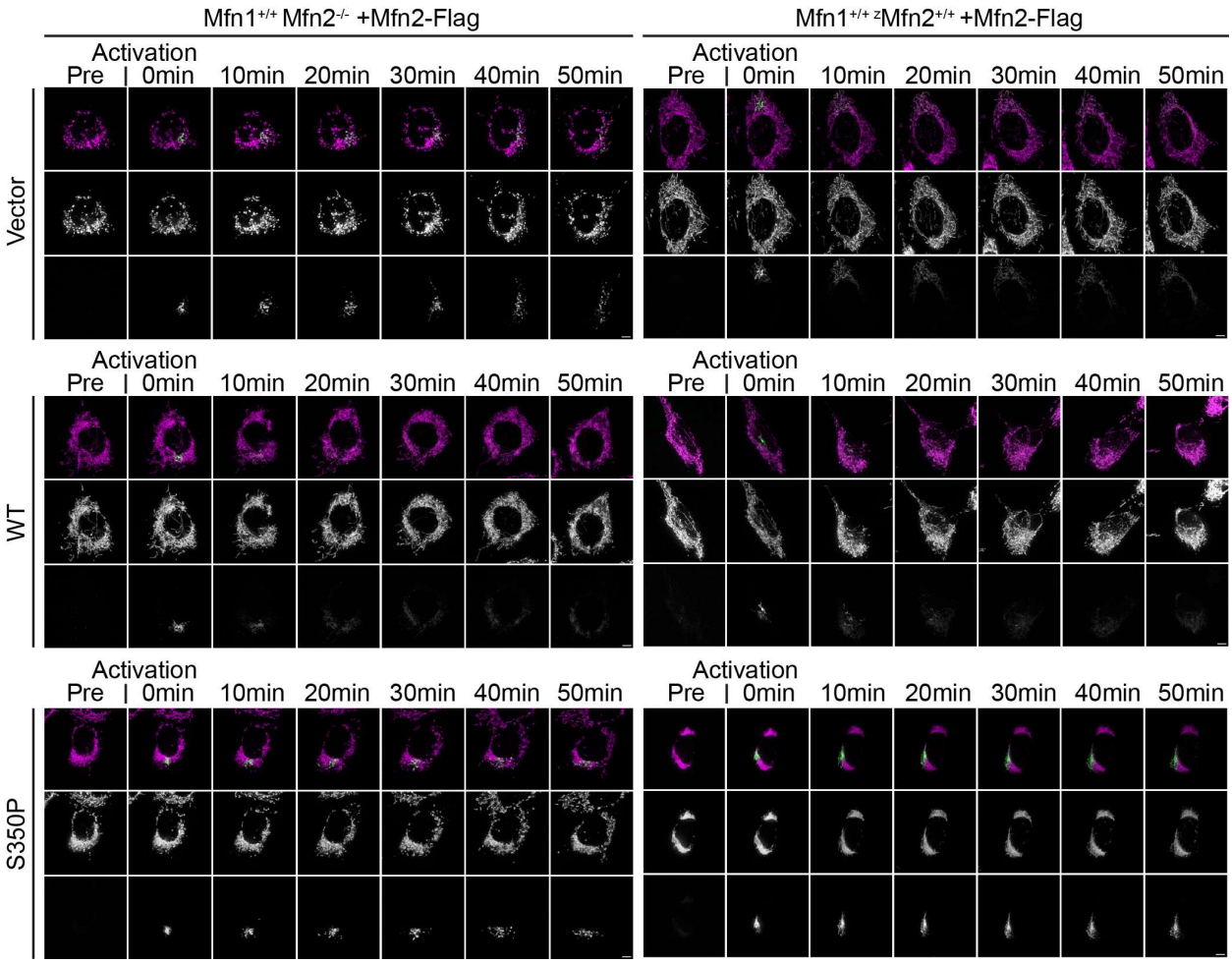

Figure 5.2 Representative images of mt-paGFP diffusion over 50 minutes

Representative images of Mfn2-null or WT MEFs expressing mt-paGFP and transduced with empty vector (V), $Mfn2^{WT}$-Flag or $Mfn2^{S350P}$-Flag before activation of mt-paGFP (Pre) and 0min, 10 min, 20 min, 30 min, 40 min and 50 min following. Mitochondria were labeled with Mitotracker Red CMXRos and visualized with live cell fluorescence microscopy. Images represent maximum intensity projections. Scale bar = 5 μm

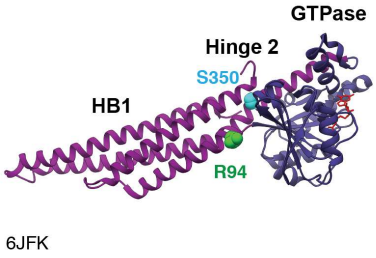

Figure 5.3 Structure of Mfn2

Ribbon structure of $Mfn2_{IM}$ bound to GDP (PDB: 6FJK) with the GTPase domain in dark blue, helical bundle 1 (HB1) in magenta, S350 highlighted in cyan, R94 highlighted in green, and GDP in red.

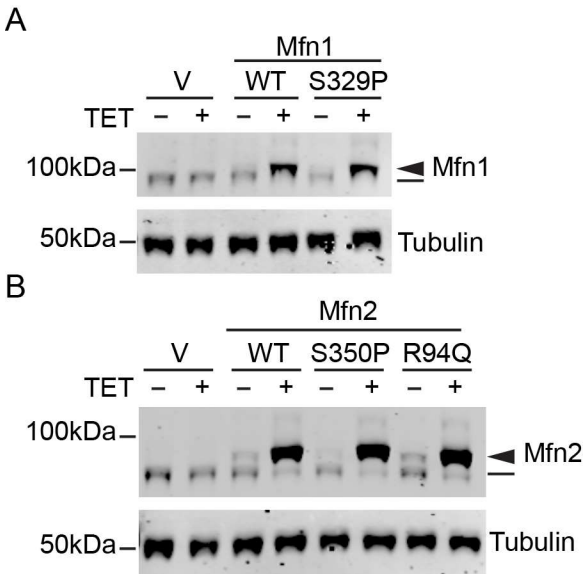

Figure 5.4 Mitofusin protein expression in Flp-In TREx HEK293 induced with 0.2 µg/mL TET for 4 hrs.

(A) Whole-cell lysates prepared from the indicated cell lines incubated in the absence (-) or presence (+) of 0.2 µg/mL TET for 4 hrs were subject to SDS–PAGE and immunoblotting with α-Mfn1 and α-tubulin. **(B)** Whole-cell lysates prepared from the indicated cell lines incubated in the absence (-) or presence (+) of 0.2 µg/mL TET for 4 hrs were subject to SDS–PAGE and immunoblotting with α-Mfn2 and α-tubulin.

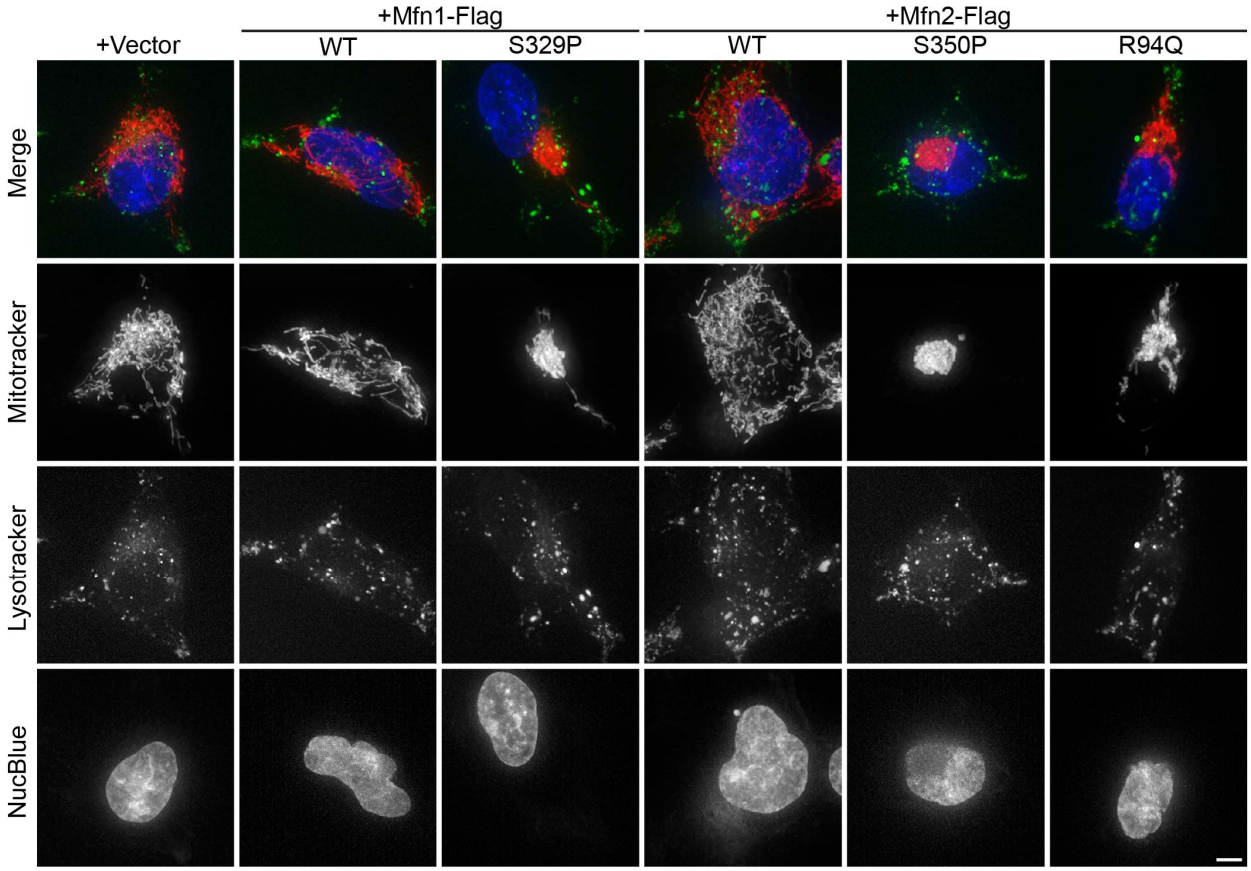

Figure 5.5 Mitofusin protein expression in Flp-In TREx HEK293 induced with 0.2 µg/mL TET for 4 hrs.

Representative images of Flp-In TREx HEK293 expressing indicated mitofusin variant following induction of expression by incubation with 0.2 µg/mL TET for 4 hrs. Mitochondria were labeled with Mitotracker Red CMXRos, lysosomes were labeled with Lysotracker, and nuclei were labeled with NucBlue and visualized by live cell fluorescence microscopy. Images represent maximum intensity projections. Scale bar = 5 µm.

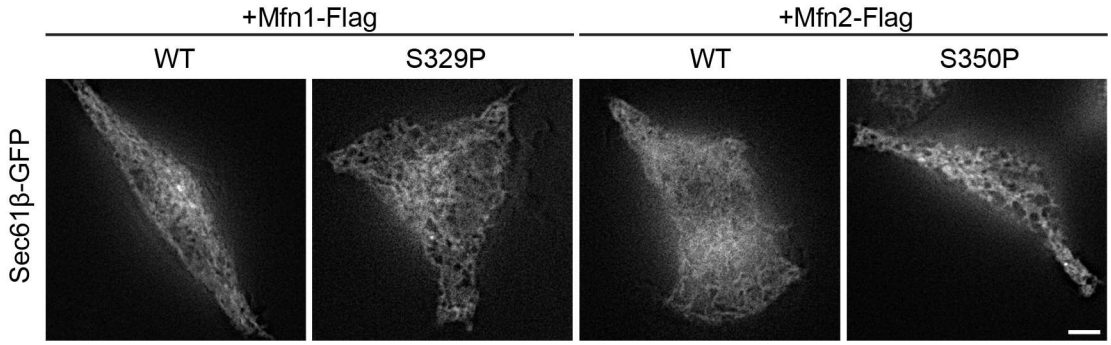

Figure 5.6 Endoplasmic reticulum distribution is not affected by expression of mitofusin proline variants

Representative images of Flp-In TREx HEK293 expressing indicated mitofusin variant following induction of expression by incubation with 0.2 µg/mL TET for 4 hrs. Endoplasmic reticulum was labeled by expression of Sec61-eGFP and visualized by live cell fluorescence microscopy. Images represent single z slices near the coverslip. Scale bar = 5 µm.

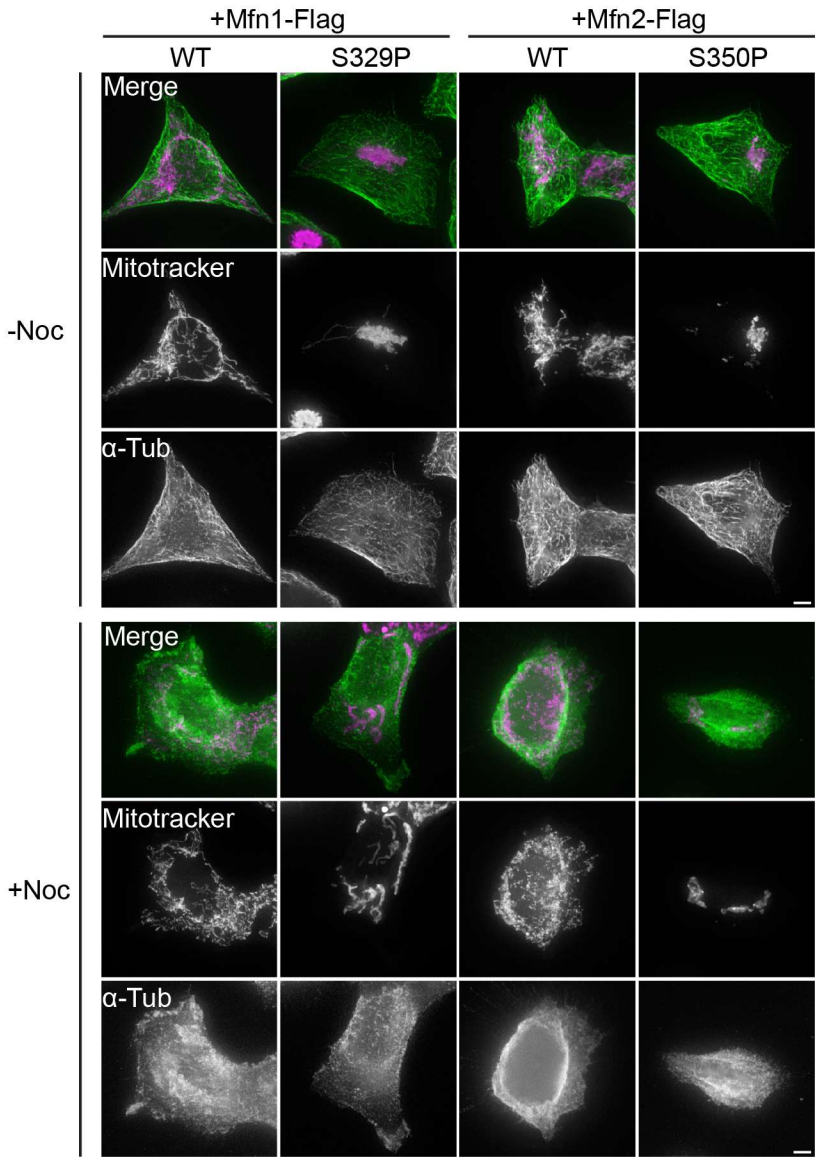

Figure 5.7 Microtubule depolymerization by nocodazole.

Representative images of Flp-In TREx HEK293 expressing indicated mitofusin variant following induction of expression by incubation with 0.2 µg/mL TET for 4 hrs in the presence of 0 nM or 5 nM nocodazole. Mitochondria were labeled with Mitotracker Red CMXRos. Cells were fixed and immunolabelled with anti-tubulin (α-Tub). Images represent maximum intensity projections. Scale bar = 5 µm.

Chapter 6. References

Agarwal, S., and S. Ganesh. 2020. Perinuclear mitochondrial clustering, increased ROS levels, and HIF1 are required for the activation of HSF1 by heat stress. *J Cell Sci.* 133:jcs245589.

Al-Mehdi, A. B., V. M. Pastukh, B. M. Swiger, D. J. Reed, M. R. Patel, G. C. Bardwell, V. V. Pastukh, M. F. Alexeyev, and M. N. Gillespie. 2012. Perinuclear mitochondrial clustering creates an oxidant-rich nuclear domain required for hypoxia-induced transcription. *Sci Signal.* 5:ra47.

Alexander, C., M. Votruba, U. E. Pesch, D. L. Thiselton, S. Mayer, A. Moore, M. Rodriguez, U. Kellner, B. Leo-Kottler, G. Auburger, S. S. Bhattacharya, and B. Wissinger. 2000. OPA1, encoding a dynamin-related GTPase, is mutated in autosomal dominant optic atrophy linked to chromosome 3q28. *Nat Genet.* 26:211-215.

Antonny, B., C. Burd, P. De Camilli, E. Chen, O. Daumke, K. Faelber, M. Ford, V. A. Frolov, A. Frost, J. E. Hinshaw, T. Kirchhausen, M. M. Kozlov, M. Lenz, H. H. Low, H. McMahon, C. Merrifield, T. D. Pollard, P. J. Robinson, A. Roux, and S. Schmid. 2016. Membrane fission by dynamin: what we know and what we need to know. *EMBO J.* 35:2270-2284.

Baloh, R. H., Schmidt, R. E., Pestronk, A., & Milbrandt, J. 2007. Altered Axonal Mitochondrial Transport in the Pathogenesis of Charcot-Marie-Tooth Disease from Mitofusin 2 Mutations. *Neurobiology of Disease*, *27*(2), 422–430.

Bido, S., F. N. Soria, R. Z. Fan, E. Bezard, and K. Tieu. 2017. Mitochondrial division inhibitor-1 is neuroprotective in the A53T-α-synuclein rat model of Parkinson's disease. *Sci Rep.* 7:7495.

Blass, J. P., Sheu, R. K.-F., & Gibson, G. E. 2000. Inherent Abnormalities in Energy Metabolism in Alzheimer Disease Interaction with Cerebrovascular Compromise. *Annals of the New York Academy of Sciences*, *903*(April), 204–221.

Brandt, T., L. Cavellini, W. Kühlbrandt, and M. M. Cohen. 2016. A mitofusin-dependent docking ring complex triggers mitochondrial fusion in vitro. *Elife.* 5:e14618.

Brandt, T., Cavellini, L., Kühlbrandt, W., & Cohen, M. M. 2016. A mitofusin-dependent docking ring complex triggers mitochondrial fusion in vitro. *ELife*, *5*, e14618.

Byrnes, L. J., A. Singh, K. Szeto, N. M. Benvin, J. P. O'Donnell, W. R. Zipfel, and H. Sondermann. 2013. Structural basis for conformational switching and GTP loading of the large G protein atlastin. *EMBO J.* 32:369-384.

Cao, Y. L., S. Meng, Y. Chen, J. X. Feng, D. D. Gu, B. Yu, Y. J. Li, J. Y. Yang, S. Liao, D. C. Chan, and S. Gao. 2017. MFN1 structures reveal nucleotide-triggered dimerization critical for mitochondrial fusion. *Nature.* 542:372-376.

Cartoni, R., E. Arnaud, J. J. Médard, O. Poirot, D. S. Courvoisier, R. Chrast, and J. C. Martinou. 2010. Expression of mitofusin 2(R94Q) in a transgenic mouse leads to Charcot-Marie-Tooth neuropathy type 2A. *Brain.* 133:1460-1469.

Cartoni, R., & Martinou, J. C. 2009. Role of mitofusin 2 mutations in the physiopathology of Charcot-Marie-Tooth disease type 2A. In *Experimental Neurology* (Vol. 218, Issue 2, pp. 268–273).

Chaanine, A. H., Joyce, L. D., Stulak, J. M., Maltais, S., Joyce, D. L., Dearani, J. A., Klaus, K., Nair, K. S., Hajjar, R. J., & Redfield, M. M. 2019. Mitochondrial Morphology, Dynamics, and Function in Human Pressure Overload or Ischemic Heart Disease with Preserved or Reduced Ejection Fraction. *Circulation: Heart Failure*, *12*(2).

Chan, D. C. 2020. Mitochondrial Dynamics and Its Involvement in Disease. *Annu Rev Pathol.* 15:235-259.

Chappie, J. S., S. Acharya, M. Leonard, S. L. Schmid, and F. Dyda. 2010. G domain dimerization controls dynamin's assembly-stimulated GTPase activity. *Nature.* 465:435-440.

Chen, H., S. A. Detmer, A. J. Ewald, E. E. Griffin, S. E. Fraser, and D. C. Chan. 2003. Mitofusins Mfn1 and Mfn2 coordinately regulate mitochondrial fusion and are essential for embryonic development. *J Cell Biol.* 160:189-200.

Chen, Y., Y. Liu, and G. W. Dorn. 2011. Mitochondrial fusion is essential for organelle function and cardiac homeostasis. *Circ Res.* 109:1327-1331.

Choi, S. Y., P. Huang, G. M. Jenkins, D. C. Chan, J. Schiller, and M. A. Frohman. 2006. A common lipid links Mfn-mediated mitochondrial fusion and SNARE-regulated exocytosis. *Nat Cell Biol.* 8:1255-1262.

Chung, K. W., B. C. Suh, S. Y. Cho, S. K. Choi, S. H. Kang, J. H. Yoo, J. Y. Hwang, and B. O. Choi. 2010. Early-onset Charcot-Marie-Tooth patients with mitofusin 2 mutations and brain involvement. *J Neurol Neurosurg Psychiatry.* 81:1203-1206.

Dai, W., and L. Jiang. 2019. Dysregulated Mitochondrial Dynamics and Metabolism in Obesity, Diabetes, and Cancer. *Front Endocrinol (Lausanne).* 10:570.

Dang, X., Williams, S. B., Devanathan, S., Franco, A., Fu, L., Bernstein, P. R., Walters, D., & Dorn, G. W. 2021. Pharmacophore-Based Design of Phenyl-[hydroxycyclohexyl] Cycloalkyl-Carboxamide Mitofusin Activators with Improved Neuronal Activity. *Journal of Medicinal Chemistry*, *2021*(64), 12506–12524.

Daumke, O., and A. Roux. 2017. Mitochondrial Homeostasis: How Do Dimers of Mitofusins Mediate Mitochondrial Fusion. *Curr Biol.* 27:R353-R356.

Delettre, C., G. Lenaers, J. M. Griffoin, N. Gigarel, C. Lorenzo, P. Belenguer, L. Pelloquin, J. Grosgeorge, C. Turc-Carel, E. Perret, C. Astarie-Dequeker, L. Lasquellec, B. Arnaud, B. Ducommun, J. Kaplan, and C. P. Hamel. 2000. Nuclear gene OPA1, encoding a mitochondrial dynamin-related protein, is mutated in dominant optic atrophy. *Nat Genet.* 26:207-210.

Detmer, S. A., and D. C. Chan. 2007. Complementation between mouse Mfn1 and Mfn2 protects mitochondrial fusion defects caused by CMT2A disease mutations. *J Cell Biol.* 176:405-414.

Detmer, S. A., Velde, C. Vande, Cleveland, D. W., & Chan, D. C. 2008. Hindlimb gait defects due to motor axon loss and reduced distal muscles in a transgenic mouse model of Charcot - Marie - Tooth type 2A. *Human Molecular Genetics*, *17*(3), 367–375.

Eisner, V., M. Picard, and G. Hajnóczky. 2018. Mitochondrial dynamics in adaptive and maladaptive cellular stress responses. *Nat Cell Biol.* 20:755-765.

El Fissi, N., M. Rojo, A. Aouane, E. Karatas, G. Poliacikova, C. David, J. Royet, and T. Rival. 2018. Mitofusin gain and loss of function drive pathogenesis in Drosophila models of CMT2A neuropathy. *EMBO Rep.* 19:e45241.

Engelhart, E. A., and S. Hoppins. 2019. A catalytic domain variant of mitofusin requiring a wildtype paralog for function uncouples mitochondrial outer-membrane tethering and fusion. *J Biol Chem.* 294:8001-8014.

Eura, Y., Ishihara, N., Yokota, S., & Mihara, K. 2003. Two Mitofusin Proteins, Mammalian Homologues of FZO, with Distinct Functions Are Both Required for Mitochondrial Fusion. *Journal of Biochemistry*, *134*(3), 333–344.

Ferguson, S. M., & de Camilli, P. 2012. Dynamin, a membrane-remodelling GTPase. *Nature Reviews Molecular Cell Biology*, *13*(2), 75–88.

Ferreira, J. C. B., J. C. Campos, N. Qvit, X. Qi, L. H. M. Bozi, L. R. G. Bechara, V. M. Lima, B. B. Queliconi, M. H. Disatnik, P. M. M. Dourado, A. J. Kowaltowski, and D. Mochly-Rosen. 2019. A selective inhibitor of mitofusin 1-βIIPKC association improves heart failure outcome in rats. *Nat Commun.* 10:329.

Ford, M. G. J., and J. S. Chappie. 2019. The structural biology of the dynamin-related proteins: New insights into a diverse, multitalented family. *Traffic.* 20:717-740.

Franco, A., X. Dang, E. K. Walton, J. N. Ho, B. Zablocka, C. Ly, T. M. Miller, R. H. Baloh, M. E. Shy, A. S. Yoo, and G. W. Dorn. 2020. Burst mitofusin activation reverses neuromuscular dysfunction in murine CMT2A. *Elife.* 9:e61119.

Fransson, Å., Ruusala, A., & Aspenström, P. 2003. Atypical Rho GTPases have roles in mitochondrial homeostasis and apoptosis. *Journal of Biological Chemistry*, *278*(8), 6495–6502.

Fransson, Å., Ruusala, A., & Aspenström, P. 2006. The atypical Rho GTPases Miro-1 and Miro-2 have essential roles in mitochondrial trafficking. *Biochemical and Biophysical Research Communications*, *344*(2), 500–510.

Gao, S., and J. Hu. 2021. Mitochondrial Fusion: The Machineries In and Out. *Trends Cell Biol.* 31:62-74.

Giacomello, M., A. Pyakurel, C. Glytsou, and L. Scorrano. 2020. The cell biology of mitochondrial membrane dynamics. *Nat Rev Mol Cell Biol.* 21:204-224.

Glater, E. E., Megeath, L. J., Stowers, R. S., & Schwarz, T. L. 2006. Axonal transport of mitochondria requires milton to recruit kinesin heavy chain and is light chain independent. *Journal of Cell Biology*, *173*(4), 545–557.

Gomes, L. C., Benedetto, G. di, & Scorrano, L. 2011. During autophagy mitochondria elongate, are spared from degradation and sustain cell viability. *Nature Cell Biology*, *13*(5), 589–598.

Gordon, S. E., Munari, M., & Zagotta, W. N. 2018. Visualizing conformational dynamics of proteins in solution and at the cell membrane. *ELife*, *7*, e37248.

Hoppins, S., F. Edlich, M. M. Cleland, S. Banerjee, J. M. McCaffery, R. J. Youle, and J. Nunnari. 2011. The soluble form of Bax regulates mitochondrial fusion via MFN2 homotypic complexes. *Mol Cell.* 41:150-160.

Huang, P., T. Yu, and Y. Yoon. 2007. Mitochondrial clustering induced by overexpression of the mitochondrial fusion protein Mfn2 causes mitochondrial dysfunction and cell death. *Eur J Cell Biol.* 86:289-302.

Huang, X., X. Zhou, X. Hu, A. S. Joshi, X. Guo, Y. Zhu, Q. Chen, W. A. Prinz, and J. Hu. 2017. Sequences flanking the transmembrane segments facilitate mitochondrial localization and membrane fusion by mitofusin. *Proc Natl Acad Sci U S A.* 114:E9863-E9872.

Ishihara, N., Y. Eura, and K. Mihara. 2004. Mitofusin 1 and 2 play distinct roles in mitochondrial fusion reactions via GTPase activity. *J Cell Sci.* 117:6535-6546.

Jimah, J. R., Hinshaw, J. E. 2019. Structural Insights into the Mechanism of Dynamin Superfamily Proteins. Trends Cell Biol. 29(3):257–273

Karbowski, M., K. L. Norris, M. M. Cleland, S. Y. Jeong, and R. J. Youle. 2006. Role of Bax and Bak in mitochondrial morphogenesis. *Nature.* 443:658-662.

Koshiba, T., S. A. Detmer, J. T. Kaiser, H. Chen, J. M. McCaffery, and D. C. Chan. 2004. Structural basis of mitochondrial tethering by mitofusin complexes. *Science.* 305:858-862.

Kruppa, A. J., and F. Buss. 2021. Motor proteins at the mitochondria-cytoskeleton interface. *J Cell Sci.* 134:jcs226084.

Legros, F., Lombè, A., Frachon, P., & Rojo, M. 2002. Mitochondrial Fusion in Human Cells Is Efficient, Requires the Inner Membrane Potential, and Is Mediated by Mitofusins. *Molecular Biology of the Cell*, *13*, 4343–4354.

Li, H., Wang, H., Zhang, L., Wang, M., & Li, Y. 2021. Dl-3-n-Butylphthalide Alleviates Behavioral and Cognitive Symptoms Via Modulating Mitochondrial Dynamics in the A53T-α-Synuclein Mouse Model of Parkinson's Disease. *Frontiers in Neuroscience*, *15*.

Li, Y. J., Y. L. Cao, J. X. Feng, Y. Qi, S. Meng, J. F. Yang, Y. T. Zhong, S. Kang, X. Chen, L. Lan, L. Luo, B. Yu, S. Chen, D. C. Chan, J. Hu, and S. Gao. 2019. Structural insights of human mitofusin-2 into mitochondrial fusion and CMT2A onset. *Nat Commun.* 10:4914.

Lim, D., G. Dematteis, L. Tapella, A. A. Genazzani, T. Calì, M. Brini, and A. Verkhratsky. 2021. Ca^{2+} handling at the mitochondria-ER contact sites in neurodegeneration. *Cell Calcium.* 98:102453.

Liu, T. Y., X. Bian, F. B. Romano, T. Shemesh, T. A. Rapoport, and J. Hu. 2015. Cis and trans interactions between atlastin molecules during membrane fusion. *Proc Natl Acad Sci U S A.* 112:E1851-60.

Liu, X., Weaver, D., Shirihai, O., & Hajnóczky, G. 2009. Mitochondrial kiss-and-run: Interplay between mitochondrial motility and fusion-fission dynamics. *EMBO Journal*, *28*(20), 3074–3089.

Macdonald, R., Barnes, K., Hastings, C., & Mortiboys, H. 2018. Mitochondrial abnormalities in Parkinson's disease and Alzheimer's disease: Can mitochondria be targeted therapeutically? In *Biochemical Society Transactions* (Vol. 46, Issue 4, pp. 891–909).

Martínez-Reyes, I., and N. S. Chandel. 2020. Mitochondrial TCA cycle metabolites control physiology and disease. *Nat Commun.* 11:102.

Mejia, E. M., Nguyen, H., & Hatch, G. M. 2014. Mammalian cardiolipin biosynthesis. *Chemistry and Physics of Lipids*, *179*, 11–16.

Mills, E. L., B. Kelly, and L. A. J. O'Neill. 2017. Mitochondria are the powerhouses of immunity. *Nat Immunol.* 18:488-498.

Mishra, P., & Chan, D. C. 2014. Mitochondrial dynamics and inheritance during cell division, development and disease. In *Nature Reviews Molecular Cell Biology* (Vol. 15, Issue 10, pp. 634–646). Nature Publishing Group.

Misko, A., S. Jiang, I. Wegorzewska, J. Milbrandt, and R. H. Baloh. 2010. Mitofusin 2 is necessary for transport of axonal mitochondria and interacts with the Miro/Milton complex. *J Neurosci.* 30:4232-4240.

Misko, A. L., Y. Sasaki, E. Tuck, J. Milbrandt, and R. H. Baloh. 2012. Mitofusin2 mutations disrupt axonal mitochondrial positioning and promote axon degeneration. *J Neurosci.* 32:4145-4155.

Murata, D., K. Arai, M. Iijima, and H. Sesaki. 2020. Mitochondrial division, fusion and degradation. *J Biochem.* 167:233-241.

Orso, G., Pendin, D., Liu, S., Tosetto, J., Moss, T. J., Faust, J. E., Micaroni, M., Egorova, A., Martinuzzi, A., McNew, J. A., & Daga, A. 2009. Homotypic fusion of ER membranes requires the dynamin-like GTPase Atlastin. *Nature*, *460*(7258), 978–983.

Pernas, L., and L. Scorrano. 2016. Mito-Morphosis: Mitochondrial Fusion, Fission, and Cristae Remodeling as Key Mediators of Cellular Function. *Annu Rev Physiol.* 78:505-531.

Praefcke, G. J., and H. T. McMahon. 2004. The dynamin superfamily: universal membrane tubulation and fission molecules. *Nat Rev Mol Cell Biol.* 5:133-147.

Qi, Y., L. Yan, C. Yu, X. Guo, X. Zhou, X. Hu, X. Huang, Z. Rao, Z. Lou, and J. Hu. 2016. Structures of human mitofusin 1 provide insight into mitochondrial tethering. *J Cell Biol.* 215:621-629.

Ramachandran, R., and S. L. Schmid. 2018. The dynamin superfamily. *Curr Biol.* 28:R411-R416.

Rambold, A. S., B. Kostelecky, N. Elia, and J. Lippincott-Schwartz. 2011. Tubular network formation protects mitochondria from autophagosomal degradation during nutrient starvation. *Proc Natl Acad Sci U S A.* 108:10190-10195.

Rocha, A. G., A. Franco, A. M. Krezel, J. M. Rumsey, J. M. Alberti, W. C. Knight, N. Biris, E. Zacharioudakis, J. W. Janetka, R. H. Baloh, R. N. Kitsis, D. Mochly-Rosen, R. R. Townsend, E. Gavathiotis, and G. W. Dorn. 2018. MFN2 agonists reverse mitochondrial defects in preclinical models of Charcot-Marie-Tooth disease type 2A. *Science.* 360:336-341.

Rojo, M., Legros, F., Chateau, D., & Lombès, A. 2002. Membrane topology and mitochondrial targeting of mitofusins, ubiquitous mammalian homologs of the transmembrane GTPase Fzo. *Journal of Cell Science*, *115*(8), 1663–1674.

Rovira-Llopis, S., Bañuls, C., Diaz-Morales, N., Hernandez-Mijares, A., Rocha, M., & Victor, V. M. 2017. Mitochondrial dynamics in type 2 diabetes: Pathophysiological implications. *Redox Biology*, *11*, 637–645.

Samanas, N. B., E. A. Engelhart, and S. Hoppins. 2020. Defective nucleotide-dependent assembly and membrane fusion in Mfn2 CMT2A variants improved by Bax. *Life Sci Alliance.* 3:e201900527.

Santel, A., and M. T. Fuller. 2001. Control of mitochondrial morphology by a human mitofusin. *J Cell Sci.* 114:867-874.

Schwarz, T. L. 2013. Mitochondrial Trafficking in Neurons. *Cold Spring Harbor Perspectives in Biology*, *5*(6), a011304.

Scorrano, L., Ashiya, M., Buttle, K., Weiler, S., Oakes, S. A., Mannella, C. A., & Korsmeyer, S. J. 2002. A Distinct Pathway Remodels Mitochondrial Cristae and Mobilizes Cytochrome c during Apoptosis. *Developmental Cell*, *2*(January), 55–67.

Sloat, S. R., B. N. Whitley, E. A. Engelhart, and S. Hoppins. 2019. Identification of a mitofusin specificity region that confers unique activities to Mfn1 and Mfn2. *Mol Biol Cell.* 30:2309-2319.

Smirnova, E., D. L. Shurland, S. N. Ryazantsev, and A. M. van der Bliek. 1998. A human dynamin-related protein controls the distribution of mitochondria. *J Cell Biol.* 143:351-358.

Song, Z., M. Ghochani, J. M. McCaffery, T. G. Frey, and D. C. Chan. 2009. Mitofusins and OPA1 mediate sequential steps in mitochondrial membrane fusion. *Mol Biol Cell.* 20:3525-3532.

Stavropoulos, F., Sargiannidou, I., Potamiti, L., Kagiava, A., Panayiotidis, M. I., Bae, J. H., Yeom, S. C., Lee, J. Y., & Kleopa, K. A. 2021. Aberrant Mitochondrial Dynamics and Exacerbated Response to Neuroinflammation in a Novel Mouse Model of CMT2A. *International Journal of Molecular Sciences*, *22*(21), 11569.

Steffen, J., A. A. Vashisht, J. Wan, J. C. Jen, S. M. Claypool, J. A. Wohlschlegel, and C. M. Koehler. 2017. Rapid degradation of mutant SLC25A46 by the ubiquitin-proteasome system results in MFN1/2-mediated hyperfusion of mitochondria. *Mol Biol Cell.* 28:600-612.

Stuppia, G., F. Rizzo, G. Riboldi, R. Del Bo, M. Nizzardo, C. Simone, G. P. Comi, N. Bresolin, and S. Corti. 2015. MFN2-related neuropathies: Clinical features, molecular pathogenesis and therapeutic perspectives. *J Neurol Sci.* 356:7-18.

Tondera, D., Grandemange, S., Jourdain, A., Karbowski, M., Mattenberger, Y., Herzig, S., da Cruz, S., Clerc, P., Raschke, I., Merkwirth, C., Ehses, S., Krause, F., Chan, D. C., Alexander, C., Bauer, C., Youle, R., Langer, T., & Martinou, J. C. 2009. SIP-2 is required for stress-induced mitochondrial hyperfusion. *EMBO Journal*, *28*(11), 1589–1600.

Tornabene, B. A., N. V. Varlakhanova, C. J. Hosford, J. S. Chappie, and M. G. J. Ford. 2020. Structural and functional characterization of the dominant negative P-loop lysine mutation in the dynamin superfamily protein Vps1. *Protein Sci.* 29:1416-1428.

van der Bliek, A. M., T. E. Redelmeier, H. Damke, E. J. Tisdale, E. M. Meyerowitz, and S. L. Schmid. 1993. Mutations in human dynamin block an intermediate stage in coated vesicle formation. *J Cell Biol.* 122:553-563.

van Spronsen, M., Mikhaylova, M., Lipka, J., Schlager, M. A., van den Heuvel, D. J., Kuijpers, M., Wulf, P. S., Keijzer, N., Demmers, J., Kapitein, L. C., Jaarsma, D., Gerritsen, H. C., Akhmanova, A., & Hoogenraad, C. C. 2013. TRAK/Milton Motor-Adaptor Proteins Steer Mitochondrial Trafficking to Axons and Dendrites. *Neuron*, *77*(3), 485–502.

Wada, J., & Nakatsuka, A. 2016. Mitochondrial Dynamics and Mitochondrial Dysfunction in Diabetes. *Acta Medica Okayama*, *70*(3), 151–158.

Wang, W., J. Yin, X. Ma, F. Zhao, S. L. Siedlak, Z. Wang, S. Torres, H. Fujioka, Y. Xu, G. Perry, and X. Zhu. 2017. Inhibition of mitochondrial fragmentation protects against Alzheimer's disease in rodent model. *Hum Mol Genet.* 26:4118-4131.

Wong, Y. C., W. Peng, and D. Krainc. 2019. Lysosomal Regulation of Inter-mitochondrial Contact Fate and Motility in Charcot-Marie-Tooth Type 2. *Dev Cell.* 50:339-354.e4.

Wu S, Zhou F, Zhang Z, Xing D. 2011. Mitochondrial oxidative stress causes mitochondrial fragmentation via differential modulation of mitochondrial fission-fusion proteins. FEBS J. 278(6):941–954.

Yan, L., Y. Qi, X. Huang, C. Yu, L. Lan, X. Guo, Z. Rao, J. Hu, and Z. Lou. 2018. Structural basis for GTP hydrolysis and conformational change of MFN1 in mediating membrane fusion. *Nat Struct Mol Biol.* 25:233-243.

Yan, Duanmu, Zeng, Liu, & Song. 2019. Mitochondrial DNA: Distribution, Mutations, and Elimination. *Cells*, *8*(4), 379.

Zenisek, D., & Matthews, G. 2000. The role of mitochondria in presynaptic calcium handling at a ribbon synapse. *Neuron*, *25*(1), 229–237.

Zhang, Y., X. Liu, J. Bai, X. Tian, X. Zhao, W. Liu, X. Duan, W. Shang, H. Y. Fan, and C. Tong. 2016. Mitoguardin Regulates Mitochondrial Fusion through MitoPLD and Is Required for Neuronal Homeostasis. *Mol Cell.* 61:111-124.

Zhou, Y., S. Carmona, A. K. M. G. Muhammad, S. Bell, J. Landeros, M. Vazquez, R. Ho, A. Franco, B. Lu, G. W. Dorn, S. Wang, C. M. Lutz, and R. H. Baloh. 2019. Restoring mitofusin balance prevents axonal degeneration in a Charcot-Marie-Tooth type 2A model. *J Clin Invest.* 129:1756-1771.

Zhu, X., G. Perry, M. A. Smith, and X. Wang. 2013. Abnormal mitochondrial dynamics in the pathogenesis of Alzheimer's disease. *J Alzheimers Dis.* 33 Suppl 1:S253-62.

Zong, W. X., Rabinowitz, J. D., & White, E. 2016. Mitochondria and Cancer. *Molecular Cell*, *61*(5), 667–676.

Züchner, S., I. V. Mersiyanova, M. Muglia, N. Bissar-Tadmouri, J. Rochelle, E. L. Dadali, M. Zappia, E. Nelis, A. Patitucci, J. Senderek, Y. Parman, O. Evgrafov, P. D. Jonghe, Y. Takahashi, S. Tsuji, M. A. Pericak-Vance, A. Quattrone, E. Battaloglu, A. V. Polyakov, V. Timmerman, J. M. Schröder, J. M. Vance, and E. Battologlu. 2004. Mutations in the mitochondrial GTPase mitofusin 2 cause Charcot-Marie-Tooth neuropathy type 2A. *Nat Genet.* 36:449-451.